Charles University in Prague
Faculty of Mathematics and Physics

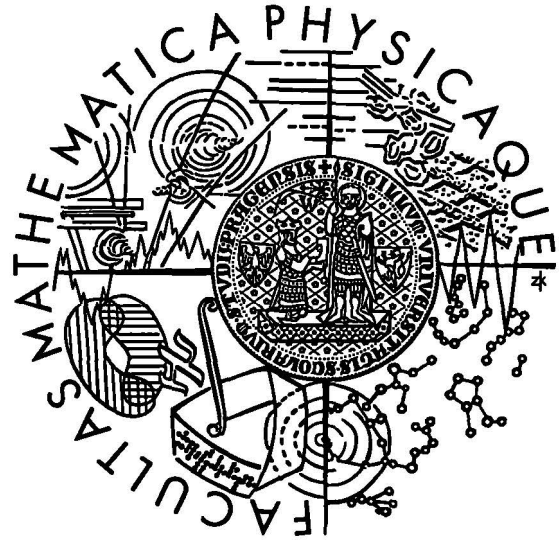

Doctoral Thesis

In situ neutron diffraction studies of deformation and transformation processes in modern types of steels

Ondrej Muránsky

Supervisor: RNDr. Petr Lukáš CSc.
Consultants: Prof. Ing. Jozef Zrník CSc., RNDr. Petr Šittner CSc.

Branch: F3 – Physics of condensed matter and material research

Prague, 2006

CONTENTS

PREFACE

The thermo-mechanically controlled processing (TMCP) has become an essential part in the development of new steels exhibiting a requested balance of user properties. The main advantage of TMCP consists especially in the possibility to produce low-alloyed structural steels with excellent mechanical properties without using expensive alloying elements [1]. In order to clarify the processes taking place during TMCP, the *in situ* (on-line) characterization of microstructure evolution upon TMCP has been strongly wished but such studies were impossible for long time because of the technical difficulties [2]. Just recent development of the *in situ* neutron diffraction technique enables us to obtain bulky information on deformation and transformation behaviour of metallic materials [3,4]. This experimental technique has found many useful applications in solid state physics, chemistry and biology. In particular, the neutron diffraction examination of internal strains/stresses in materials has become a very well established experimental tool in material science and engineering [5]. The analysis of the neutron diffraction profiles collected during thermal or/and mechanical treatment of any crystalline material can thus yield accurate bulk information on the structural changes associated with occurring deformation and transformation processes [6].

In order to emphasize the relevance of the *in situ* neutron diffraction method in the investigation of processes occurring within thermally or/and mechanically treated single and multiphase steels, different kinds of experiments were performed and included in the present doctoral thesis, namely:

- *In situ* investigation of the thermo-mechanically controlled processes (TMCP) of low-alloyed (Nb-added, Nb-free and Si-Mn) steels (Chapter 6).
- *In situ* neutron diffraction investigation of the deformation and transformation behaviour of low-alloyed (Si-Mn) TRIP-aided multiphase steels (Chapter 7).
- *In situ* neutron diffraction investigation of the deformation behaviour of single ferritic and multiphase duplex stainless steels (Chapter 8).

Neutron diffraction investigations were performed on the dedicated stress/strain diffractometers at the Nuclear Physics Institute in Řež near Prague, Czech Republic and at ISIS spallation neutron source situated at the CCLRC Rutherford Appleton Laboratory, United Kingdom.

ACKNOWLEDGEMENTS

I would like to express my large gratitude to my supervisor, Dr Petr Lukáš for his continuous encouragement and guidance throughout my post-gradual study as well as for his contributions to the investigation involved in the present thesis. He is acknowledged, in particular, for introducing the neutron diffraction technique to me and for supporting this work with ideas, comments, etc., furthermore, I would like to thank him for his help, patience and encouragement during three years of joint work at the Nuclear Physics Institute in Řež near Prague.

I'm also frankly thankful to both my consultants Professor Jozef Zrník and Dr Petr Šittner for useful advices, ideas and comments to this thesis and for their support during my post-gradual study.

I express my sincere thank to Professor Yo Tomota and Dr Pingguang G. Xu from Ibaraki University, Japan as well as to Dr Edward C. Oliver form the CCLRC Rutherford Appleton Laboratory, United Kingdom for the fruitful scientific collaboration, advices and help in solving scientific problems included in the present thesis.

I would like to individually thank to my colleague from the Nuclear Physics Institute Dr Miroslav Vrána for countless advices and many scientific contributions involved in this work as well as for his encouragement.

I also would like to thank the whole team of scientific workers of the Neutron Physics Department, namely: Dr Pavol Mikula, DrSc., Dr Pavel Strunz, Dr Vasyl Ryukhtin and Dr Ján Šaroun for their help, advices and encouragement during my three-year stay at the Nuclear Physics Institute. Many thank also to the technicians Mr Pavel Hyka, Mrs Božena Michalcová and our amazing secretary Mrs Eva Kodetová for their technical support and encouragement.

Last but not least I would like to thank to Professor Vladimír Sechovský, DrSc., and Doc. Pavel Svoboda from Charles University in Prague for their help and encouragement during my post-gradual study at Charles University.

SYMBOLS AND ABBREVIATIONS

Symbol	*Meaning*
σ_{GS}	contribution to yield stress by grain size
σ_y	yield strength
σ_{PN}	Peierls-Nabarro stress
σ_{SS}	contribution to yield stress by solid solution
σ_P	contribution to yield stress by precipitation
σ_D	contribution to yield stress by plastic deformation
ρ	dislocation density
G	shear modulus
A_{c1}	temperature at which austenite starts to form
A_{c3}	temperature at which austenite formation is complete
U	deformation matrix
M_s	martensite start temperature
ΔG_{M_s} / ΔG_{T1}	chemical free energy
ε_{pl}	plastic strain
τ_r	critical resolved shear stress
hkl	Miller indices
(hkl)	notation to identify a specific lattice plane
$\{hkl\}$	notation to identify a family of equivalent planes
$[hkl]$	notation to identify a specific direction
$< hkl >$	notation to identify a family of equivalent directions
$l_0^{I,II,III}$	length scales
ε_{hkl}	lattice strain
d_{hkl}	lattice spacing
θ_{hkl}^{B}	Bragg angle

Symbol	*Meaning*
t_{hkl}	neutrons time-of-flight
λ	wavelength
Q	scattering vector
σ_{ij}	stress tensor
ε_{ij}	strain tensor
C_{ij}	stiffness tensor
S_{ij}	compliance tensor
E, E_{hkl}	macroscopic and diffraction Young's modulus
ν, ν_{hkl}	macroscopic and diffraction Poisson's ratio
A_{hkl}	orientation factor
σ_{appl}	applied stress
$I_{\alpha}^{100}(T)$	extrapolated integrated intensity
$I_{\alpha}^{obs}(T)$	observed integrated intensity
f_{α}^{dif}	ferrite volume fraction determined by neutron diffraction
f_{α}^{SEM}	ferrite volume fraction determined by SEM
f^{γ}, f^{α}	austenite and ferrite volume fractions
T_t	transformation temperature
$R_{p0.2}$	conventional yield stress
A	elongation
R_m	tensile strength
ε^{ph}	volume-averaged phase strain
σ^{ph}	volume-average phase stress
a^{ph}	lattice parameter
$\sigma^{\gamma}, \sigma^{\alpha}$	austenite and ferrite phase stresses
$\varepsilon^{\gamma}, \varepsilon^{\alpha}$	austenite and ferrite phase strains
$\langle \varepsilon^2 \rangle^{1/2}$	the root mean square strain

Symbol	*Meaning*
F	factor describing interaction between dislocations
ε_{hkl}^{def}	lattice strain caused by tensile deformation
ε_{hkl}^{ther}	thermal residual lattice strain
ε_{hkl}^{tot}	total measured lattice strain

Abbreviation	*Meaning*
TMCP	thermo-mechanical controlled processing
IF	interstitial-free
ULC	ultra-low carbon
BH	bake-hardening
DP	dual-phase
TRIP	transformation-induced plasticity
HSLA	high strength low alloyed
CCT	continuous cooling transformation
IPS	invariant-plane strain
LM	light microscopy
SEM	scanning electron microscopy
PSD	position sensitive detector
TM	thermo-mechanical
XRD	X-ray diffraction
ND	neutron diffraction
TOF	time-of-flight
CAD	computer aided design
GSAS	general structure analysis system
b.c.c.	body-centered cubic
f.c.c.	face-centered cubic
f.c.t.	body-centered tetragonal
RMSS	root mean square strain
FWHM	full width at half maximum of diffraction profile

1.

INTRODUCTION TO STEELS

Steels are one of the most commonly used materials today, especially in industrial sectors such as an automotive industry. Their properties vary from very hard razor blades to the soft beverage cans. This wide range of mechanical properties stem from [7]:

- the two allotropic forms of iron ferrite (*b.c.c.*) and austenite (*f.c.c.*)
- the different alloying elements (interstitial, substitutional),
- the interactions between the TMCP (thermo-mechanically controlled process) parameters and different phase transformations.

From the ecological point of view, the main challenge of the automotive industry is to reduce the fuel consumption of vehicles. In order to achieve this requirement, a reduction of weight of cars seems to be the best way to proceed. On the other hand, for safety reason, if the weight of the vehicles is decreased, the strength of used materials should be increased, but the increase in strength must not be accompanied by a large drop in formability in order to enable the sophisticated forming.

1.1 DEMAND FOR STRENGTH

Metallurgical and materials engineers are often called on to design alloys having high strengths and ductility, simultaneously, but usually ductility is sacrificed when an alloy is strengthened. Several hardening techniques are at the disposal of material engineers, and an alloy selection frequently depends on the capacity of the material to be tailored with the mechanical characteristics required for a particular application [1]. In order to strengthen single-phase steels the following mechanisms are usually employed:

Strengthening by grain size reduction (σ_{GS}) is a powerful way for increasing the yield strength, tensile strength and uniform elongation simultaneously. A fine-grained material is harder and stronger than one which is coarse grained, since the former has a larger total grain boundary area to impede dislocation motion. For many materials, the yield strength σ_y varies with the grain size according to the Hall-Petch equation:

$$\sigma_y = \sigma_{PN} + k_y d^{-1/2}, \tag{1.1}$$

where d is the average grain diameter and σ_{PN} (Peierls-Nabarro stress), k_y are constants for a particular material [1,8,9].

Solid solution strengthening (σ_{SS}) by small atoms in interstitial position in iron lattice, e.g. elements as carbon or nitrogen, can bring about a significant increase in the yield strength (solution strengthening by interstitial atoms). Interstitial atoms interact with the stress field of dislocations and hinder their movement. Large atoms in substitutional positions impede the glide of the dislocations because of the distortion of the lattice (solution strengthening by substitutional atoms). In general the contribution of the solid solution strengthening to the yield strength (σ_y) can be calculated from the chemical composition

$$\sigma_{SS} = \sum k_i c_i, \tag{1.2}$$

where c_i are concentrations of individual alloying elements and k_i corresponding constants for the given solid solution [10].

Precipitation strengthening (σ_P) can cause additional reinforcement of steels already strengthened by grain refinement and by solid solution additions. The most common precipitates present in steels are carbides because of the low solubility of carbon in ferrite. In plain carbon steels, this carbide is usually cementite (Fe_3C) whereas in alloyed steels, the iron carbide is replaced by other carbides that are thermodynamically more stable (Cr_3C, TiC, NbC, etc.). The strengthening stems from the interaction of the dislocations with the precipitates [1,11].

When the volume fraction of the precipitated phase becomes large, the steel behaves like a metallic composite. The strengthening is no more only due to the interaction of the dislocations with the precipitates, but also due to the fact that the overall strength of the composite results from the uneven distribution of stresses between the present phases (***"stress partitioning"***). This brings about the *composite effect*, i.e. the synergetic interaction of phases having different mechanical properties (e.g. ferrite, bainite, retained austenite and strain-induced martensite in TRIP-aided multiphase steels).

Deformation strengthening (σ_D) is the phenomenon whereby a majority of metals become harder and stronger as they flow plastically. The dislocation density in a metal increases with deformation due to the dislocation multiplication or formation of new dislocations. As the dislocation density increases, the resistance to dislocation motion by other dislocations becomes more pronounced [1]. Thus, the imposed stress necessary to deform a metal increases with increasing plastic deformation. The contribution of the dislocation strengthening to the macroscopic yielding point can be generally related to the dislocation density ρ as

$$\sigma_D = 2\alpha G b \rho^{1/2}, \tag{1.3}$$

where b is Burger's vector, α ranges from 0.5 to 2.0 and G is the shear modulus[11].

The influence of all strengthening mechanisms to the yield strength (σ_y) can be express as their superposition (extended Hall-Petch equation) according to:

$$\sigma_y = \sigma_{PN} + \sigma_{GS} + \sigma_{SS} + \sigma_P + \sigma_D, \quad (1.4)$$

where σ_{PN} is Peierls-Nabarro stress and σ_{GS}, σ_{SS}, σ_P, σ_D are particular strengthening mechanisms, respectively [10,11].

1.2 STRENGTH VERSUS DUCTILITY

The most common problem of material engineering is that an increase in strength leads to a loss of ductility and, vice versa, an increase in ductility can usually be achieved through the sacrifice in strength. Nowadays, the automotive industry requires steels with high strength and ductility (formability), simultaneously. Higher strength allows making thinner components which results in reducing weight and thus decreasing the fuel consumption. It also improves the dent resistance of the material, which is important from the esthetic point of view, and improves passenger safety through higher crash resistance. High formability is necessary for manufacturing the individual components. For example, a door panel must be press-formed from thin gauge sheet in one [12] that requires adequate formability of the used alloy.

Therefore, many materials have been tested in an attempt to strike a balance between strength and formability. Steels exhibiting the best balance of the mechanical properties (strength, ductility) are *microalloyed steels*, *interstitial-free steels* (IF), *ultra-low carbon steels* (ULC), *bake-hardening steels* (BH), *dual-phase steels* (DP), *transformation-induced plasticity steels* (TRIP). A brief review of these materials commonly used in automotive industry is given in the following sections.

1.3 AUTOMOTIVE STEELS

1.3.1 Microalloyed Steels

Microalloyed steels are low-carbon steels alloyed with small amounts (~0.1 wt.%) of carbide-forming elements, especially niobium, titanium and vanadium [13,14]. The concept of microalloying combined with controlled thermo-mechanical processing (TMCP) yields steels with fine grains and subgrains. Fine-grained microstructure is provided by fine precipitates of the microalloy additions with carbon or nitrogen, typically on grain/subgrain boundaries [13,15]. Such precipitates also increase strength of steel by precipitation hardening, and besides that the ferrite is strengthened by solid solution hardening [16].

Microalloyed, high-strength low-alloy (HSLA) steels have become an indispensable class of the structural steels. Their ability to achieve final engineering properties in as hot-rolled conditions eliminates the need for additional heat treatments (e.g. normalizing) [17-20]. Yield strengths ranging from 550 to 600 MPa can be reached through small additions of selected carbide-nitride formers without requiring costly alloying elements [21]. The resulting cost-effectiveness of microalloyed steels has led to the successful replacement of heat-treated steels, particularly in automotive applications.

1.3.2 Interstitial-Free and Ultra-Low Carbon Steels

Interstitial-free (IF) and ultra-low carbon (ULC) steels are world widely known as the best affordable high quality materials for deep drawing applications. They have been used for wide applications ranging from automotive body to electronic components [22]. IF/ULC steels are similar to microalloyed steels, when combining very low carbon content (<80 ppm) with microalloying elements (Ti, Nb, V) [23]. However, IF steels theoretically does not have any interstitial atoms such as carbon, hydrogen, oxygen, nitrogen, or boron in the crystal lattices. This combination results in an extraordinary formability as well as a non-aging property [23].

1.3.3 Bake-Hardening Steels

Bake-hardening (BH) steels are often ultra-low carbon grades that are resistant to aging at room temperature, but not at slightly elevated temperature, especially after deformation [24]. BH steels are generally any high-strength, low-carbon steels that increases in strength as a result of a combination of straining and aging at higher temperature during the automotive paint cure cycle [25]. Thus, the interstitials diffuse to dislocations when the paint is baked onto the formed parts at ~180°C, such additional hardening of already formed components providing sophisticated method to manufacture sufficiently light and hard components.

1.3.4 Dual-Phase Steels

Dual-phase (DP) steels were developed to provide high strength formable alloys for the automobile industry. They are typically produced by intercritical annealing (producing an austenite-ferrite microstructure) followed by cooling/quenching resulting in a soft ferrite matrix containing hard martensite particles and often small amounts of retained austenite [24, 26]. The strains associated with the formation of martensite introduce free dislocations in the adjacent ferrite, thereby eliminating the sharp yield points. The mixture of hard martensite and soft ferrite also gives a higher average strength without losing formability [27].

1.3.5 Duplex Steels

Duplex stainless steels contain a mixed microstructure of about equal proportions of austenite and ferrite [28]. Their yield strength at the room temperature in the solution-annealed condition is more than double of standard austenitic stainless steels. This allows decreasing the thickness in some application, and thus achieving the weight reduction. The mechanical properties of wrought duplex stainless steels are highly anisotropic caused by the elongated grains and the crystallographic texture that results from usually used hot or cold rolling [28].

1.3.6 TRIP-Aided Multiphase Steels

Low-alloyed TRIP (TRansformation Induced Plasticity)-aided steels belong to multiphase steels offering an attractive combination of the strength and ductility [29,30]. Their microstructure usually consists of a mixture of polygonal (equiaxed) ferrite, bainite (bainitic ferrite) and metastable retained austenite [31,32]. Most of publications on TRIP-aided steels highlight the role of the retained austenite which transforms to martensite during the plastic deformation contributing thus to the enhanced strength and formability [32,33]. Since the contribution of the transformation strain due to the formation of a newly formed martensite phase is much smaller than the achieved total sample elongation, the strain-induced transformation *per se* provides only a minor contribution to the uniform elongation [32,33]. It however leads to the redistribution of stresses and a composite effect [32,34] responsible for the high uniform elongation of TRIP-aided steels [33,35].

2.

TRIP-AIDED MULTIPHASE STEELS

As has been mention before, usually, as the strength of steel increases, the uniform elongation (ductility, formability) is reduced (Fig.2.1). This causes complications in forming applications, such as an auto component press-forming. Zackay et al. pointed out, that the rate of strain hardening produced by dislocations is inadequate to compensate the increase in stress in the region of the neck [38]. This results in a lower strain to necking and a higher strain hardening [12].

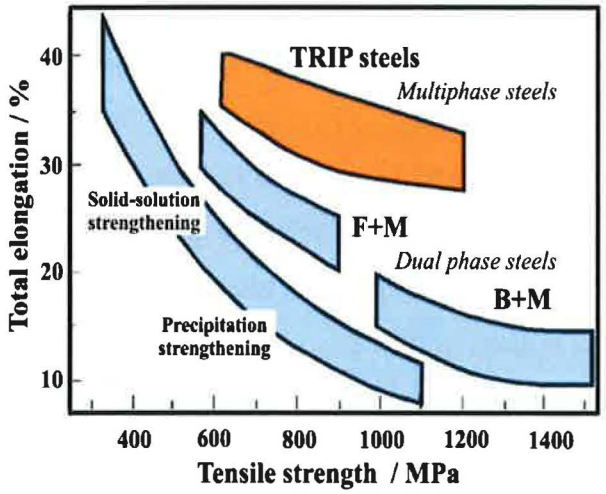

Figure 2.1: Comparison of the stress/strain behaviours of different types of steels [39].

Barriers (obstacles) present in steel microstructures which are used to delay the onset of necking must be harder than moving dislocation tangles and should be introduced during plastic straining [12]. If they were present in the starting material, they would simply result in an increase in the yield strength [12]. Martensite plates satisfy both conditions for delaying necking in plastically deformed steels because they are

- harder than moving dislocation,
- and are formed from retained (metastable) austenite during plastic deformation.

When the stress in a particular region of the sample reaches a sufficiently high value, such as near the onset of necking, retained austenite (in a multiphase steels like TRIP-aided steels) or metastable austenite (in a metastable-austenitic steels) will transform to martensite, which results in an increase of the local strain hardening rate and delaying necking. This process leads to a considerable improvement in ductility without losing strength.

2.1 MECHANICAL PROPERTIES

Mechanical properties (Fig.2.1) of TRIP-aided multiphase steels consist in their microstructure containing varying amount of *ferrite*, *bainite* (α-matrix), *retained austenite* and *strain-induced martensite* depending on the desired strength level. Volume fractions of phases contained in the alloy are significantly affected by the applied thermo-mechanically controlled processing (TMCP) (see section 2.3). Thus, it helps us to produce TRIP-aided steel with requested properties for particular applications.

Typical mechanical characteristics of TRIP-aided multiphase steels are [37]:

- *Work hardening* – As compared with other high strength steels, TRIP-aided steel displays higher work hardening rate in the entire range of plastic deformation.
- *Formability* – Due to high work hardening rate TRIP-aided steel behaves in a stable way in stamping processes (resistance to onset necking) and displays remarkably high formability (high potential to form parts of complex geometry).
- *Bendability* – TRIP-aided steel exhibits good bendability. As a result, product and process design solutions leading to spring back control are easier to implement.
- *Bake hardening* – TRIP-aided steels have an excellent bake-hardening capacity. The increase in the yield strength in typical paint baking cycle is approximately 70 MPa.

Fatigue performance – TRIP-aided steels have higher fatigue strength than equivalent conventional High Strength Low Alloy (HSLA) steels [37].

During deformation, a dispersion of hard second phase in soft ferrite can create a high work hardening rate, as has been observed in dual-phase steels [40]. However, in the TRIP-aided steels, the retained austenite also progressively transforms to martensite with the increasing strain, thereby increases the work hardening rate at higher strain levels. The TRIP-aided steels have a lower initial work hardening rate than the DP steels, but the hardening rate persists at higher strains [41].

2.2 EFFECT OF ALLOYING ELEMENTS

The most important alloying elements in TRIP-aided multiphase steels are carbon, manganese, silicon and niobium. There are also some others alloying elements as aluminium, phosphorus, molybdenum, etc. (see Fig.2.2), but because this thesis covers only Si-Mn TRIP steel, we will focus on the influence of only C, Mn, Si, Nb. All these alloying elements used in TRIP steels are mainly added for increasing a retained austenite volume faction in the final microstructure and for an improvement of mechanical properties of prepared steel in general.

2.2.1 Carbon

Carbon is an austenite stabilizer [42] and also it is generally accepted that carbon is the most powerful enhancer of the hardenability of austenite. Carbon expands the austenite region and encourages the formation of austenite over wider compositional limits (Fig.2.2). The expansion of the austenite region underlies the heat treatment of steels, by permitting the formation of a homogeneous solid solution. In addition, the expansion of the austenite region implies a decrease in the A_{C3} temperature, assuming that the driving force of transformation at any temperature is reduced. It is known [43] that the increase in the retention of austenite is strongly dependent on the dissolved carbon content.

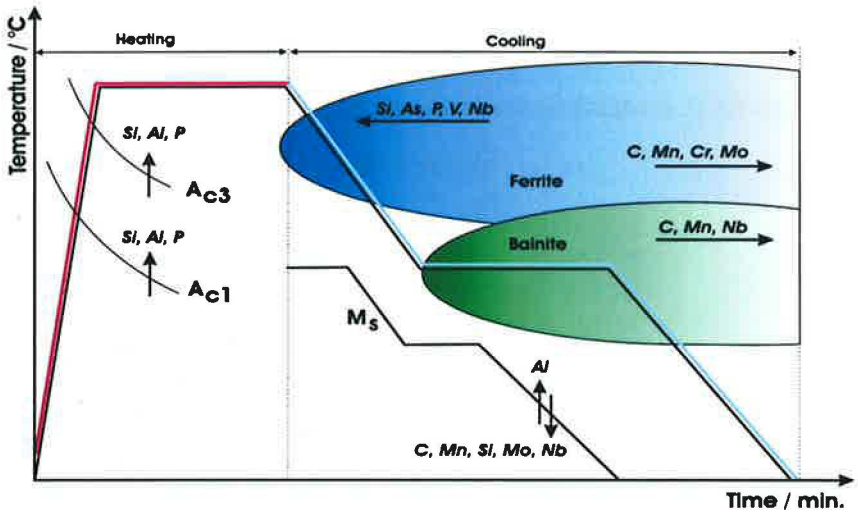

Figure 2.2: Effects of alloying elements on CCT [44].

2.2.2 Manganese

Manganese is also regarded as a beneficial additive for retaining austenite. It affects both the A_{C3} and A_{C1} transition temperatures [44-46] and reduces the width of the intercritical region, thereby stabilizing austenite over a wider temperature and carbon compositional range (Fig.2.2). Furthermore, Mn has lower activity coefficient of C, N, [47-49], and consequently, increases the solubility of Nb(C,N) in austenite and defends carbon lock-up as a carbide. These effects increase the carbon supersaturation of austenite whereby the austenite stabilization is affected during the thermo-mechanically controlled processes (TMCP) and straining in TRIP-aided steels.

2.2.3 Silicon

Silicon is a ferrite stabilizer because it restricts the formation of austenite by contracting the austenite region. Though this role is apparently against the main task of austenite

stabilization, but there are several different effects attributed to Si additions, which lead to an increase in the retained austenite volume fraction [50] (Fig.2.2). For instance, the addition of Si (>1 wt.%) increases the activity of carbon and thus exerts a retarding effect of carbides precipitation [32]. As a result, the austenite becomes enriched with carbon and becomes retained at low temperatures. The silicon concentration is also kept sufficiently high to ensure that cementite is not precipitated during the early stages of bainite formation [21].

2.2.4 Niobium

Niobium has been found to be the most beneficial microalloy in high strength, low-alloyed steels [51,52]. The presence of small amounts (<0.05 wt.%) of Nb in solution can act as an austenite stabilizer. When Nb remains in solution after hot deformation (rolling), it will usually precipitate in ferrite either during or after transformation. This increases the strength of steels through precipitation hardening (see section 1.3).

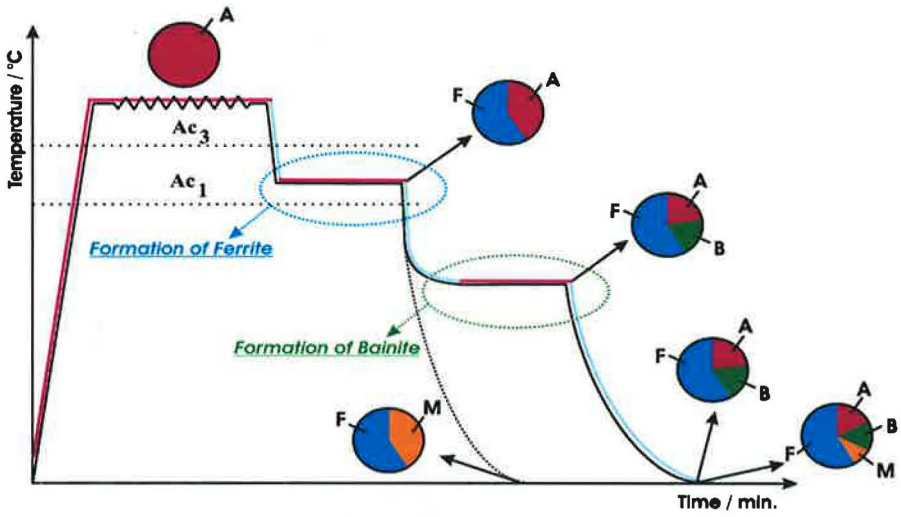

Figure 2.3: Typical scheme of thermo-mechanically controlled process (TMCP) employed in manufacturing TRIP steels.

2.3 THERMO-MECHANICALLY CONTROLLED PROCESSING

A complex multiphase microstructure of TRIP-aided steels is provided by special thermo-mechanically controlled processing (TMCP) (Fig.2.3). The typical TMCP of TRIP-aided steel involves the high temperature deformation in the austenite region and additional deformation in the intercritical (ferrite-austenite) region followed by controlled cooling through both the ferrite and bainite regions (Fig.2.3). By varying of particular steps in the used TMCP (applied deformations, transformation temperatures, cooling rates, etc.) it is possible significantly modify not just a volume fraction of retained austenite in the final microstructure but also a character of TRIP-aided steel microstructure in general. Microstructure evolution during

TMCP is described in next section because the importance of each particular step has to be considered.

2.3.1 Ferrite Formation

The first phase transformation which occurs during the cooling from the high-temperature austenite region is austenite-to-ferrite transformation (Fig.2.3). Ferrite nucleates in a heterogeneous way on the crystalline defects existing in the austenite. Depending on the ratio of the nucleation rate to the growth rate, the transformation results in different ferrite morphologies [53]:

- grain boundary allotriomorphs
- Widmanstatten side plates or laths
- intragranular idiomorphs
- intragranular plates [54].

Allotriomorphic ferrite is the predominant ferritic morphology found in Si-Mn TRIP-aided multiphase steels [55]. It nucleates at the highest temperatures, at austenite grain boundaries and grows into the grains to give rise to a well-defined (equiaxed) grain structure. This type of ferrite morphology is also known as polygonal ferrite [56].

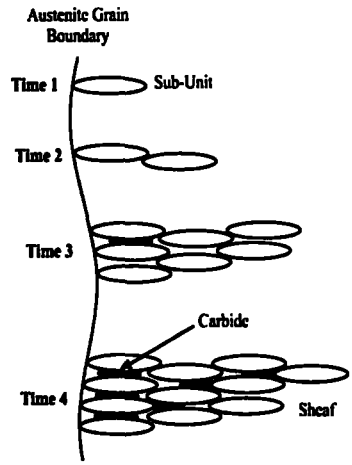

Figure 2.4: Schematic illustration of the development of a bainite sheaf [7,57].

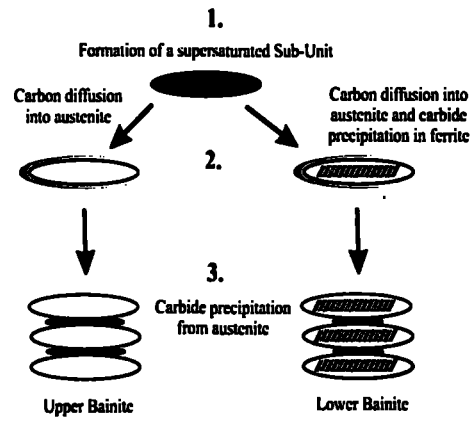

Figure 2.5: Schematic illustration of the formation of upper and lover bainite [57].

2.3.2 Bainite Formation

Bainite forms from austenite at temperatures above the martensite transformation temperature and below the pearlite reaction temperature (see CCT diagram Fig.6.18). There are two distinct morphologies of classical bainite, upper and lower bainite [58]. Bainitic ferrite supersaturated by carbon nucleates at austenite grain boundaries and grows as a plate until its growth is hindered by the dislocation pile-up at the austenite-ferrite interfaces

(Fig.2.4). After the growth of the bainite plate, the excess carbon can diffuse and get out of the bainite lath. The difference between the time required for forming cementite and the time required for carbon to exit the ferrite platelets allows distinguishing between upper and lower bainite. If carbon redistribution is rapid due to a high temperature, no cementite precipitates within the ferrite platelets. But cementite will be precipitated between the bainitic sub-units and upper bainite is formed. Vice versa, if the temperature is not high enough to allow the rejection of carbon from the ferrite platelets, cementite will precipitate within bainitic ferrite, gives rise to the lower bainite (Fig.2.5) [7].

2.3.3 Austenite Retention

As have been already mentioned the austenite-to-ferrite phase transformation is the first phase transformation occurring during cooling of a fully austenitized steel (Fig.2.3). Because of a relatively low solubility of carbon in ferrite, it is generally accepted that carbon saturates the neighbouring austenite grains. Furthermore, additional austenite enrichment by carbon is achieved due to the following partial phase transformation of austenite-to-bainite. Main difficulty of the austenite retention in conventional high strength steels is in their inability to sufficiently saturate the remaining austenite with carbon during applied TMCP. But the suitable combination of the TMCP application with appropriate alloying can significantly modify continuous cooling transformation diagram (CCT) (Fig.6.18) (existence of austenite, ferrite, bainite, martensite regions) and thus remedy the ability for the austenite retention.

2.4 MARTENSITIC TRANSFORMATION

The martensite formation can occur at very low temperatures where atomic mobility is inconceivably small, and diffusion of even interstitial atoms is not possible within the time scale of the transformation. Hence, changes in the crystal structure at low temperatures are achieved by homogenous deformation (*Bain Distortion*) of the parent phase and atoms displacement (*shuffles*) [27,59]. Main characteristics of martensitic transformations are as follows:

- martensitic transformations are the first order, diffusionless, shear (displacive) solid state structural changes
- atoms displacement can be described as a combination of a homogeneous lattice deformation, known also as *Bain Distortion,* and so-called *shuffles*
- during the homogeneous lattice deformation (*Bain Distortion*) the Bravais lattice is changed into another by the coordinated shift of all atoms

- a shuffle is a coordinated shift of atoms within a unit cell, which change the crystal lattice but does not produce homogenous lattice distortive strain [59].

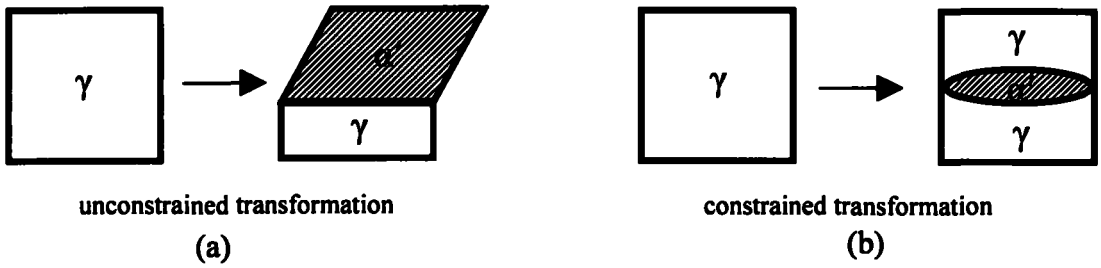

Figure 2.6: The habit plane of martensite (α') under condition of unconstrained and constrained transformation, respectively.

To minimize the strain energy the martensite is formed as thin plates on particular crystallographic planes known as the habit planes. The habit plane is the interface (invariant) plane between austenite and martensite. When the transformation occurs without any constraint, the habit plane is macroscopically flat as can be seen in Fig.2.6a. If the martensite is formed in a constrained environment, it grows in the shape of a thin lenticular plate or lath and the habit plane is a little less clear in the sense that the interface is curved on a macroscopic scale (see Fig.2.6b). Nevertheless, the macroscopic habit plane is identical in both cases (Fig.2.6a,b) [60].

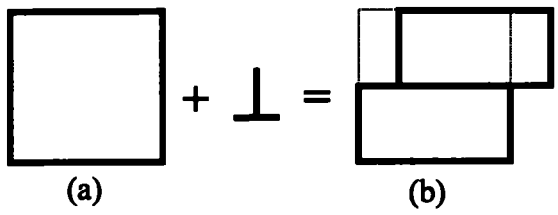

Figure 2.7a,b: Step caused by the passage of a slip dislocation.

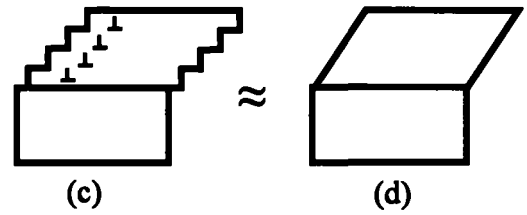

Figure 2.7c,d: Many slip dislocations, causing a macroscopic shear.

2.5 STRAIN-INDUCED MARTENSITIC TRANSFORMATION

2.5.1 The Shape Deformation due to Strain-Induced Martensitic Transformation

Passage of a slip dislocation through a crystal causes the formation of a step where the glide plane intersects the free surface (Fig.2.7a,b). The passage of many dislocations on parallel slip planes brings about macroscopic shear (Fig.2.7c,d). Slip causes a change in the shape but not a change in the crystal structure, because the Burger's vector of the dislocation is also lattice vector [60].

During martensitic transformation, the pattern in which the atoms of the parent crystal are arranged is deformed into the appropriate martensite form. This is connected with changes in

the macroscopic shape of the crystal undergoing transformation. The dislocations responsible for the deformation are concentrated in the martensite/austenite (α'/γ) interface with such Burger's vectors that in addition to deformation they also cause the change in crystal structure. The deformation proceeds in the way that an initially flat surface becomes uniformly tilted about the line formed by the intersection of the interface plane with the free surface.

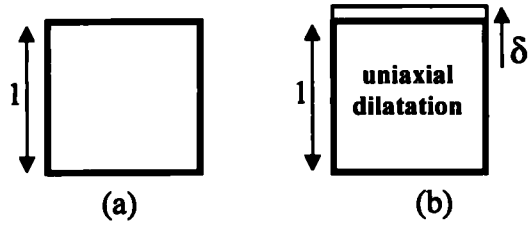

Figure 2.8a,b: (a) parent phase, **(b)** an invariant-plane strain (IPS) with a uniaxial dilatation.

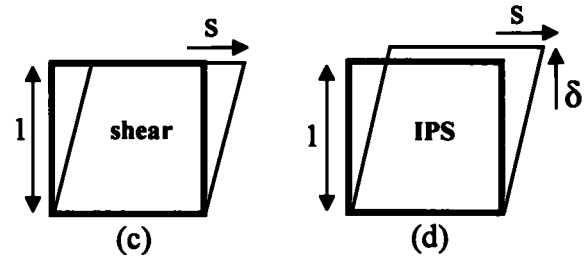

Figure 2.8c,d: (c) an IPS which is simple shear, **(d)** an IPS a uniaxial dilatation and a simple shear.

The invariant-plane strain (IPS) forming martensite is a combination of a large shear ($s \sim 0.25$) parallel to the invariant-plane and dilatational strain ($\delta \sim 0.03$) normal to the habit plane [32,59] (Fig.2.8d). This deformation can be defined by the following deformation matrix (U) form [32].

$$U = \begin{pmatrix} 1 & 0 & s \\ 0 & 1 & 0 \\ 0 & 0 & 1+\delta \end{pmatrix}. \qquad (2.1)$$

2.5.2 Thermodynamics of Strain-Induced Martensitic Transformation

The thermodynamics of the strain-induced martensitic transformation of the retained austenite can be easily understood from Fig.2.9. This figure schematically represents the variation of the free energy curves of the martensite and austenite as a function of temperature. Austenite is metastable at the temperature (T_1) since the change of a free energy accompanying its transformation to the martensite has not yet reached a critical driving force. Temperature (T_1) is the intermediate temperature between the equilibrium transformation temperature (T_0) (at which austenite and martensite have the same free energy) and the temperature (M_S) at which the undercooling is sufficient to induce transformation. At the temperature T_1, austenite can transform into martensite if an additional energy is provided

(***U'***). In the case of the strain-induced martensitic transformation, this energy is provided by the mechanical solicitation (deformation) [7].

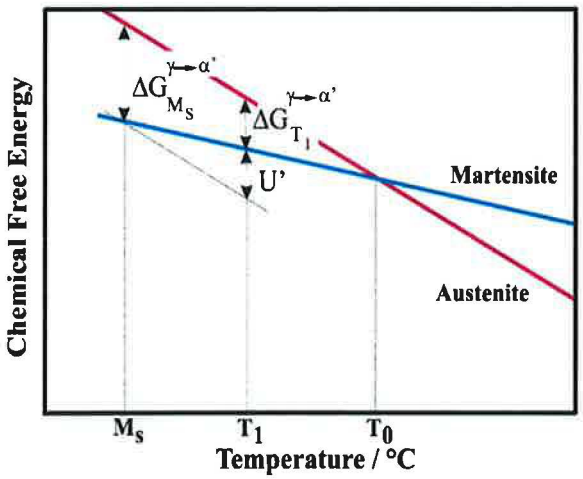

Figure 2.9: The chemical free energies of austenite and martensite as a function of temperature, $T_0 > T_1 > M_s$ [61].

2.5.3 Kinetics of Strain-Induced Martensitic Transformation

If the TRIP steel specimen is strained beyond the necessary critical strain/stress to initiate the martensite formation, then the amount of the strain-induced martensite increases with an increase of the plastic strain. The kinetics of the strain-induced martensite transformation can be expressed as a function of the plastic strain. It was proposed that the principal feature of the transformation-deformation function is given by the following proportionality [62]:

$$V_{\alpha'} \approx \varepsilon_{pl}, \tag{2.2}$$

where $V_{\alpha'}$ is the martensite volume and ε_{pl} is the plastic strain.

However, the formation of a martensite plate itself produces dilatational and coherency strains in the surrounding structure. These strains account for the autocatalytic nature of the martensite formation, that is, the ability of martensite to accelerate the formation of additional martensite [62]. This autocatalysis effect can be taken into account by modifying Eq.2.2 to:

$$V_{\alpha'} \approx \varepsilon_{pl}^{B}, \tag{2.3}$$

where ***B*** is the autocatalysis exponent.

As the strain-induced transformation of austenite to martensite proceeds, there is a decrease in the volume fraction of the retained austenite and, as a result, there is less austenite for further transformation. To account for this austenite exhaustion, Eq.2.3 is then modified to:

$$V_{\alpha'} \approx \varepsilon_{pl}^{B}(V_{\gamma}), \tag{2.4}$$

where V_γ is the volume fraction of residual austenite.

The Eq.2.4 can be transformed from the proportionality to the following equality as follows:

$$V_{\alpha'} = A\varepsilon_{pl}^{B}(V_\gamma), \tag{2.5}$$

where A is a proportionality constant.

If the sum of $V_{\alpha'}$ and V_γ is unity, Eq.2.5 can be rewritten into more useful forms in which $V_{\alpha'}$ and V_γ are expressed as functions of the plastic strain:

$$V_{\alpha'} = \left(1+\frac{\varepsilon_{pl}^{-B}}{A}\right)^{-1} \text{ and } V_\gamma = 1-\left(1+\frac{\varepsilon_{pl}^{-B}}{A}\right)^{-1}, \tag{2.6}$$

where coefficient A represents the difficulty with which an austenite structure can undergo the strain-induced transformation to martensite, i.e. mechanical stability (see section 2.6), and B represents the effect of martensite formation in stimulating the formation of further martensite, or an index of the autocatalytic nature of the transformation [55].

2.6 RETAINED AUSTENITE STABILITY

Mechanical stability of retained austenite in TRIP-aided multiphase steels is increased by a decrease in the particle size, the mechanism which involves both martensite nucleation and growth [63]. When a fixed volume of the remaining austenite is divided into discrete, disconnected regions it is possible to isolate regions that do not contain an effective martensite nucleation site i.e. dislocations. It is also possible that, even if an effective martensite nucleus exists the retained austenite particle can be stabilized by the increased matrix constraints resulting from the partially coherent nature of the ferrite-austenite (α/γ) interfaces [64].

The morphology of the retained austenite in Si-Mn TRIP-aided steels has been also investigated [65] while it has been shown that there are basically three different morphologies of retained austenite at room temperature:

1. *thin film-type retained austenite* located between bainite lath boundaries
2. *island-type retained austenite* located inside the comparatively large ferrite matrices
3. *granular-type retained austenite* located along the ferrite grain boundaries

The island-type retained austenite is considerably smaller in size when compared to the surrounding ferrite phase and acts similar to precipitates in steel and, as a result, it is difficult to transform due to the size effect [65,66]. Because the film-type retained austenite is protected from the imposed stress by the surrounding hard phase, its deformation and

transformation will hardly occur. On the other hand, since the granular-type retained austenite lies mainly around ferrite grain boundaries where high stress gradients are produced between grains of different orientations [66], the transformation to martensite occurs rather easily.

The last but one of the most important parameter which controls the mechanical stability of the retained austenite is the enrichment of solutes in the austenite, in particular, the amount of dissolved carbon. Additions of interstitial atoms such as carbon strengthen both the parent austenite and any martensite formed from it. The higher the solute enrichment the greater the stability of the retained austenite is (i.e. more resistant to undergo transformation to martensite) [55,66].

3.

DEFORMATION MECHANISMS OF STEELS

3.1 DEFORMATION STATE

The elastic/plastic deformation of metals is the most important issue of metals applications in the everyday life. In general, plastic deformation of metallic materials can proceed by means of:

- *dislocations* (slip mechanism of deformation)
- *twins* (twinning mechanism of deformation).

3.1.1 Glide of Dislocations and Work Hardening

The movement of a dislocation consists of the dislocation glide on a compact (close packed) or near compact crystallographic plane in the direction given by the Burger's vector. In the case of the face-centered cubic (*f.c.c.*) metals, these planes are {111} planes and the slip directions are <110> directions. In the case of the body-centered cubic (*b.c.c.*) metals the active slip direction is <111> and the main slip planes are {110}, {211} or {321}. Glide on a given plane is possible only if the resolved shear stress on this plane is larger than the so-called *critical resolved shear stress* (τ_r) [7]. Beside glide mechanism, dislocation motion can also take place by two additional mechanisms, *cross-slip* and *dislocation climb*. A screw dislocation, which has no defined slip planes can cross-slip onto another plane. And an edge dislocation can climb perpendicularly to its Burger's vector which necessitates the creation or the diffusion of a vacancy. The concentration and diffusion of vacancies is being thermally activated, therefore dislocation climb plays a major role in the high temperature deformation of metals.

During plastic deformation, new dislocations are generated mainly by the *Frank-Read* mechanism. A dislocation that is pinned at two points (by precipitates or jogs) progressively bulges under the action of the applied stress on the slip plane of dislocation. Different types of interactions participate in hindering and even stopping the motion of dislocations result in the formation of jogs, the interaction between the stress fields around two dislocations and the splitting (decomposition) into partial dislocations. This leads to an increase in the critical resolved shear stress (τ_r) on a given slip system and to the phenomenon known as the ***work hardening.***

3.1.2 Recovery and Recrystallisation of Deformed Microstructures

An energy absorbed by material during straining, so-called "*stored energy*" makes a deformed material thermodynamically unstable. But if deformed material is heated to the temperature high enough, thermally activated phenomena can operate in order to decrease the stored energy by rearrangement of the dislocation structure in deformed metal into lower energy configurations. In general, two very different types of *softening mechanisms* are observed:

Recovery – is defined as changes in the properties of a deformed material which occur prior to recrystallisation. Recovery is not a single microstructural process but involves a series of mechanisms as the annihilation of some dislocations by the combination of dislocations having different signs and the reorganisation of the dislocations in stable arrays [67].

Recrystallisation – Recrystallisation can be easily understood as nucleation and growth phenomenon involving thermally activated processes for which the driving force is provided by the stored energy [68,69]. Whereas only a small part of the dislocation density can be removed by recovery, recrystallisation enables the formation of a new, *dislocation-free* microstructure.

3.2 HOT DEFORMATION

As has bee already mentioned, hot deformation is an effective way of producing low cost high strength structural steels. The strategy behind this technique is usually to minimise the final grain size or to produce multiphase microstructures. The following deformation stages are commonly distinguished in the typical thermo-mechanical controlled processing (TMCP) of steels:

- deformation in the austenite recrystallisation region
- deformation in the non-recrystallisation region
- deformation in the two-phase (austenite-ferrite) region.

These three stages are usually combined with rapid cooling e.g. in the TMCP of TRIP-aided multiphase steel (see section 2.3).

3.2.1 Deformation in the Austenite Recrystallisation Region

During the first stage of TMCP (~1200°C), the austenite grain is refined considerably through deformation and recrystallisation. Additions of microalloyed elements as niobium, titanium and vanadium (see section 1.3) prevent significant grain growth in this high

temperature region. If such recrystallised austenite is cooled, fairly coarse ferrite grains nucleate at austenite grain boundaries and grow into the austenite grains. Under these conditions, the final ferrite grain size is dependent on the grain size of the undeformed austenite from which it transforms. After the first stage of deformation, the steel is usually cooled down to approximately 950°C and deformed again.

3.2.2 Deformation in the Non-Recrystallisation Region

During this stage, the temperature of the steel falls below the non-recrystallisation temperature (T_{nr}). The deformation of austenite in this region leads to the formation of elongated austenite grains. The change from a recrystallised to a deformed microstructure is accompanied by an increase in the grain boundary area per unit volume increasing the nucleation site density. Moreover, intergranular defects such as shear bands created during deformation can provide additional sites for ferrite nucleation [68].

3.2.3 Deformation in the Two-Phase Region

The aim of this deformation is to increase ferrite nucleation site by deforming austenite grains in two-phase region as well as strengthen the microstructure by deforming already existing ferrite grains. Consequently the final microstructure contains hard deformed ferrite grains and soft undeformed fine-grained ferrite nucleated in deformed austenite grains during cooling from deformation temperature [70,71].

4.

CLASSIFICATION OF INTERNAL STRESSES

4.1 MACROSTRESSES AND MICROSTRESSES

The internal stresses are commonly divided into three classes or types, by the length scales over which they vary and over which they are self-equilibrated, ***Type I***, ***Type II***, and ***Type III*** stresses. They are often categorized as ***macrostresses*** (*Type I*) and ***microstresses*** (*Type II* and *Type III*). Their presence in solids can be very detrimental to the performance of a material or the lifetime of a component. Alternatively, some beneficial stresses can be introduced deliberately in a production process [72-74].

Type I Macrostress

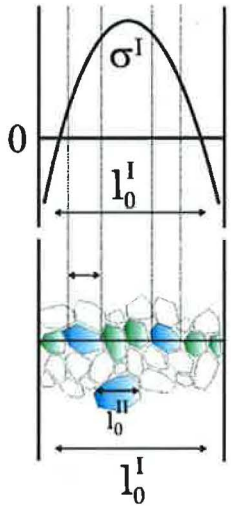

Figure 4.1: Type I stress varies on a length scale l^{I}_{0}, which is of the order of the sample dimensions.

Type II Microstress

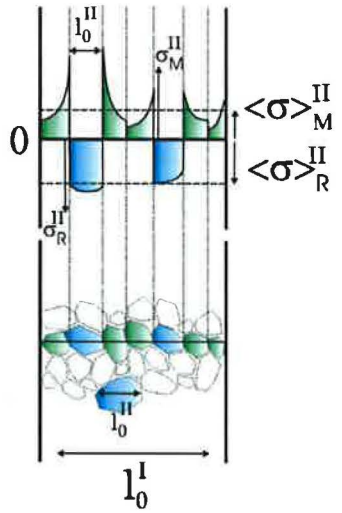

Figure 4.2: Type II stress varies on a length scale l^{II}_{0}, which is of the order of the grain size [72].

4.1.1 Type I - Macrostress

Type I stresses are self-equilibrate over a length l^{I}_{0} comparable to the macroscopic dimension (~ mm) of the measured sample. These stresses are typically a consequence of macroscopic misfits generated, for example, by macroscopic plastic deformation or quenching of a hot sample. They are assumed to be continuous from grain to grain, and indeed, even from phase to phase (Fig.4.1).

4.1.2 Type II - Microstress

Type II stresses arise from misfits having a characteristic length scale l^{II}_{0} comparable to the grain size of polycrystalline solids, usually a few tens of microns. *Type II* stresses are

discontinuous form grain to grain (Fig.4.2). Low-level *Type II* stresses almost always exist in polycrystalline materials, but because of the propensity for large property mismatches between the phases, more significant *Type II* stresses occur in multiphase materials. This grain-scale stresses are also usually called ***intergranular stresses***, however they have nothing to do with stresses directly associated with the grain boundary region [72,74].

The grain-to-grain and phase-to-phase misfits are shown in (Fig.4.2) schematically by separating the fitting grains. In this example, the major *Type II* misfit is caused by differential thermal contraction, which on average, generates tensile stresses ($\langle\sigma\rangle_M^{II}$) in the matrix (green grains) and compressive average phase stresses ($\langle\sigma\rangle_R^{II}$) in the reinforcement (blue). Elastic mismatches between grains, or phases, in combination with macrostresses will also generate *Type II* stress [72,73].

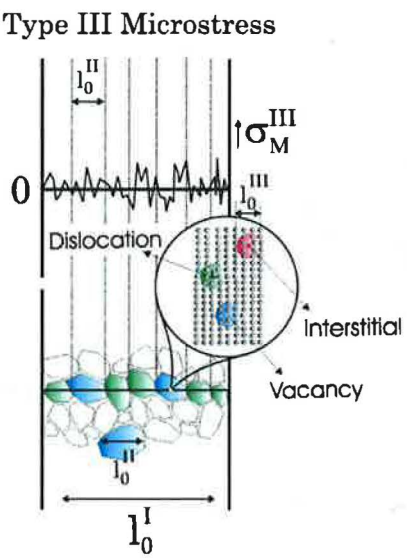

Figure 4.3: Type III stress varies on a subgrain length scale l^{III}_0, which is less than the grain size.

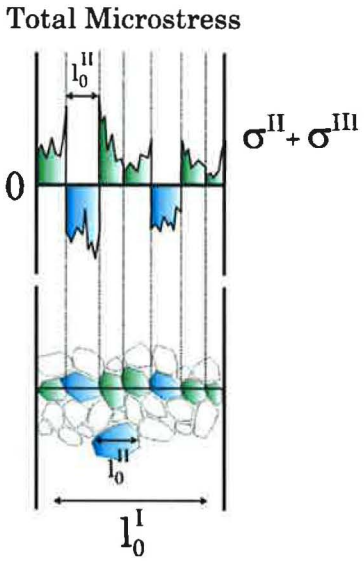

Figure 4.4: Type II and Type III stresses are often grouped together and termed microstress [72].

4.1.3 Type III - Microstress

Type III stresses self-equilibrate over a length scale l^{III}_0, smaller than the characteristic length scale of the microstructure, e.g. the grain size or the fiber/particle spacing for composite materials. These stresses are varying within a specific grain, such as due to grain subdivision into cell structures. In this case, their origins are misfits, such as crystal defects, with a scale shorter than the grain scale (Fig.4.3). The *Type III* category typically includes stresses due to coherency at interfaces and dislocation stress fields. *Type II* and *III* stresses are also sometimes collectively referred as *microstresses* and they can vary in the manner shown in (Fig.4.4).

5.

DIFFRACTION STRESS/STRAIN MEASUREMENT

5.1 DIFFRACTION TECHNIQUES

Neutron/X-ray (synchrotron) diffraction lattice strain measurement provides much more information than a conventional strain gauge. By sampling a well-defined subset of grains, each diffraction peak provides insight the *Type I*, *II* and *III* elastic strains within the sample. In the following section, these particular diffraction techniques are briefly described since each method has some advantages and disadvantages.

5.1.1 X-Ray Diffraction

X-ray diffraction techniques have been used extensively in scientific and engineering fields over the years [75,76]. However, the major shortcoming of this diffraction technique for stress measurement remains in the lack of the capability to penetrate deeply into typical crystalline materials used in the engineering industry. However, the penetration path length is adjustable by appropriate selection of specific X-ray producing targets, and hence the X-ray energies and wavelengths but in general, the technique is limited to penetrations of a few tens of microns. Therefore, non-destructive X-ray measurements have been limited to studies of near-surface effects or otherwise thin structures. In the case of successively removed surface layers, either by etching, polishing, or gentle machining, this technique can be adapted to probe stresses deeper below the surface of a material [72].

5.1.2 Synchrotron X-Ray Diffraction

Many of the limitations of the X-ray techniques (see section 5.1.1) have been overcome by the rapid introduction of the third-generation synchrotron sources [77]. These sources provide access to higher X-ray energies, or hard X-ray as they are commonly known. Relatively very high X-ray intensities lead to path lengths of centimetres in steel and even tens of centimetres in aluminium. As a probe of samples important to engineering and materials science, synchrotron sources now offer the opportunity to study phenomena within most samples [78,72]. However, the main advantages are the high intensity and the high collimation of the beam that allow diffraction data acquisition rates of order of seconds from the sample gauge volume of millimeter-size or even micron-size. For many engineering

problems requiring residual stress measurement, such an extremely high data acquisition rate is not necessary and also sub-millimeter-size spatial resolution is usually not essential. But employing a lower spatial resolution combined with a higher level of penetration reaching to several centimeters into materials like, steel, nickel, or titanium is often necessary [72,78,79].

5.1.3 Neutron Diffraction

Neutron diffraction is an experimental technique with immense potential for the characterization of strains and stresses via probing the interior of solids. It brings the opportunity to acquire information otherwise inaccessible on the state of strain within the bulk of a structure. The main advantages of this technique are:

- neutron penetration power of the order of centimetres in the most engineering materials
- a non-destructive character which can be used to monitor the evolution of internal stresses in realistic environments and loading conditions
- it provides a spatial resolution that is easily adjustable and can be adequate for resolving strain gradients in engineering components
- it can be used to study bulk macroscopic engineering stresses, average phase-specific stresses, and intergranular stresses (see section 4.1)

The high neutron penetration power which is of about three orders of magnitude higher than that of conventional X-rays for the most materials (e.g. in steel ~ 0.8 cm [72]), provides non-destructive access to the interior of solids. Therefore, for the majority of engineering applications, it can provide access to elastic strain profiles extending centimetres into structural components. Moreover, the penetration power in principle enables a free choice of the strain measurement direction. The technique has been proved to be a valuable engineering tool used in product design and development. Common applications include *ex situ* residual measurement of stresses due to welding, plastically deformed structures (such as cold expanded holes), automotive components (such as crank shafts) etc. and *in situ* measurement of stresses during thermal exposure or mechanical loading (see experimental part).

Application to different problems

Thanks to the nature of the diffraction process which focuses on specific lattice plane spacings of a subset of crystallites, or grains, having specific orientations relative to the scattering geometry, the technique provides unique insights for both fundamental and applied materials science studies. This grain-selective character facilitates the separation of the strain

response of different phases in a multiphase material, provided that the phases are distinguishable in a crystallographic sense [72]. Typical examples of a multiphase engineering material are already mentioned duplex steels, dual-phase steels, TRIP-aided multiphase steels etc., eventually any metallic composites. Neutron diffraction enables the investigation of the stress/strain response of the individual phases simultaneously, and thereby it can provide valuable information on processes taken place inside the solids during the straining (tensile test, low-cycle fatigue, etc.) [80,81].

Sensitivity to the crystallographic character of the phases also makes this technique to be an attractive probe for the investigation of composite systems where one phase may be actuated through imposed variations of some external parameter (e.g. magnetic field, applied load, heat treatment, etc.). As an example, a system where one phase possesses e.g. piezoelectric, magnetostrictive or shape-memory properties, can be mentioned. Regarding shape memory alloys, phase transformations have been studied by diffraction for a long time but neutron diffraction has been employed in studying their micromechanical aspects only recently. By providing access to the interior of solids, the technique is especially attractive for studies of the micromechanical effects associated with ongoing phase transformations, particularly in shape-memory alloys (e.g. NiTi, TiPt) and TRIP-aided steel etc. [82,83].

5.2 PRINCIPLE OF STRAIN MEASUREMENT BY DIFFRACTION TECHNIQUES

In general, macrostresses (*Type I*) and microstresses (*Type II, III*) which exist in the polycrystalline material, cause different observable effects on diffraction pattern. Different diffraction methods are hence intended to detect them [84-86]. Information on lattice strain ε_{hkl} caused by macrostresses is obtained by means of the Bragg's equation

$$\lambda = 2d_{hkl} \sin\theta^{B}_{hkl}. \tag{5.1}$$

The macrostresses bring about the average change of the lattice spacing Δd_{hkl} within the gauge volume due to the elastic deformation of the crystal. This change is further related to the shift $\Delta\theta^{B}_{hkl}$ of the diffraction peak through the Bragg's equation (Eq.5.1). Considering that the diffraction peak shifts are small, they can be derived by its differentiation as

$$\varepsilon_{hkl} = \frac{(d_{hkl} - d^{0}_{hkl})}{d^{0}_{hkl}} = \frac{\Delta d_{hkl}}{d_{hkl}} = -[\cot(\theta^{B0}_{hkl})](\theta^{B}_{hkl} - \theta^{B0}_{hkl}) \text{ or } \varepsilon_{hkl} = \frac{\Delta t_{hkl}}{t_{hkl}} = \frac{\Delta\lambda_{hkl}}{\lambda_{hkl}} \tag{5.2}$$

where θ^{B}_{hkl} is the Bragg angle, d_{hkl} is the measured lattice spacing, t_{hkl} is neutrons time-of-flight and λ_{hkl} neutrons wavelength [87,88]. The Eq.5.2 for lattice strain is very similar to that for the continuum engineering strain. However, it is important to remember that while

diffraction does allow probing the atomic lattice spacing with great precision, it has quite different characteristics from a conventional strain gauge. In fact, a great deal of information to engineers and materials scientists can be obtained from the behaviour of a diffraction peak profile from a sample under load, including its *shape, center* and *width.*

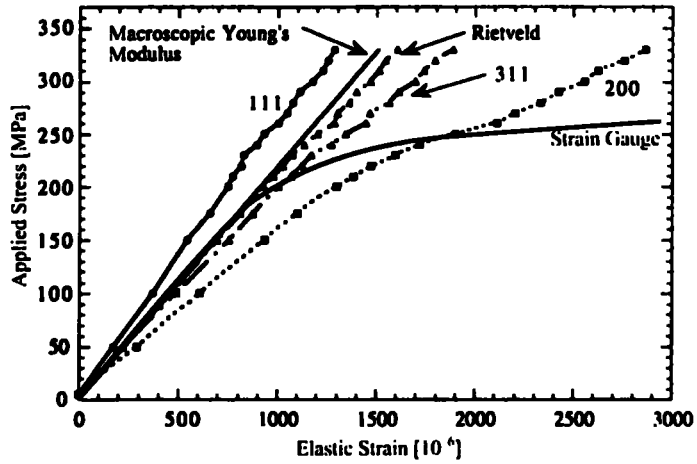

Figure 5.1: The elastic lattice strain response for austenitic stainless steel parallel to uniaxial loading as determined from individual peak analysis and by Rietveld analysis of the whole diffraction pattern [89].

It is essential for measurement and interpretation of strain data from a polycrystalline sample, especially in the process of converting Bragg peak angles into strains and then calculating stresses, to appreciate a highly selective nature of the diffraction technique. A single *hkl* diffraction peak is inherently associated with a subset, or family, of the grains within the sampled gauge volume, typically, of a few cubic millimetres. This subset consists of grains with *hkl* plane-normal oriented to the direction of the scattering vector $\boldsymbol{Q}$, and the technique thus provides very selective information. Strain variations occurring over a characteristic distance larger than the corresponding sampling gauge volume dimension are recorded as shifts in the angle or wavelength at which a diffraction peak is measured, whereas those having a characteristic length much shorter than the corresponding sampling gauge dimension, often termed ***microstrains*** (*Type II, Type III*, chapter 4), are evidenced by changes in the profile of the diffraction peak in width or/and shape. As a result, the angle representative of the center of the peak provides the lattice strain in this subset averaged over the gauge volume. That the lattice strain is proportional to the macroscopically applied stress, at least below the proportional (elastic) limit is evident in Fig.5.1. The consequence of the selective nature of the individual different reflections is also clear from the figure, which shows their different average lattice strain response from that of a conventional strain gauge to applied loading, even at low loads. The different slopes of the strain-stress curves for

particular reflection in Fig.5.1 before macroscopic plastic yielding are caused by so-called *elastic anisotropy*, arising from the different elastic properties of the various crystal lattice planes (see section 5.4) [89,90].

It is also clear from Fig.5.1 that unlike a conventional strain gauge, first-order lattice strains - which must be elastic by their nature - are not sensitive to macroscopic plastic strain. This is because plastic strain occurs by slip processes and the passage of dislocations through the crystalline lattice does not give rise to any increase in the lattice spacing *per se*. However, plastic strain can give rise to intergranular misfits leading to *Type II* (intergranular) stresses. As a result, lattice strain gives valuable information on the stress even in the plastic regime. Intergranular strains generated by plastic straining give rise to the non-linearities in the applied stress versus lattice strain curves. These non-linearities are due to the *plastic anisotropy* and also they need to be accounted for when interpreting (converting) diffraction strain data in terms of stresses [72,90,91].

5.3 FUNDAMENTAL RELATIONSHIP BETWEEN STRAINS AND STRESSES

Stress (σ_{ij}) and strain (ε_{ij}) are tensors quantities related one to another by the elastic stiffness tensor C_{ij}, and the elastic compliance tensor S_{ij}:

$$\sigma_{ij} = \sum_{kl} C_{ijkl}\varepsilon_{kl}, \text{ and } \varepsilon_{ij} = \sum_{kl} S_{ijkl}\sigma_{kl}, \tag{5.3}$$

where σ_{ij} and ε_{ij} have 9 components, 6 of which are independent, and C_{ij} and S_{ij} have 81 components, 36 of them can be independent [92-94]. Essentially, most engineering calculations are based on isotropic continuum mechanics. In this case, C_{ij} can be written in terms of just two independent elastic components, such as *Young's modulus*, E, and *Poisson's ratio*, ν. Consequently, the relationship between stress and strain can be expressed by using the generalized *Hooke's law*

$$\sigma_{ij} = \frac{E}{1+\nu}\left[\varepsilon_{ij} + \frac{\nu}{(1-2\nu)}(\varepsilon_{11}+\varepsilon_{22}+\varepsilon_{33})\right], \tag{5.4}$$

where i, j = 1,2,3 indicate the components of main directions [92-94].

The applied stress versus elastic strain response characteristic for each lattice plane family *hkl* is usually different (Fig.5.1), because in general, the stiffness (C_{ij}) of a single crystal in not isotropic. Therefore it is necessary to replace the continuum elastic strain Eq.5.4 with the lattice strain ε_{ij}^{hkl}, measured from the particular *hkl* reflection. And the isotropic values E, ν have to be also substituted in the generalized *Hooke's law* by the so-called *diffraction elastic*

constants (E_{hkl}, ν_{hkl}). Then, at least in the elastic loading regime, the strains ε_{ij}^{hkl} evaluated for each *hkl* reflection, can be converted to the macrostress component σ_{ij}^{I}

$$\sigma_{ij}^{I} = \frac{E_{hkl}}{1+\nu_{hkl}}\left[\varepsilon_{ij}^{hkl} + \frac{\nu_{hkl}}{(1-2\nu_{hkl})}(\varepsilon_{11}^{hkl} + \varepsilon_{22}^{hkl} + \varepsilon_{33}^{hkl})\right]. \tag{5.5}$$

The diffraction elastic constants (E_{hkl}, ν_{hkl}) for a polycrystal can be determined from calibration experiments in which a polycrystalline sample is subjected to known uniaxial loading (see experimental part) or they can be calculated by means of Voigt, Reuss or Kröner models (see section 5.4) [95,96].

For single crystal, the diffraction elastic constant (E_{hkl}) can be calculated from the values of elastic stiffness tensor C_{ij} and Miller indexes of the investigated *hkl* reflection. In the cubic system, i.e. for face-centered cubic, body-centered cubic, or primitive cubic we receive:

$$\frac{1}{E_{hkl}} = \frac{C_{11}+C_{12}}{(C_{11}-C_{12})(C_{11}+2C_{12})} - 2\left(\frac{1}{C_{11}-C_{12}} - \frac{1}{2C_{44}}\right)A_{hkl}, \tag{5.6}$$

where

$$A_{hkl} = \frac{h^2k^2 + h^2l^2 + k^2l^2}{(h^2+k^2+l^2)^2}, \tag{5.7}$$

is the orientation factor describing the direction of elastic response with respect to the crystal lattice axes. The elastic properties of the crystalline material are included in the Eq.5.6 by means of the elastic stiffness tensor C_{ij} [72].

5.4 ELASTIC RESPONSE OF hkl-REFLECTION IN A POLYCRYSTAL

The interpretation of the results of diffraction lattice strain measurements by means of the model predictions of the elastic response of the specific *hkl* reflections is very useful. As mentioned above, in the elastic region of deformation, we have to consider the plane-specific *Young's modulus*, E_{hkl} parallel to the applied uniaxial load, and *Poisson's ratio*, ν_{hkl} giving the strain measured perpendicular to the applied loading stress in terms of the strain measured parallel to the loading direction.

5.4.1 Voigt Model

The Voigt model is based on the assumption that all grains in a polycrystalline aggregate experience the same uniform strain (Fig.5.2) Therefore, it does not provide any orientation dependency, and all *hkl* reflections inherently render the same lattice strain response parallel

to the external load. Thus, *Young's modulus* and *Poisson's ratio* are isotropic and the same for all *hkl* reflection.

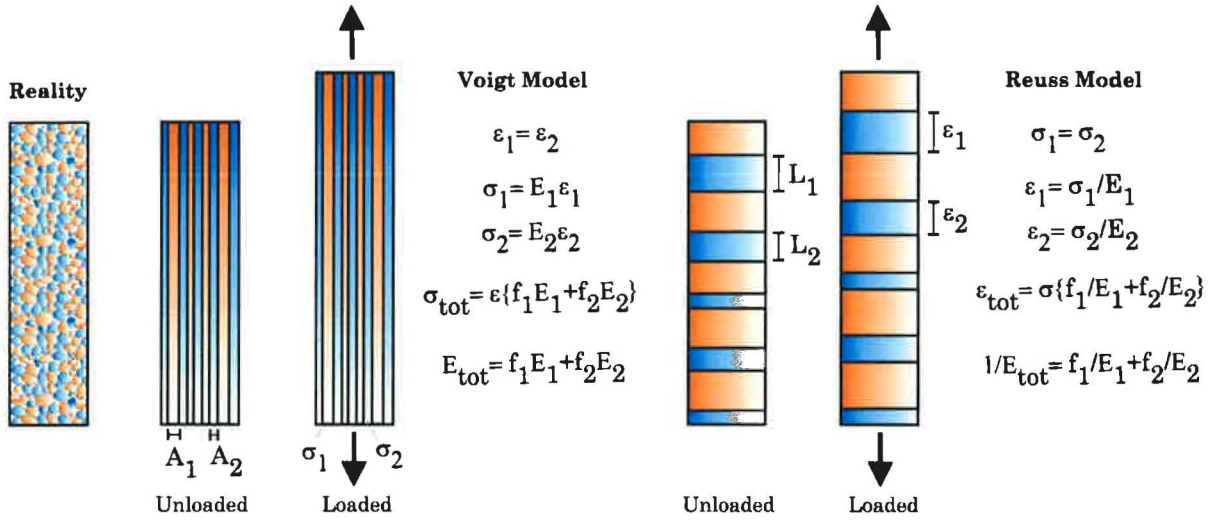

Figure 5.2: Principle of Voigt and Reuss model for the elastic behaviour of polycrystalline material under straining.

5.4.2 Reuss Model

Under assumption of the Reuss model, all crystallites experience the same stress (Fig.5.2). In order to determine the strain response to the applied uniaxial stress experienced by cubic crystallites giving rise to the *hkl* reflection, the contributions from all crystallites with *hkl* planes perpendicular to the [hkl] direction are averaged. Two important cases are distinguished when these *hkl* planes are perpendicular to the applied stress (i.e., when the lattice strain is measured in the loading stress direction, *axial direction*), and when the *hkl* planes contain the loading stress direction (i.e., when this is perpendicular to the [*hkl*] direction, *radial direction*) [72].

The polycrystalline average strain measured parallel to the applied uniaxial loading, $\varepsilon_{\parallel}^{hkl}$ is defined as

$$\varepsilon_{\parallel}^{hkl}(poly) = \sigma_{appl}(S_{11} - 2S_0 A_{hkl}), \tag{5.8}$$

where, σ_{appl} is the applied uniaxial stress, S_{11}, S_0 are values of the elastic compliance tensor S_{ij}, and A_{hkl} is defined by Eq.5.7 as the orientation factor. Then by using the *Hooke's law*

$$\sigma_{hkl} = E_{hkl}\varepsilon_{hkl}, \tag{5.9}$$

Young's modulus can be expressed by

$$E_{hkl}^{Reuss}(poly) = \frac{1}{(S_{11} - 2S_0 A_{hkl})}. \tag{5.10}$$

The strain response perpendicular to the loading stress, $\varepsilon_{\perp}^{hkl}$, is given by

$$\varepsilon_{\perp}^{hkl}(poly) = \sigma_{appl}(S_{12} + S_0 A_{hkl}). \tag{5.11}$$

Poisson's ratio relating the lattice strains perpendicular and parallel to the loading stress can be written as:

$$\nu_{hkl}^{Reuss}(poly) = -\frac{\varepsilon_{\perp}^{hkl}(poly)}{\varepsilon_{\parallel}^{hkl}(poly)} = -\frac{(S_{12} + S_0 A_{hkl})}{(S_{11} - 2S_0 A_{hkl})}. \tag{5.12}$$

5.4.3 Kröner Model

In contrast to the idealized approaches of Voigt and Reuss which assume either the strain or the stress to be identical in all constituents of the aggregate, the Kröner model allows both stresses and strains to vary from grain-to-grain. In the self-consistent scheme proposed by Kröner [97], it is merely suggested that the whole aggregate is exposed to a specific homogeneous average stress field and an associated homogeneous average strain field. An expression for the strain component in a specific sample direction, the measurement direction [*hkl*], is found by averaging this strain over contributing crystallites with all orientations in the plane perpendicular to this direction. This is related to the average stress in a similar way to that one used for the bulk response [98].

THE GOAL OF THE PROJECT

The motivation of the present work lies in a better understanding of the deformation and transformation processes taking place within thermally or/and mechanically treated single and multiphase steels (e.g. TRIP-aided multiphase steels, duplex stainless steels and single ferritic steels). Since thermal neutrons provide a possibility to obtain otherwise inaccessible information from bulk of crystalline materials, in this investigation, the recently developed *in situ* neutron diffraction technique has been employed as a main experimental tool. This unique application of neutron diffraction helps us to characterize the deformation and transformation processes occurring in steels during thermo-mechanically controlled processing. In order to obtain complex information on macroscopic and microscopic processes in treated steels the neutron diffraction results are supported by microstructural observation by the light microscopy (LM) and scanning electron microscopy (SEM).

The project consists of the three major parts. The first part is dedicated to the *in situ* investigation of the thermo-mechanically controlled processes (TMCPs) of low-alloyed (i.e. Nb-added, Nb-free and Si-Mn) steels. The partial tasks were defined as follows:

- study of the austenite-to-ferrite phase transformation kinetics by mean of the evaluation of the changes in the integrated intensity of austenite and ferrite diffraction profiles recorded during application of specific thermo-mechanical treatment
- evaluation of the changes in the lattice spacing of austenite and ferrite phases as a function of temperature during applied TMCPs in single ferritic, single austenitic and dual phase (austenite/ferrite) regions
- optimization of the temperature and isothermal holding time criteria of the austenite-to-ferrite phase transformation in TMCP of low-alloyed Si-Mn TRIP-aided steels.

The second part is devoted to the *in situ* neutron diffraction investigation of the deformation and transformation behaviour of low-alloyed (Si-Mn) TRIP-aided multiphase steels at room temperature, namely:

- transformation kinetics investigation of the strain-induced martensitic transformation of the retained austenite upon tensile deformation
- evolution of the interphase strains/stresses and load redistribution between phase constituents in TRIP-aided steels in the course of tensile testing

- interpretation of the relation between interphase load redistribution and the kinetics of the strain-induced martensite transformation of the retained austenite
- generation of the intergranular strains/stresses between differently oriented grains of the individual phase constituents.

The last part of the project is devoted to the *in situ* neutron diffraction investigation of the deformation behaviour of single ferritic and duplex stainless steels. Investigation has been namely focused on:

- evaluation of lattice strains in the course of tensile testing in both tested steels as well as in both phase constituents in duplex stainless steel
- study of the generation of intergranular residual strains/stresses in single ferritic steel as a function of accumulated plastic strain
- evaluation of the changes in the width (FWHM) of diffraction profiles upon loading (unloading) and corresponding changes in the dislocation density during elastic and plastic deformation
- investigation of the effect of initial (thermal) and final (deformation) residual strains in both phase constituents present in duplex stainless steel on the mechanical properties of the alloy and individual phases (ferrite, austenite).

6.

THERMO-MECHANICALLY CONTROLLED PROCESSING (TMCP)

The beneficial contributions of TMCP to steels properties persuaded us to use *in situ* neutron diffraction technique to study steels upon thermal and/or mechanical treatment. This study has been particularly concerned on the evolution of steel microstructure during the applied TMCP (section 6.1) and to the optimization of TMCP for producing low-alloyed (Mn-Si) TRIP-aided multiphase steel as a bulky material (section 6.2).

6.1 INVESTIGATION OF TMCP OF LOW-ALLOY STEELS

Though a lot of literatures involved in the effects of TMCP and microalloying on the formation mechanism of ultra-fine grained ferrite, the *in situ* characterization of microstructure evolution and phase strain during the austenite-to-ferrite transformation is still urgently demanded as a direct proof to well clarify why the deformation can induce dynamic ferrite transformation. Therefore, in this study, the austenite-to-ferrite transformation characteristics were investigated by *in situ* neutron diffraction. However, the neutron diffraction is the unique technique to identify such microstructure evolution during phase transformations the beam intensity is usually too weak to follow a rapid transformation in low carbon steel. On that account, in our case 2% Mn (Tab.6.1) was added to make austenite-to-ferrite transformation slower. Based on the *in situ* investigation in the course of the thermo-mechanical treatment, critical phase transformation temperatures, phase volume fractions and the evolution of phase lattice spacing were determined. In addition to this, the effects of Nb addition and austenite prior deformation were also studied by the neutron diffraction.

Table 6.1: Chemical composition of two investigated steels (wt. %)

	C	Si	Mn	Nb	Ni
Nb-free	0.19	0.01	1.95	< 0.002	< 0.01
Nb-added	0.19	0.01	1.97	0.03	< 0.01

6.1.1 Experimental Material

Two low-alloyed Nb-free and Nb-added steels have been chosen as an experimental material to compare the beneficial influence of Nb addition on austenite-to-ferrite

transformation kinetics during applied TMCP. As mention before, both investigated steels contain a higher content of manganese in order to slow down the austenite-to-ferrite phase transformation (Tab.6.1).

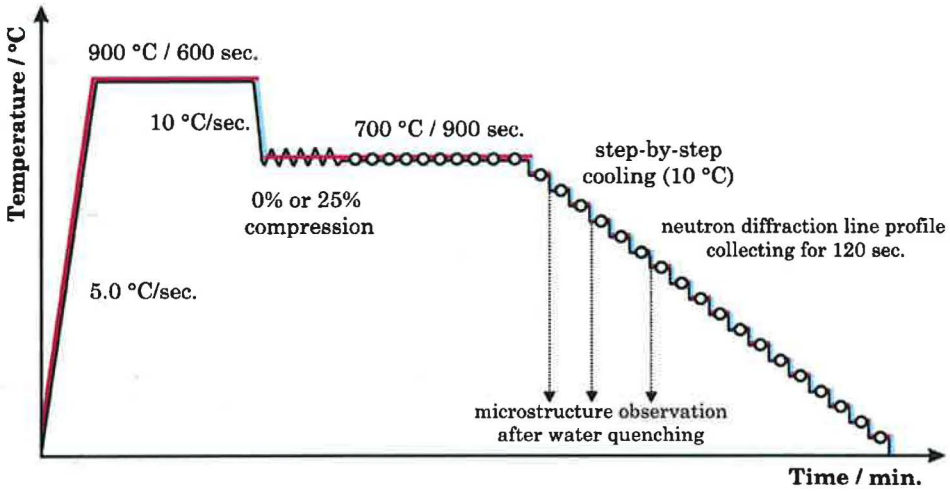

Figure 6.1: A thermo-mechanically controlled process (TMCP) schedule employed in two kinds of performed experiments.

6.1.2 Experimental Procedures

Two 14×14mm^2 caliber-rolled steels were quenched after the solution treatment at 900 °C for 30 min. to obtain a single martensite starting microstructure. Since the specimen after neutron diffraction can not be employed directly to examine the metallurgical microstructure, two kind of TMCP experiments were performed by using the two relevant machines:

1. the *in situ* neutron diffraction measurement, and
2. microstructure observation after quenching specimens at different stages of TMCP by means of scanning electron microscopy (SEM).

A common TMCP schedule (Fig.6.1) comprises heating up to 900 °C with a heating rate of 5 °C/sec. and holding time for 10 min. to obtain a single austenite microstructure. The specimen was then cooled down to 700°C with a rate of 10 °C/sec. followed by deformation 0% or 25% in compression before the onset of austenite-to-ferrite transformation, and isothermal holding at 700 °C for 15 min. The step-by-step cooling with 120 sec. holding per each 10°C increment was finally applied (see Fig.6.1).

6.1.2.1 *In situ* neutron diffraction experiment on the TKSN-400 at NPI

The *in situ* diffraction experiments were performed at the Nuclear Physics Institute in Řež on the diffractometer TKSN-400 installed at horizontal neutron channel HK-9 (Fig.6.2) of the LVR-15 reactor. The white incident beam coming out of the reactor core is monochromatized

by $\{220\}_{Si}$ lattice plane of silicon single crystal providing the wavelength of 0.23 nm. For the most effective utilizing of intensity of the incident neutron beam, the horizontally curved monochromator is used for focusing incident neutron beam, provide thus an excellent resolution of $\Delta d_{hkl}/d_{hkl} = 2\times10^{-3}$ [3,4]. The diffractometer is equipped with a special deformation rig for tension/compression loading up to the force of ±20 kN. The applied force is directly measured by loading cell (Fig.6.3) whereas the actual strain of the investigated specimen is recorded by means of an extensometer (clip gauge) fitted on specimen surface (except high-temperature tests) and macroscopic strain is recorded simultaneously by a digital micrometer (Fig.6.3).

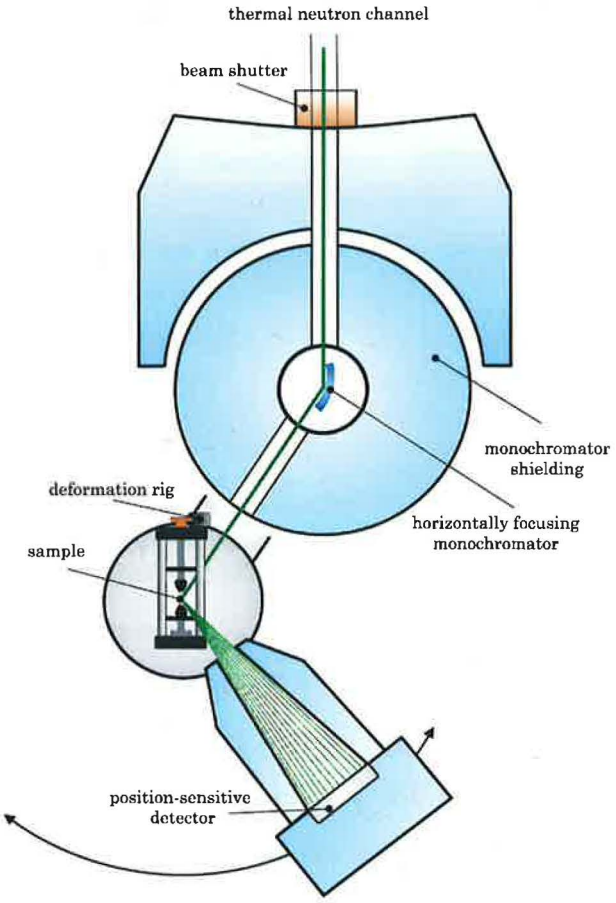

Figure 6.2: High-resolution stress/strain diffractometer TKSN-400 at Nuclear Physics Institute in Řež.

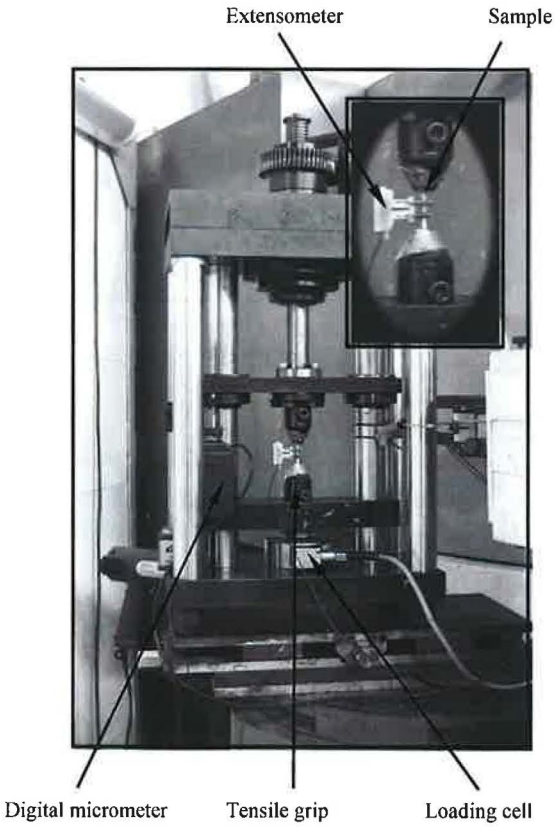

Figure 6.3: Tensile rig assembled at diffractometer TKSN-400 at Nuclear Physics Institute in Řež.

The resistant heating system is mounted directly to the water-cooled and modified grips of the deformation machine (Fig.6.4). The maximum electric power of the heating system is 3.5 kW, the specimens are heated by the electrical current up to of about 1.5 kA enabling thus the heating of the metallic specimens up to temperatures about 1000°C. By using the EUROTHERM thermocontroller and two thermocouples, a relatively good temperature

stability of ±0.5°C in overall working temperature range has been reached. The diffractometer, testing rig and heating/cooling system are fully PC controlled by the SCP program which enables very flexible measuring schemes and their independent operations. The adjustable positioning of the deformation rig and its dimensions enable *in situ* measurements of all components of the stress/strain tensor. This high-resolution stress/strain diffractometer is dedicated for *in situ* investigations of the deformation processes in different kinds of metallic materials e.g. steels, aluminium, shape-memory alloys. The neutron diffraction patterns are recorded by a linear position-sensitive detector (PSD) (Fig.6.2) which enables fast acquisition of the diffraction data in a relatively narrow 2θ band of about the 2θ = 7° with high instrumental resolution. The PSD detector can be set to any position in the range from 20° to 85° of the 2θ scattering angle [3,4].

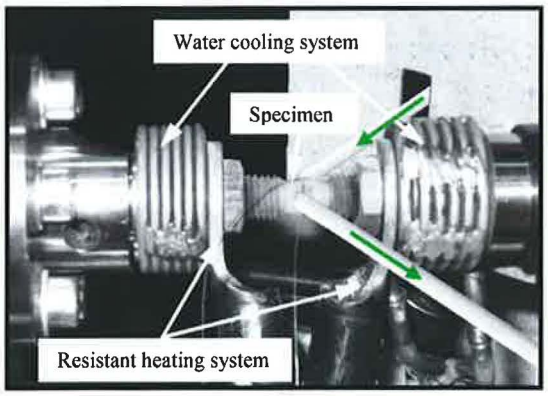

Figure 6.4: In-situ neutron diffraction experiment on TKSN-400 at NPI in Řež.

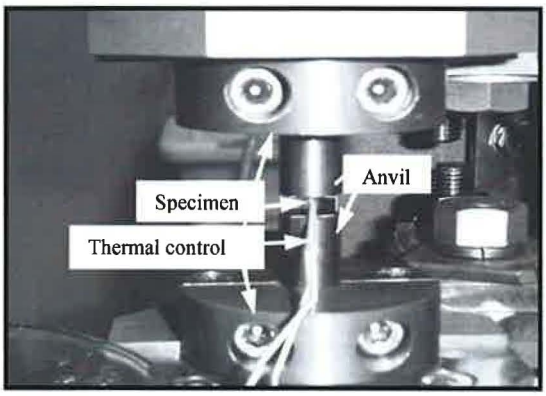

Figure 6.5: Microstructure examination by using hot-compression tester.

For present *in situ* neutron diffraction experiments, the TMCP specimens with 7mm in gauge diameter and 14 mm in gauge length were machined. No protective atmosphere was used during all the TMCP tests since the useful signal was collected from the whole irradiated gauge volume. The neutron diffraction spectra of austenite $\{111\}_\gamma$ and ferrite $\{110\}_\alpha$ peaks were collected during the temperature holding simultaneously and for this purpose the PSD window was set to $2\theta = 68^o$ (Fig.6.8).

6.1.2.2 Modifications of the TKSN-400 for *in situ* TMCP experiments

In order to perform *in situ* neutron diffraction experiments during the application of various TMCP, some necessary modifications of the TKSN-400 diffractometer had to be done. At first, the deformation rate was considerably modified as is seen in Fig.6.6. The initial maximum rate of 63 $\mu m.s^{-1}$ (red) was successfully increased almost three times to the final 180 $\mu m.s^{-1}$ (blue) (Fig.6.6). Besides the deformation rate the temperature stability, during

TMCP is also very important. As it is seen in Fig.6.7a there was problem with temperature stability during deformation, mainly caused by losing the thermocouples electric contact with deformed material. To reduce this unwelcome effect, some settings modifications in thermocontroller (EUROTERM) was done, but the most important was to change the thermocouples welding method. Instead of welding thermocouples directly on the sample surface, a small hole was drilled to the specimen body and the thermocouples were welded into this hole (Fig.6.7b). Finally, the excellent temperature stability of ±0.5 °C had been achieved even during deformation process (Fig.6.7a, blue)

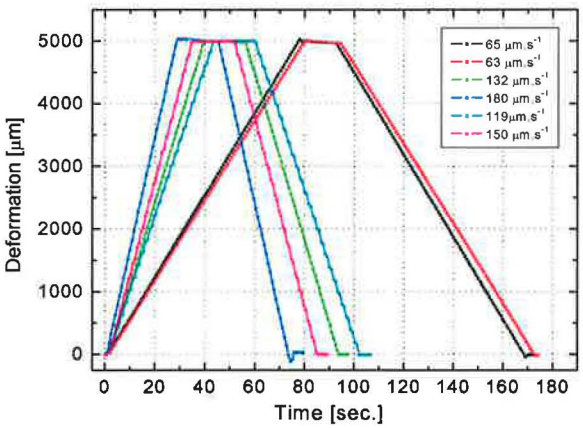

Figure 6.6: Modification of the deformation rate for *in situ* thermo-mechanically controlled processes at high-resolution diffractometer TKSN-400 at NPI.

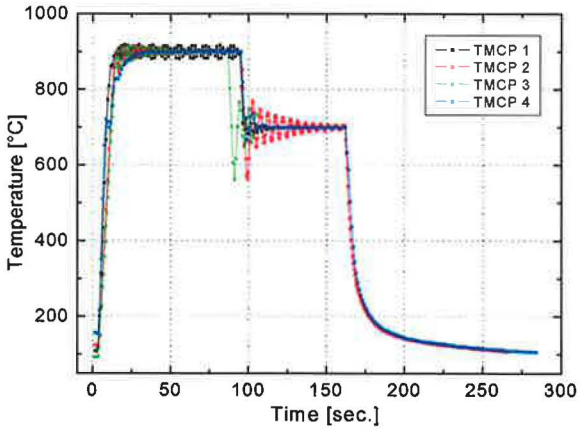

Figure 6.7a: Examples of temperature record during tested thermo-mechanically controlled processes

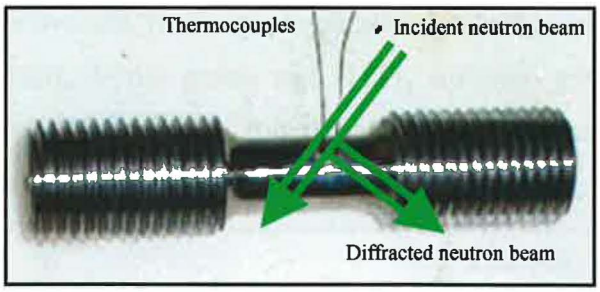

Figure 6.7b: Specimen for TMCP with thermocouples welded into the hole in sample body.

6.1.2.3 Microstructural observations

Columnar specimens for microstructural observation were manufactured with 6 mm in length and 4 mm in diameter by spark cutting. The TMCP experiments on these samples were performed by using a newly developed hot-compression tester with a heating system of direct electrical resistance (Fig.6.5). During the TMCP, the cooling process was interrupted at different stages and the specimen was immediately quenched into water. The TMCP interrupted microstructures at the volume center of specimen were observed with the optical

microscopy and the scanning electronic microscopy (SEM). The volume fraction of transformed ferrite was evaluated by combining the ASTM linear intercept method and the direct area ratio method with the JEOL SemAfore software between the ferrite area summation and the entire image area. These microstructural observations were performed in collaboration with Professor Y. Tomota at Ibaraki University in Hitachi, Japan [99]. The ferrite volume fraction determined by means of SEM observations was compared with the results obtained from the neutron diffraction profiles measurement (see below).

6.1.3 Austenite-to-Ferrite Phase Transformation upon TMCP

6.1.3.1 Microstructure evolution analyzed by *in situ* neutron diffraction

The typical changes in neutron diffraction profiles of austenite $\{111\}_\gamma$ and ferrite $\{110\}_\alpha$ reflections collected during the austenite-to-ferrite phase transformation can be seen in Fig.6.8. Although the obtained neutron diffraction profiles are a little rough due to the weak neutron beam and the limited profile-collecting time per step, their quality is good enough to characterize the microstructure evolution during TMCP. During the step-by-step cooling, the increase in ferrite diffraction intensity and the decrease in austenite diffraction intensity reveal that the austenite gradually transforms into ferrite while the shifts of diffracted peaks to the larger Bragg angles reveal the thermal contraction of crystalline lattice of both phases. By using the Gaussian curve fitting, the relevant parameters about the austenite-to-ferrite transformation can be extracted from the integrated intensities and angular positions of individual profiles of $\{110\}_\alpha$ ferrite grains and $\{111\}_\gamma$ austenite grains. Here the integrated intensity of ferrite peak was assumed as a function of the ferrite volume fraction and the peak position was employed to estimate the lattice plane spacing.

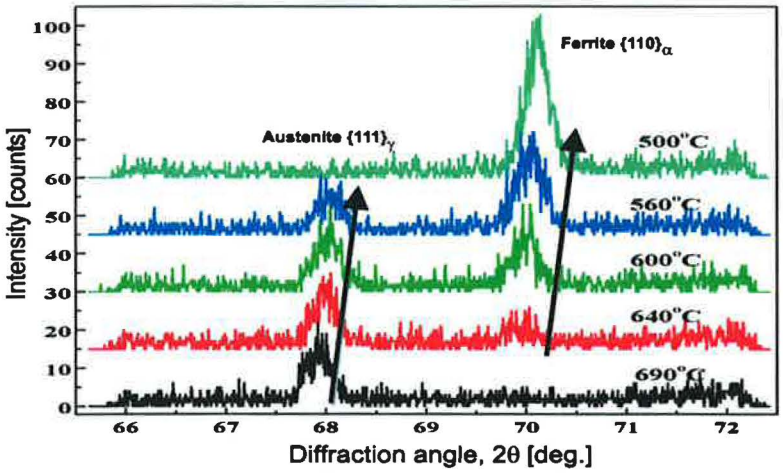

Figure 6.8: Neutron diffraction profile changes of austenite $\{111\}_\gamma$ and ferrite $\{110\}_\alpha$ reflection of non-deformed Nb-added steel during austenite-to-ferrite phase transformation.

Considering the existence of the temperature effect of neutron elastic and inelastic scattering due to the atomic thermal vibration around the atomic sites and due to the energy loss of inelastic collision between the neutron and the nuclei [72,100], the temperature calibration of ferrite **{110}$_\alpha$** diffraction intensity has to be carried out before the further austenite-to-ferrite transformation evaluation based on the neutron diffraction profiles.

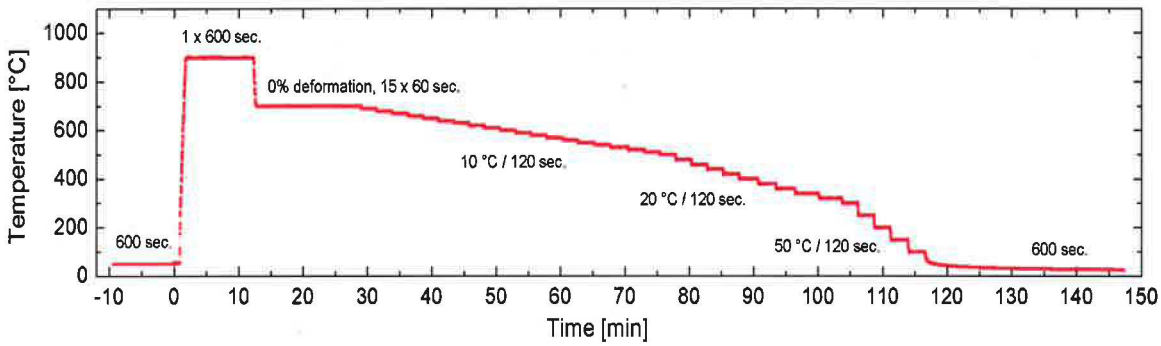

Figure 6.9: The temperature record during thermo-mechanically controlled processing of Nb-added low-alloyed steel.

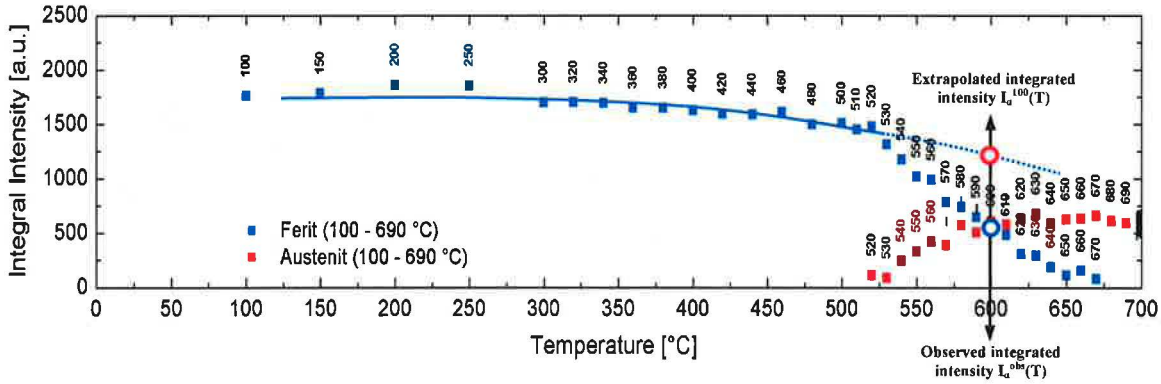

Figure 6.10: Estimation of ferrite volume fraction during austenite-to-ferrite phase transformation based on the integrated intensities of neutron diffraction profiles.

Fig.6.10 shows the changes in the integrated intensity of ferrite **{110}$_\alpha$** and austenite **{111}$_\gamma$** during the step-by-step cooling (Fig.6.9). At a certain temperature in the austenite/ferrite (γ/α) dual phase region, the integrated intensity $I_\alpha^{100}(T)$ extrapolated from those in the ferrite single phase region at low temperature was assumed to correspond to the maximum ferrite volume fraction after the entire ferrite transformation ($I_\alpha^{obs}(T)$ is the observed intensity of the ferrite **{110}$_\alpha$** diffraction profile), then the volume fraction of transformed ferrite was estimated as,

$$f_\alpha^{dif}(T) = I_\alpha^{obs}(T) / I_\alpha^{100}(T). \qquad (6.1)$$

The volume fractions of transformed ferrite estimated from the diffraction profiles were plotted in Fig.6.11. It is found that both of the prior austenite deformation and the niobium

addition enhance the starting temperature of austenite-to-ferrite transformation, which is consistent with the published paper [101].

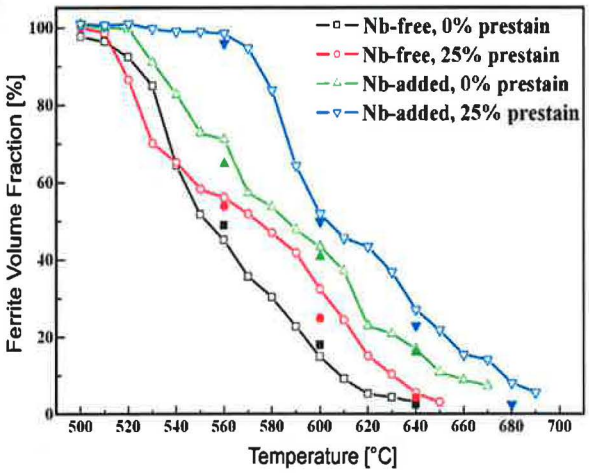

Figure 6.11 Changes in ferrite volume fraction analyzed from the neutron profile (in open marks) and measured from the TMCP-interrupted specimens (solid marks) during the step-by-step austenite-to-ferrite phase transformation.

6.1.3.2 Effect of austenite deformation on ferrite transformation kinetics

Since the ferrite volume fraction are here thought as the ratio between the measured integrated intensity and the ideally 100%-transformed integrated intensity extrapolated from those in the ferrite single phase region, the weak austenite texture due to the limited deformation has no apparent influence on the statistic accuracy of newly transformed ferrite. For the changes in ferrite volume fraction during the austenite-to-ferrite transformation as shown in Fig.6.11, a single transition curve can be found in the case of non-deformed steels and a double transition curve in the case of deformed steels. The deviation of the increment trend of ferrite amount from the dashed line in Fig.6.12 reveals that certain austenite stabilization occurs in the deformed steels after the partial ferrite transformation. In fact, such shape difference in kinetics transition curves between deformed and non-deformed steels also occurs during the dilatometry testing [102,103]. Though there are several possibilities including the phase stresses, the carbon enrichment and so on, no reason has already been confirmed to determine the above austenite stabilization.

According to the diffusion & interface mobility mixed control model [104], if the overall carbon concentration of the austenite is not much larger than the carbon concentration in the newly formed ferrite, the diffusion of the expelled carbon atoms will be a relatively fast process and the kinetics of the ferrite transformation will be largely interface controlled; if the overall carbon concentration of the non-transformed austenite is near to its equilibrium composition, the carbon diffusion will be sluggish and the transformation will be diffusion

controlled. Therefore, a possible explanation about the above austenite stabilization is proposed as follows: The prior austenite deformation accelerates the carbon diffusion through the dislocation substructures near the grain and subgrain boundaries and promotes the formation of newly ferrite grains; the rapid growth of ferrite grains leads to a large concentration difference between the austenite at the ferrite/austenite interface (i.e. carbon-rich region) and the remainder austenite (i.e. relatively carbon-poor region). In the carbon-poor region of austenite grains with specific orientations, the ferrite grains can preferably nucleate or grow through the rapid diffusion. Once the relatively carbon-poor region is consumed, the ferrite grains decrease its nucleation rate or/and growth rate due to the slow carbon diffusion, that is to say, the austenite stabilization occurs. If the austenite is continuously deformed (just like that in the dynamic transformation) or not deformed at all, the austenite stabilization will be difficult to observe.

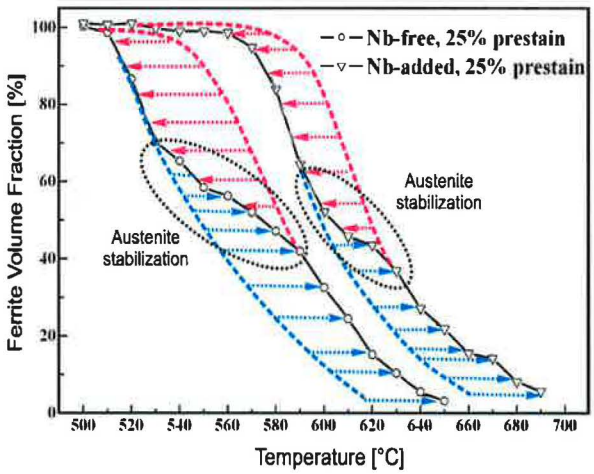

Figure 6.12: Double transition curve occurred in the deformed steels during austenite-to-ferrite transformation.

6.1.3.3 Microstructure evolution analyzed in the TMCP-quenched specimens

The ferrite morphology characteristics in the transformed products by quenching from 680 °C, 640 °C and 560 °C, respectively, are documented in (Fig.6.13, Fig.6.1 and Fig.6.15). By means of SEM observations, a few small ferrite grains (marked with red circles in Fig.6.13d) can be observed in the triple-joint boundary corner of the prior-deformed Nb-added specimen while single martensite microstructures appear in the other three specimens quenched from the same temperature of 680°C (Fig.6.13a,b,c). When evaluating the average length of martensite laths in the prior austenite grains they are finer in Nb-added specimens than those in Nb-free ones, this indicates that the Nb addition is very effective in refining the austenite grains. At the beginning of austenite-to-ferrite phase transformation (e.g. at 640 °C), the

ferrite grains mostly nucleate and grow along the prior austenite grain boundaries, especially in the deformed specimen where the prior austenite grain boundaries were clearly marked by the allotriomorphic ferrite grains (Fig.6.14b,d). Comparing the microstructures of deformed and non-deformed steels, it can be clearly seen that the prior austenite deformation increases the grain/sub-grain boundary area as ferrite nucleation sites, promotes the nucleation of ferrite grains and finally refines the ferrite grains.

Nb-free low-alloyed steel

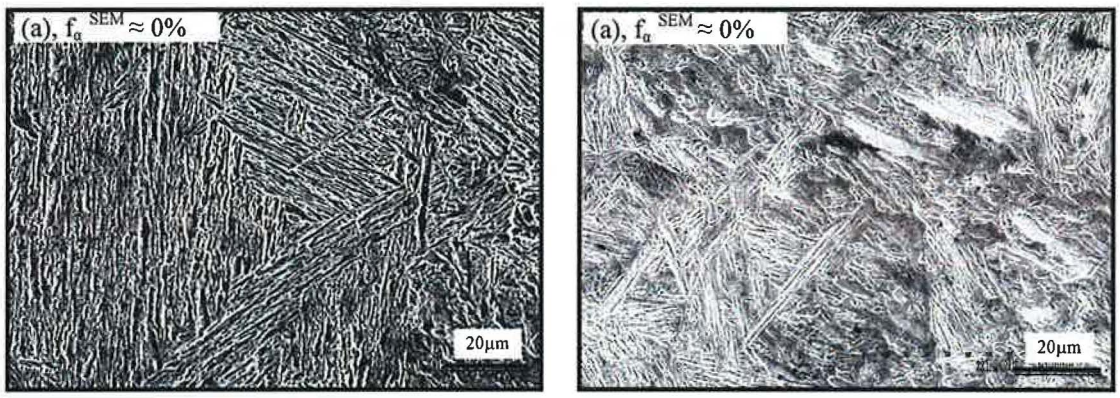

Figure 6.13a,b: Microstructure observation of 680 °C – quenched specimens **(a)** no austenite pre-strain and **(b)** 25% austenite pre-strain.

Nb-added low-alloyed steel

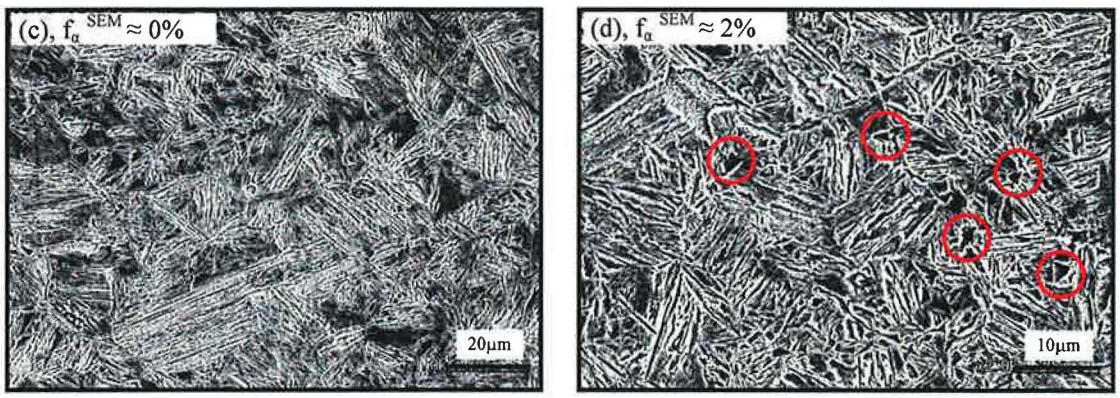

Figure 6.13c,d: Microstructure observation of 680 °C – quenched specimens **(c)** no austenite pre-strain and **(d)** 25% austenite pre-strain.

Nb-free low-alloyed steel

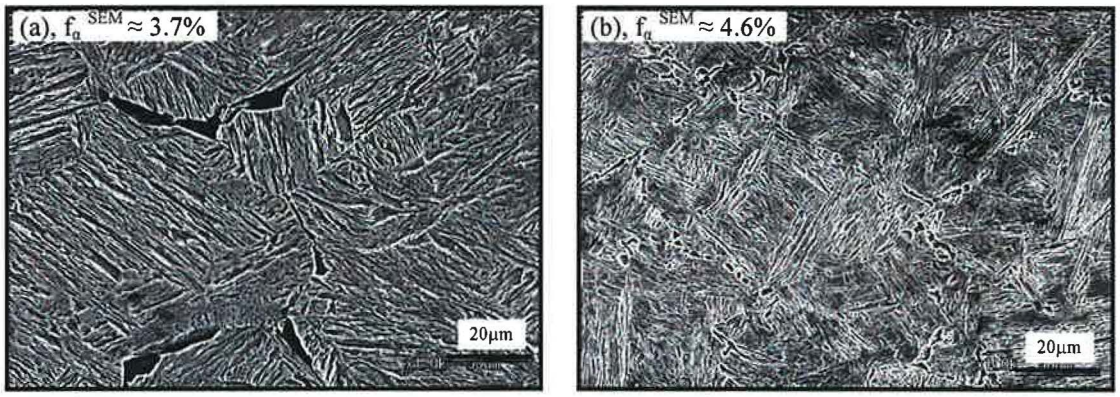

Figure 6.14a,b: Microstructure observation of 640 °C – quenched specimens **(a)** no austenite pre-strain and **(b)** 25% austenite pre-strain.

Nb-added low-alloyed steel

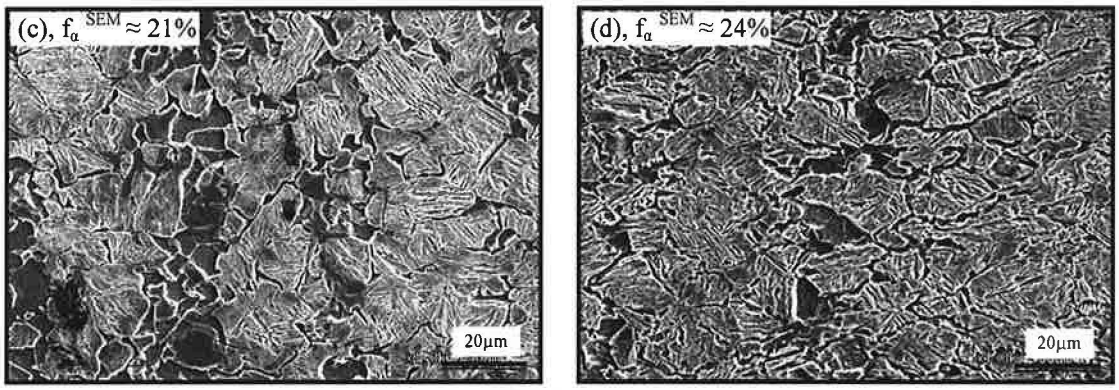

Figure 6.14c,d: Microstructure observation of 640 °C – quenched specimens **(c)** no austenite pre-strain and **(d)** 25% austenite pre-strain.

Nb-free low-alloyed steel

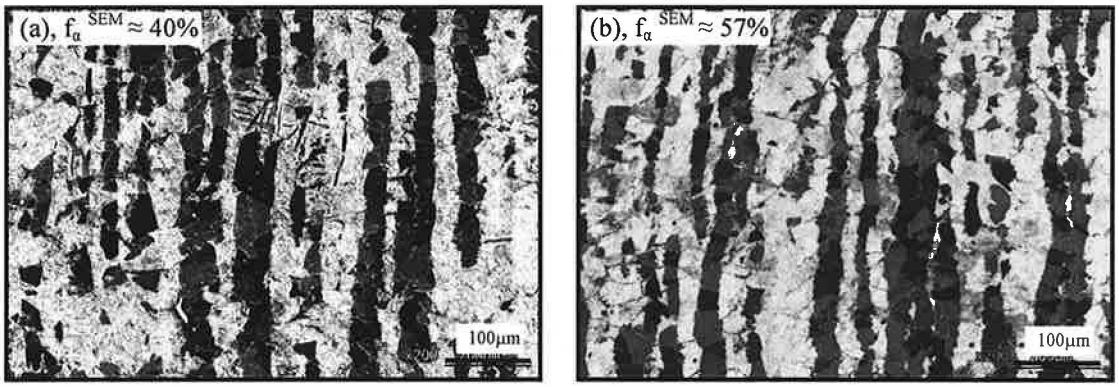

Figure 6.15a,b: Microstructure observation of 560 °C – quenched specimens **(a)** no austenite pre-strain and **(b)** 25% austenite pre-strain.

Nb-added low-alloyed steel

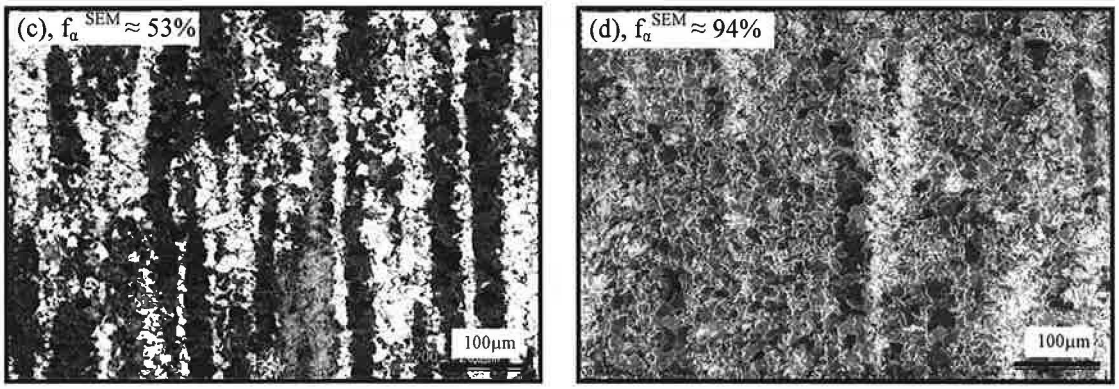

Figure 6.15c,d: Microstructure observation of 560 °C – quenched specimens **(c)** no austenite pre-strain and **(d)** 25% austenite pre-strain.

Taking into account the statistic error of about 5%, the ferrite volume fractions estimated from the *in situ* neutron diffraction experiment (f_α^{dif}) is in a good agreement with the ones obtained from the TMCP interrupted microstructures (f_α^{SEM} , solid marks in Fig.6.11). For example, f_α^{SEM} at 560 °C in the deformed Nb-added and Nb-free steels are of about 94% and 57%, which confirm the assumptions on the austenite stabilization (see Fig.6.13-15 and Fig.6.11, Fig.6.12).

6.1.3.4 Changes in lattice plane spacing during the TMCP

The changes in lattice plane spacing of austenite and ferrite during TMCP are shown in Fig.6.16, Fig.6.17 as a function of temperature. The austenite exhibits a linear thermal expansion in the single phase region; on the other hand, a non-linear thermal expansion occurs in the dual phase region due to the carbon enrichment in austenite. Moreover, it is also found that there is a limit for the thermal expansion deviation.

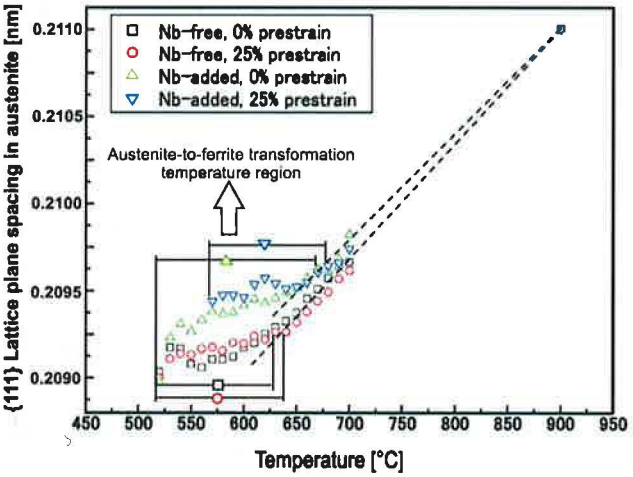

Figure 6.16: Measured lattice plane spacing in austenite phase during thermo-mechanically controlled process.

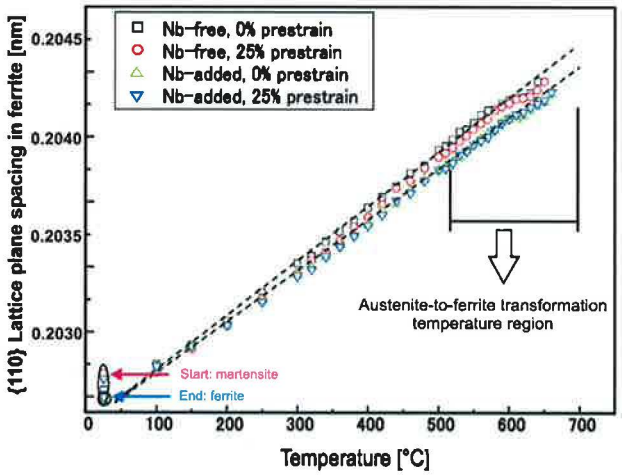

Figure 6.17: Measured lattice plane spacing in ferrite phase during thermo-mechanically controlled process.

This phenomenon should be ascribed to that the carbon concentration in austenite can not be further enriched once the austenite begins to decompose into pearlite (i.e. the ferrite and the cementite). It should be mentioned here that at the above austenite stabilization temperature region, the carbon concentration in austenite still increases which reveals that the austenite stabilization really occurs during the ferrite transformation. In addition, the austenite non-linear expansion started from a higher temperature in the Nb-added steels than that in the

Nb-free steels can easily confirm that the niobium addition enhances the ferrite transformation onset temperature to a certain extent.

In the austenite/ferrite (γ/α) dual phase region, the ferrite phase also shows a non-linear deviation form the linear thermal expansion occurred in the low temperature ferrite/cementite phase region, which proves that the internal stresses are generated during the ferrite transformation. Relative to the ferrite lattice spacing at 25 °C after TMCP, the evident different lattice spacing obtained form the martensite starting microstructure suggests a large phase strain, which can be employed to describe the martensite transformation characteristics of low-alloyed steels.

However, it is difficult to directly evaluate the three misfit strains occurred during the austenite-to-ferrite transformation, i.e. the thermal expansive misfit strain, the carbon enrichment misfit strain and the transformation misfit strain [105]. The proper modelling calculation to evaluate the phase stresses during the ferrite transformation will be developed on the basis of these and additional *in situ* neutron diffraction experiments in the near future.

6.1.4 Brief Summary

The austenite-to-ferrite transformation evolution of two low-alloy steels and the effects of Nb addition and austenite deformation were investigated by the *in situ* neutron diffraction. The transformation kinetics were determined from the measured intensities of neutron diffraction, these data are in a good consistence with the measured ferrite volume fractions from the metallographic microstructures quenched from the corresponding temperatures, which reveals that the *in situ* neutron diffraction can be satisfactorily applied to investigate the bulky microstructure evolution during the thermo-mechanically controlled process. The lattice changes both in the single austenite (or ferrite) region and in the dual phase region were also evaluated from the neutron diffraction profiles. The niobium addition and austenite pre-deformation were confirmed to promote the ferrite transformation. The deformed and non-deformed austenite microstructures were found to exhibit distinguishable shape difference in their transition curves.

6.2 TMCP OPTIMIZATION OF TRIP-AIDED MULTIPHASE STEEL

The optimization of mechanical properties of low-alloyed steels can be achieved either by the additional alloying (Ni, Cr, Mo etc.) or by thermo-mechanically controlled processing (TMCP). From the economical point of view, additional alloying is usually more expensive option in comparison to the application of the specific TMCP. Therefore a lot of effort has

been paid to find an appropriate TMCP to produce steels with an excellent balance of strength and ductility. Especially, development of TMCP has been recently focused on employing the effect of the strain-induced transformation (TRIP, TRansformation-Induced Plasticity effect) which occurs in steel containing a specific amount of the metastable austenite.

For purpose of manufacturing the TRIP-aided multiphase steel containing a significant volume fraction of the retained austenite, the austenite-to-ferrite phase transformation of selected low-alloyed Si-Mn steel has been studied (Tab.6.2). This high-temperature phase transformation has been studied during isothermal exposure at different transformation temperatures by *in situ* neutron diffraction technique. On the basis of the all performed *in situ* investigations during the isothermal austenite-to-ferrite phase transformation, optimal transformation temperature, and volume fraction of ferrite and non-transformed austenite with respect to austenite conditioning were determined.

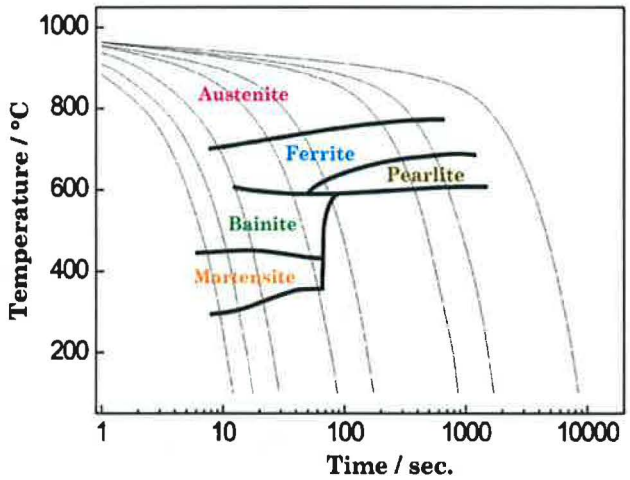

Figure 6.18 Continuous cooling transformation (CCT) diagram of used low-alloyed Mn-Si steel

Table 6.2: Chemical composition of the used steel (wt. %)

C	Mn	Si	P	S	Cr	Ni	Cu	Al	Nb
0.19	1.45	1.9	0.02	0.02	0.07	0.02	0.04	0.02	0.003

6.2.1 Characterisation of Used Low-Alloyed Si-Mn Steel

As an experimental material has been chosen low-alloyed (Si-Mn) steel with chemical composition tabled in Tab.6.2. This chemical composition has been proposed with respect to promote austenite stabilization and suppress the carbide precipitation during applied thermo-mechanically controlled processing. Therefore, this experimental steel contains high content of the most important direct austenite stabilizers as manganese and carbon, which strongly

influence the retained austenite stability at low temperature (section 2.7). Since, the presence of so-called indirect austenite stabilizer as silicon is also irreplaceable in the process of austenite retention this experimental steel contains its higher amount as well.

The continuous cooling transformation (CCT) diagram for this experimental steel is shown in Fig.6.18 [106]. The microstructures produced at controlled cooling rates are generally represented on CCT diagram, because it expresses variety of present microstructural phases in final steel structure with respect to cooling rate [107]. The CCT diagram is essential for suggesting the appropriate TMCP for particular low-alloyed TRIP-aided steel.

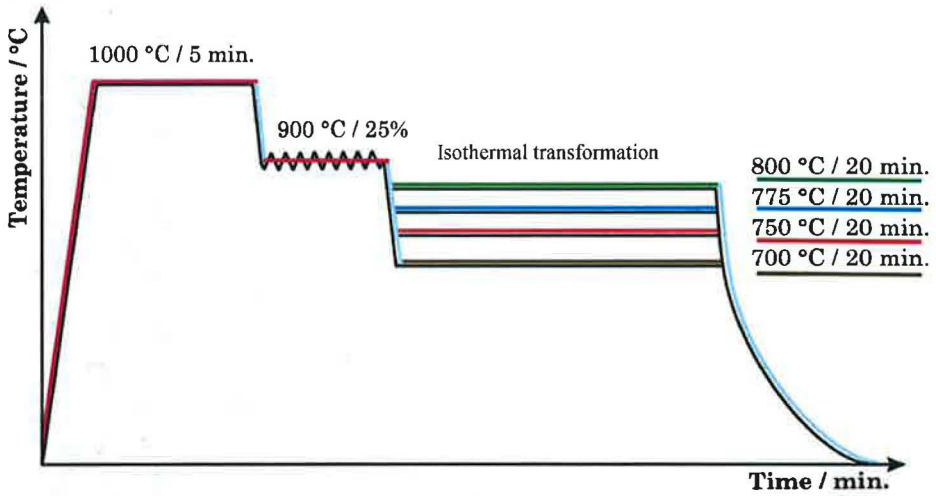

Figure 6.19 Experimental thermo-mechanically controlled processes (TMCP) for low-alloyed Mn-Si steel, applied in order to examine the effect of different temperature of isothermal transformation.

6.2.2 Experimental Procedure

Four low-alloyed Si-Mn steel (Tab.6.2) specimens (**A**, **B**, **C**, **D**) with 6 mm in gauge diameter and 15 mm in gauge length were machined for the present *in situ* high-temperature neutron diffraction experiments on the dedicated diffractometer, TKSN-400, at NPI in Řež (section 6.1.2.1). A common experimental thermo-mechanical processing of specimens (**A**, **B**, **C**, **D**) consists of heating to solution temperature of 1000 °C for 5 min. and cooling to 900 °C followed by 25% compressive deformation (Fig.6.19). Consequently, the temperature of each specimen was decreased to the different transformation temperatures (T_t) of

- T_t = 700 °C for sample **A**
- T_t = 750 °C for sample **B**
- T_t = 775 °C for sample **C**
- T_t = 800 °C for sample **D**, respectively.

These transformation temperatures (T_t) were derived from the austenite-to-ferrite transformation temperature region according to the CCT diagram of the experimental steel

(Fig.6.18). Holding time at different transformation temperatures was of 20 minutes in all cases. During this thermal exposure, the neutron diffraction spectra were collected in short intervals (30 sec.), while the time-evolution of ferrite $\{110\}_{\alpha}$ and austenite $\{111\}_{\gamma}$ reflection was recorded, respectively. After isothermal transformation at different transformation temperatures all specimens (**A**, **B**, **C**, **D**) were cooled down to the room temperature.

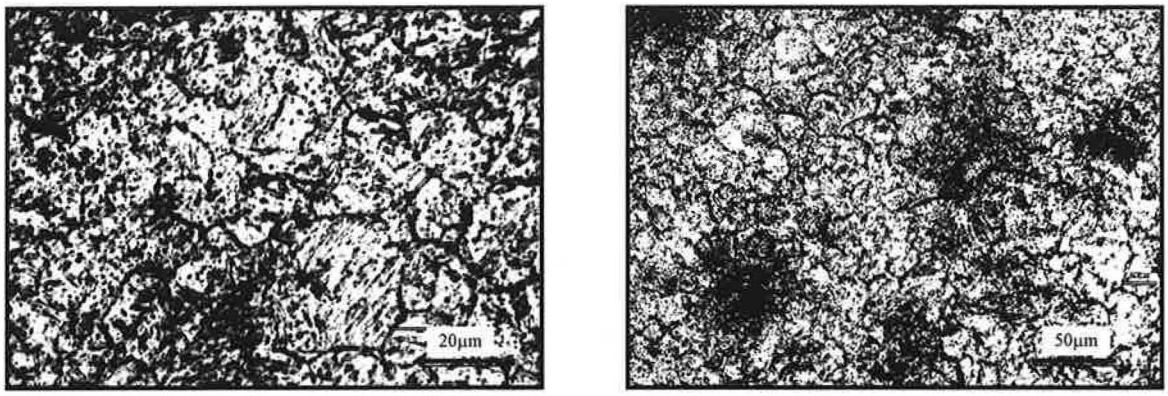

Figure 6.20a,b: Microstructure of soluble austenite after applied solutioning at 1000 °C.

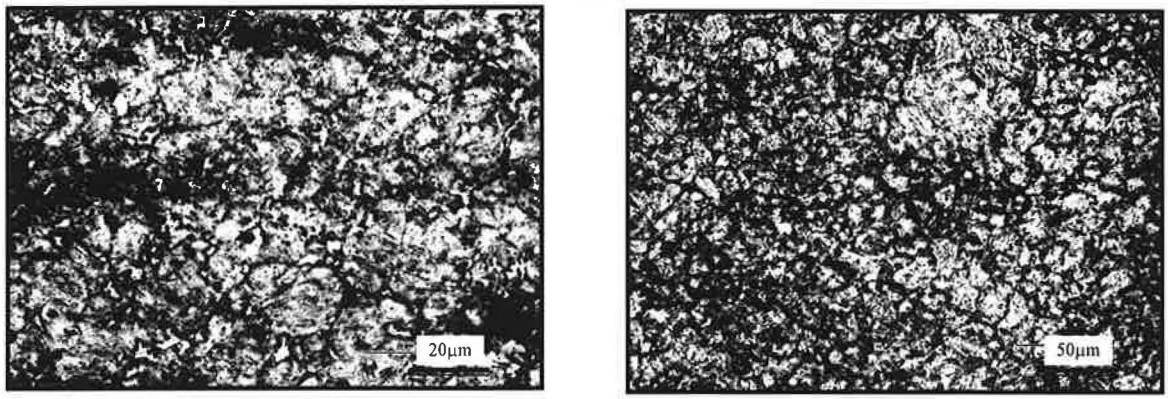

Figure 6.21a,b: Microstructure of conditioned austenite after applied deformation of 25% at temperature of spontaneous recrystallisation.

6.2.3 Microstructure Evolution during Isothermal Transformation

As mentioned above, in this case, thermo-mechanical (TM) processing comprised of solutioning at corresponding temperature of 1000 °C (see micrographs of the experimental steel after solutioning in Fig.6.20a,b) followed by compressive deformation of 25% and isothermal transformation. Micrographs of conditioned austenite obtained by light microscopy, developed as a result of the applied solutioning and compressive deformation are documented in Fig.6.21a,b. It is obvious from the comparison of microstructure of solutionized austenite in Fig.6.20 and conditioned austenite in Fig.6.21 that applied deformation caused austenite grain refining. Consequently, following austenite-to-ferrite phase transformation of the conditioned austenite has been studied by the *in situ* neutron

diffraction at isothermal transformation temperatures of 700, 750, 775 and 800 °C (20 min.) for specimens (**A**, **B**, **C**, **D**), respectively (Fig.6.19).

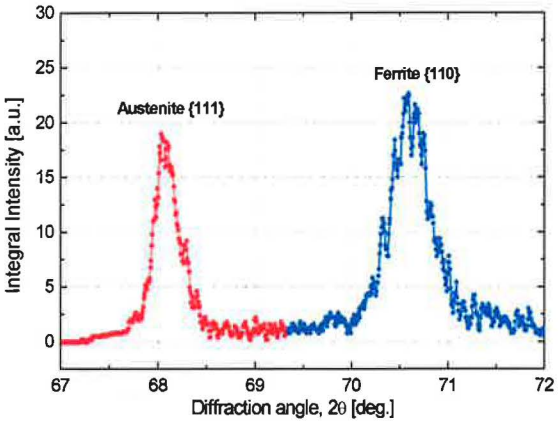

Figure 6.22: Examples of the neutron diffraction profiles of ferrite $\{110\}_\alpha$ (T=20°C) and austenite $\{111\}_\gamma$ (T=750°C), respectively.

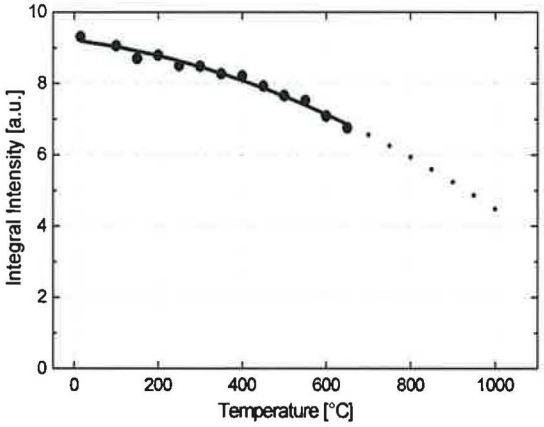

Figure 6.23: Temperature calibration curve of the integral intensity of ferrite $\{110\}_\alpha$ reflection as a function of temperature.

Similarly to the previous *in situ* experiment (see section 6.1) relevant information on the transformation kinetics were extracted from integrated intensities of the individual ferrite $\{110\}_\alpha$ and austenite $\{111\}_\gamma$ reflections recorded in 30 sec. sequences during isothermal exposure (Fig.6.22). The integrated intensity of these diffraction peaks is proportional to the phase volume fraction; however, it also strongly depends on the temperature [72, 108]. To eliminate this temperature effect, the calibration dependence of the $\{110\}_\alpha$ intensity as a function of the temperature was measured in a single-ferrite phase state of the steel. Because the ferrite single-phase state was observed in present steel in lower temperature range up to 650 °C only, the intensity values for higher temperatures have been extrapolated numerically (Fig.6.9b, section 7.1.3.1). The calibration curve in Fig.6.23 yields thus the relevant intensities $I_\alpha^{100}(T_i)$ corresponding to 100% ferrite volume fraction for the transformation temperatures. The ferrite volume fraction was then estimated by means of Eq.6.1 in section 6.1.3 where is this procedure fully described.

The time-evolution of the volume fraction of present phases were determined in the course of isothermal exposure at different transformation temperatures. An example of such a record at transformation temperature of 750 °C is shown in Fig.6.25, whereas temperature record for this particular experiment is documented in Fig.6.24. The time-evolution of the austenite and ferrite phase volume fractions for all studied transformation temperatures in samples **A**, **B**, **C**, **D** are summarized in Fig.6.26 (time-evolution of austenite volume fraction) and in Fig. 6.27 (time-evolution of ferrite volume fraction).

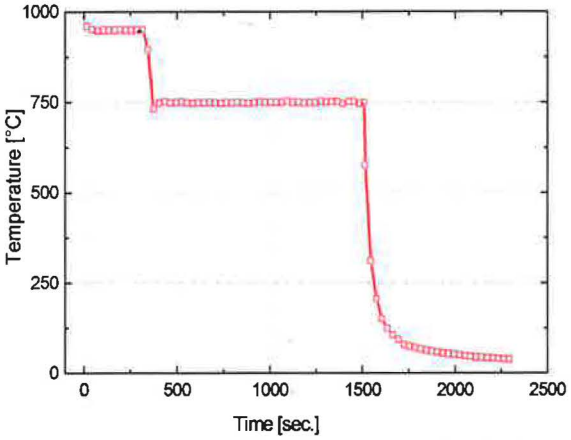

Figure 6.24: Temperature record during isothermal transformation at transformation temperature of 750°C.

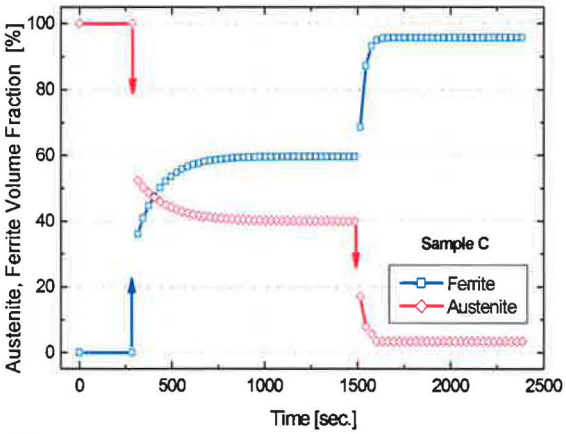

Figure 6.25: Time evolution of the volume fraction of both phases during thermal loading, T_t = 750 °C.

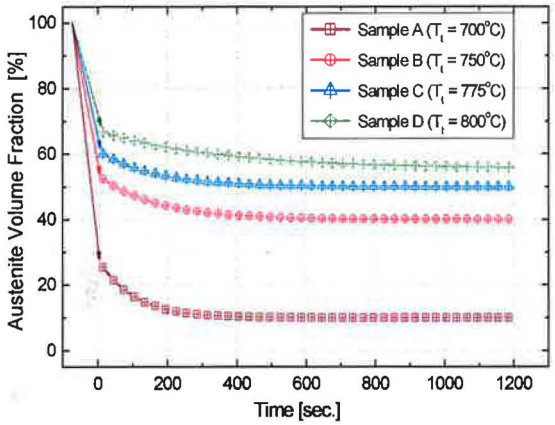

Figure 6.26: The time-evolution of the austenite phase volume fractions during isothermal transformation at different temperatures (T_t).

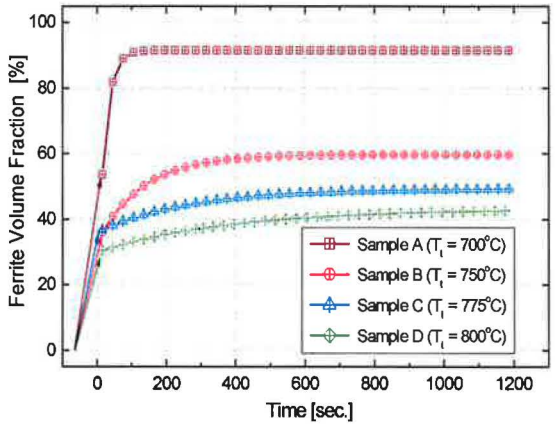

Figure 6.27: The time-evolution of the ferrite phase volume fractions during isothermal transformation at different temperatures (T_t).

From these results the austenite-to-ferrite volume fraction ratio arisen at different transformation temperatures can be easily determined (Tab.6.3). This is the most important criteria for selecting the first transformation temperature in TMCP of low-alloyed TRIP-aided steels, because the following microstructure evolution strongly depends on this austenite-to-ferrite volume fraction ratio (see Fig.2.3). It is mainly because the essential aim of applying TMCP in case of TRIP-aided steels is to obtain retained austenite in the final structure. Therefore, a reasonable amount of the non-transformed austenite has to be present in the steel microstructure after the first isothermal transformation. Concerning sample **A**, the amount of the non-transformed austenite at transformation temperature of 700 °C was too low (Tab.6.3), because if we consider the main purpose of obtaining the significant retained austenite volume fraction (>10%) in the final TRIP steel microstructure the obtained non-transformed austenite volume fraction at this transformation temperature is not optimal. On the other hand, heat treatment of sample **D** (T_t = 800 °C) is not optimum as well, although the content of the non-

transformed austenite is rather high, but high amount of austenite means low carbon saturation and that leads to problems with austenite stabilization at room temperature (section 2.7). On the basis of the acquired results (Fig.6.26, 6.27 and Tab.6.3) the T_t of 750 °C (sample **B**) has been selected as the most suitable transformation temperature at which the optimum volume fraction ratio (39%/62% ± 5%) of austenite-to-ferrite was obtained prior to following bainitic transformations (see Fig.2.3). However, at the T_t of 775 °C (sample **C**) the acceptable volume fractions of present phase constituents have been also achieved, the T_t of 750 °C has been chosen with the view of obtaining the higher volume fraction of the retained austenite in the final microstructure of TRIP-aided steel.

Table 6.3: Austenite and ferrite volume fractions achieved during isothermal transformation.

	T_t	f_γ^{dif} ±5%	f_α^{dif} ±5%
Sample **A**	700 °C	10 %	91%
Sample **B**	750 °C	39 %	62%
Sample **C**	775 °C	51 %	47 %
Sample **D**	800 °C	57 %	41 %

The volume fractions of ferrite and austenite, were determined from independent measurements, therefore their sum was received not exactly 100% in some cases. The statistic error of the measured values is roughly estimated as ±5%. But in general, the results pointing out that amount of phase transformed during isothermal transformation are in good agreement with continuous cooling transformation (CCT) diagram of experimental steel. A small volume fraction of the retained austenite has been found by means of the neutron diffraction in all specimens (ranging from 2.6 to 3.2 %) in their final microstructure after cooling from transformation temperatures.

The neutron diffraction results shown in Fig.6.26, 6.27 revealed that the ferrite and austenite phase volume fractions are stable and remain roughly unchanged after approximately 200 sec. at any chosen transformation temperature. Therefore, in order to evaluate the effect of the isothermal holing time the additional experiment was preformed applying the different holding times t_1 = 200 and t_2 = 400 sec., respectively at the selected transformation temperature of 750 °C (Fig.6.25). The results from these two independent tests imply that after 200 sec. at transformation temperature the ferrite volume fraction does not change. The corresponding ferrite volume fractions in the final microstructure were obtained

the same for both testing holding times as it is also seen from micrographs shown in Fig.6.28 (after t_1 = 200 sec.) and Fig.6.29 (t_2 = 400 sec.).

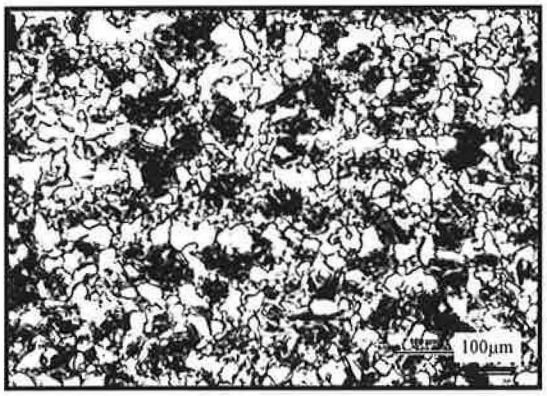

Figure 6.28: Micrograph of ferrite distribution received at transformation temperature of 750 °C and 200 sec. holding time in bulk.

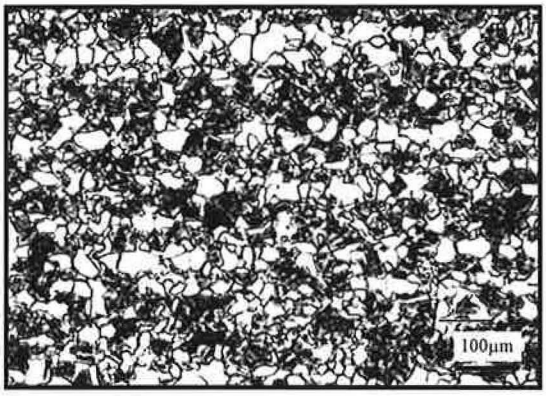

Figure 6.29: Micrograph of ferrite distribution received at transformation temperature of 750 °C and 400 sec. holding time in bulk.

6.2.4 Brief Summary

The *in situ* neutron diffraction technique has been employed for the characterisation of the austenite-to-ferrite phase transformation of the low-alloyed steel at different transformation temperatures (i.e. 700 °C, 750 °C, 775 °C, 800 °C). The temperature of 750 °C (sample **B**) has been chosen as the most convenient austenite-to-ferrite transformation temperature in TMCPs of the TRIP-aided steel after applying the 25% of compressive deformation.

- At the temperature of 750 °C an optimum austenite-to-ferrite volume fraction ratio (~40%/60%) has been achieved.
- This transformation temperature has been also selected with respect to assumed higher carbon content in the non-transformed austenite.
- Moreover, the time necessary for sufficient austenite-to-ferrite phase transformation has been defined.
- Information received from these *in situ* neutron diffraction experiments, and microstructural observation by light microscopy have been used in further experimental procedure to design the deformation, thermal and isothermal time criteria for more advanced thermo-mechanically controlled process (TMCP) of bulk TRIP-aided multiphase steels

7.

DEFORMATION BEHAVIOUR OF TRIP-AIDED STEELS

7.1 NEUTRON DIFFRACTION STUDIES OF TRIP STEELS ON TKSN-400, NPI

The present chapter deals with the deformation and transformation behaviours of variously treated low-alloyed (Si-Mn) TRIP-aided multiphase steels. The motivation for this work is better understanding of the key factors governing deformation and transformation processes in multiphase microstructure of this type of steels. Long discussion has been held whether the sufficient volume fraction of the retained austenite is essential for achieving the enhancement of uniform elongation in TRIP-aided steels or not. It is also anticipated that other microstructural parameters, such as a morphology, particle size, solute enrichment and mechanical stability of the retained austenite can considerably control TRIP effect in low-alloyed TRIP-aided steels and affect thus their mechanical properties in general.

7.1.1 Materials and Experimental Method

Two *in situ* neutron diffraction experiments were preformed on the dedicated diffractometer TKSN-400 at NPI (section 6.1.2.1) in order to study martensitic transformation of retained austenite and stress partitioning between present phases upon a tensile straining. In the first experiment, three TRIP-aided steels samples (**A, B, C**) with different volume fraction of the retained austenite were studied during uniaxial loading. In the second experiment, other three TRIP-aided steel samples (**D, E, F**) containing rather similar volume fraction of the retained austenite (~15%±3%) but with different microstructural characteristics (particle size, morphology, carbon enrichment of retained austenite and ferrite-bainite α-matrix) were prepared and investigated by *in situ* neutron diffraction techniques. In order to obtain the TRIP-aided steels with various microstructural characteristics the different TMCP recently developed also on the basis of previous *in situ* neutron diffraction experiments (see section 6.2) were employed.

7.1.1.1 TMCP of TRIP steels containing various amount of retained austenite

Three specimens (**A, B, C**) of low-alloyed Si-Mn steel (Tab.6.2) in form of bars of 25 mm in diameter were subjected to the different TMCPs (Fig.7.1) in order to obtain fine-grained TRIP-aided steels samples containing significant volume fraction of retained austenite

necessary for occurring the TRIP effect during deformation. Applied thermo-mechanical treatments for these three specimens **A, B, C** were proposed as follows:

- TMCP for Sample **A**: **1)** heating to 1000 °C / 1h (solutioning) → **2)** compression deformation ε_1 = 70% → **3)** air cooling to ~ 840 °C followed by second deformation ε_2 = 60% → **4)** isothermal holding at 750 °C / 300 sec. → **5)** 3 sec. water cooling → **6)** bainite critical tempering at 420 °C / 300 sec. → **7)** air cooling.
- TMCP for Sample **B**: **1)** heating to 1000°C/1h (solutioning) → **2)** compression deformation ε_1 = 70% → **3)** air cooling to ~ 840 °C followed by second deformation ε_2 = 40% → **4)** isothermal holding at 750 °C / 300 sec. → **5)** 3 sec. water cooling → **6)** bainitic critical tempering 420 °C / 300 sec. → **7)** air cooling.
- TMCP for Sample **C**: **1)** heating to 1000°C/1h (solutioning) → **2)** compression deformation ε_1 = 50% → **3)** air cooling to 750 °C **4)** isothermal holding at 750 °C / 180 sec. → **5)** 4 sec. water cooling → **6)** bainitic critical tempering 420 °C / 300 sec. → **7)** air cooling.

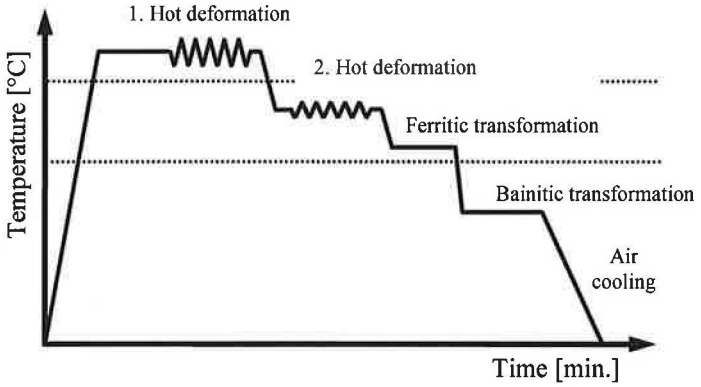

Figure 7.1 An experimental schedule of thermo-mechanically controlled processes (TMCP) for low-alloyed Mn-Si steel.

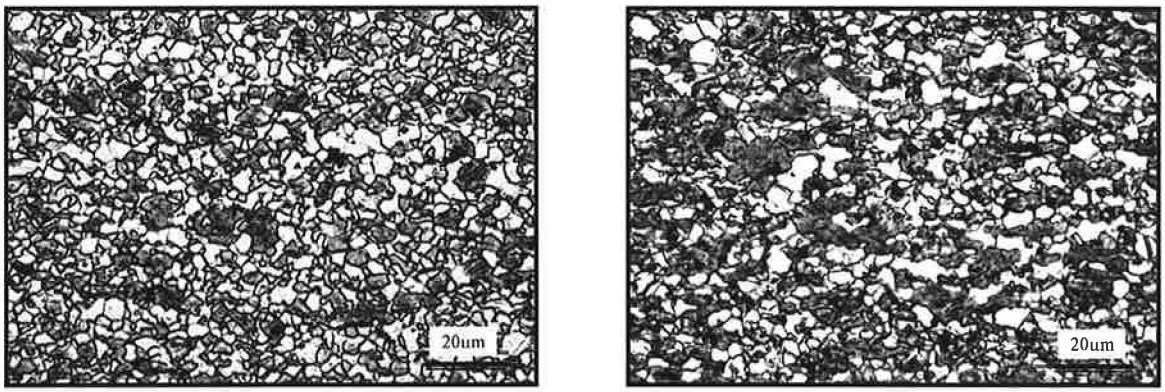

Figure 7.2 a,b: Optical micrographs of prepared TRIP-aided multiphase steels sample **A** (**a**) with retained austenite volume fraction of 15% and sample **B** (**b**) with 21% retained austenite volume fraction.

Microstructure of manufactured TRIP-aided multiphase steels were observed by light microscopy (Fig.7.2) and the retained austenite volume fraction existing in the specimens prior the tensile tests was determined by X-ray and neutron diffraction analysis (Fig.7.4, Fig.7.5). In order to evaluate the influence of the TRIP effect on steel mechanical properties,

the sample **C** after thermo-mechanical treatment but without retained austenite was subjected to tensile test as well.

- Sample **A** ≈ 15%±3% of retained austenite
- Sample **B** ≈ 21%±3% of retained austenite
- Sample **C** ≈ 0%±3% of retained austenite

7.1.1.2 TMCP of TRIP steels with similar retained austenite volume fraction

Three samples (**D, E, F**) of the same low-alloyed Si-Mn steel (Tab.7.1) as in the previous experiment were treated by following three different thermo-mechanically controlled processes:

- TMCP for Sample **D**: **1)** heating to 1000 °C / 30 min. (solutioning) → **2)** compression deformation ε_1 = 50% → **3)** air cooling to ~ 850 °C (non-recrystallisation region) followed by second deformation ε_2 of 65% → **4)** isothermal holding at 750 °C / 300 sec. → **5)** 4 sec. water cooling → **6)** bainite critical tempering at 420 °C / 300 sec. → **7)** air cooling.
- TMCP for Sample **E**: **1)** heating to 1000 °C / 30 min. (solutioning) → **2)** compression deformation ε_1 = 50% → **3)** air cooling to ~ 800 °C (intercritical region) followed by second deformation ε_2 of 65% → **4)** isothermal holding at 750 °C / 300 sec. → **5)** 4 sec. water cooling → **6)** bainite critical tempering at 420 °C / 300 sec. → **7)** air cooling.
- TMCP for Sample **F**: **1)** heating to 850 °C / 30 min. (solutioning) → **2)** air cooling for 10 sec. to ~ 800 °C followed by compressive deformation ε_1 of 65% → **3)** isothermal holding at 750 °C / 300 sec. → **4)** 4 sec. water cooling → **5)** bainite critical tempering at 420 °C / 300 sec. → **6)** air cooling.

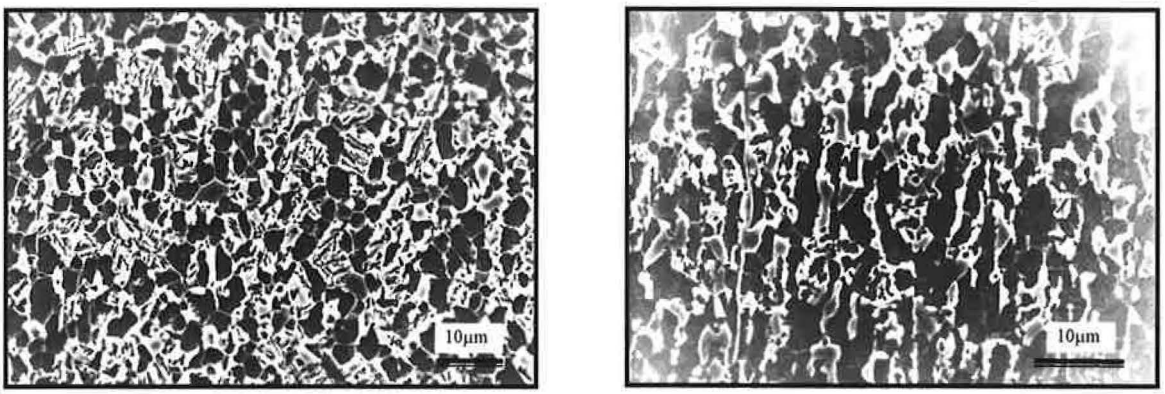

Figure 7.3 a, b: Microstructure of the investigated steel specimens: sample **D** (**a**) with higher bainite volume fraction in the α-matrix and sample **F** (**b**) contains polygonal retained austenite at ferrite grains which transform at lower stresses.

Microstructural characteristics of prepared TRIP-aided steel specimens were analyzed by SEM (Fig.7.3). The retained austenite volume fraction evaluated by X-ray diffraction was of about 10% (±3%) in all three cases (**D, E, F**). Consequently these steel specimens with different microstructures due to different TMCP were subjected to *in situ* tensile test in order

to analyze transformation kinetics of retained austenite to strain-induced martensite (Fig.7.5). As it can be seen from obtained micrographs (Fig.7.3), experimental steel samples (**D**, **F**) differ mainly in grain size, ferrite, bainite volume fraction and bainite morphology. Sample **D** (Fig.7.3a) contains higher amount of bainite with lath morphology while retained austenite is primarily located between these bainitic laths. The major part of the retained austenite in sample **F** containing similar austenite volume fraction as samples **D**, **E,** is present at ferrite grain boundaries (polygonal retained austenite). It has been assumed that polygonal austenite transforms at lower level of stress and thus contributes to the elongation and work-hardening by the second phase hardening [109]. This assumption was consequently confirmed in the performed *in situ* diffraction experiments.

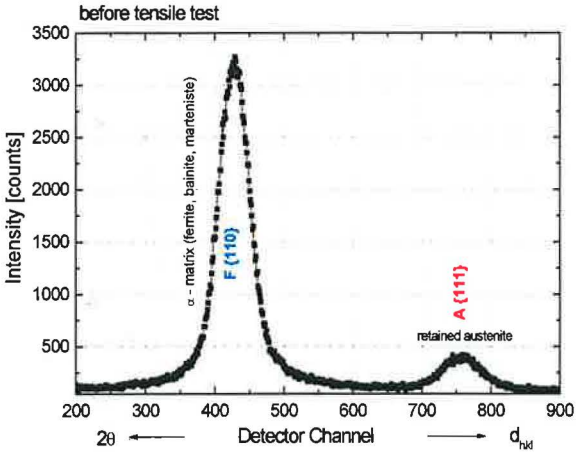

Figure 7.4: Neutron diffraction profiles of ferrite $\{110\}_\alpha$ (2θ ~ 69°) and austenite $\{111\}_\gamma$ (2θ ~ 67°) reflection, respectively, before tensile test.

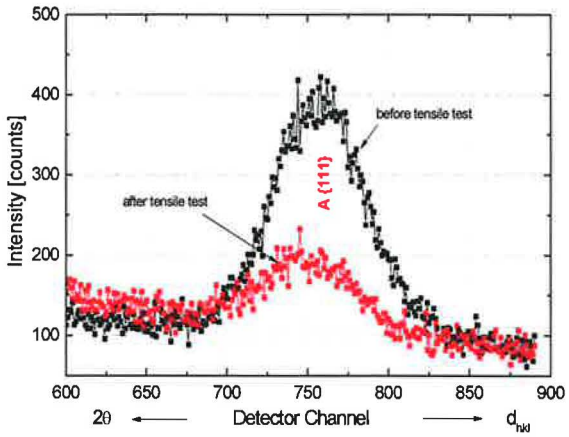

Figure 7.5: Neutron diffraction profile of austenite $\{111\}_\gamma$ reflection before (black) and after tensile test (red, failure of sample **B**).

7.1.1.3 *In situ* neutron diffraction experiments

The *in situ* tensile tests were performed at room temperature on dedicated stress/strain diffractometer, TKSN-400 (section 6.1.4.2, Fig.6.2). The neutron diffraction spectra were collected during temporary stops of the deformation machine at constant stress (stress control). In the first experiment, the tensile rig was in vertical position (exactly as it can be seen in Fig.6.3) in order to record diffraction pattern form grain families oriented perpendicularly to the load direction. In the second experiment the deformation machine was situated horizontally 45° towards the incident beam to obtain diffraction pattern from grains families aligned axially to the load direction. The holding time of one hour in each step was necessary to achieve sufficiently good statistics in measured spectra due to the relatively low neutron flux. The PSD window was set to cover both ferrite $\{110\}_\alpha$ and retained austenite $\{111\}_\gamma$ reflection simultaneously (Fig.7.4, Fig.7.5).

7.1.2 Transformation Kinetics of Retained Austenite during Deformation

7.1.2.1 Effect of retained austenite volume fraction on transformation kinetics

The engineering stress-strain curves of examined **A, B, C** samples are shown in (Fig.7.6). It is clearly seen that both specimens containing retained austenite exhibit larger ability to deform uniformly - necking of the specimen appearing at strains corresponding to the maximum stress is significantly shifted to larger strains. The observed yield stress and strength values of the specimens with the retained austenite surprisingly do not differ much. Specimen **B** containing 21% of retained austenite exhibits the largest elongation in comparison to two others examined samples (Fig.7.6). This can be likely ascribed to the more efficiently retained necking compared to the specimen **A** with 15% of retained austenite.

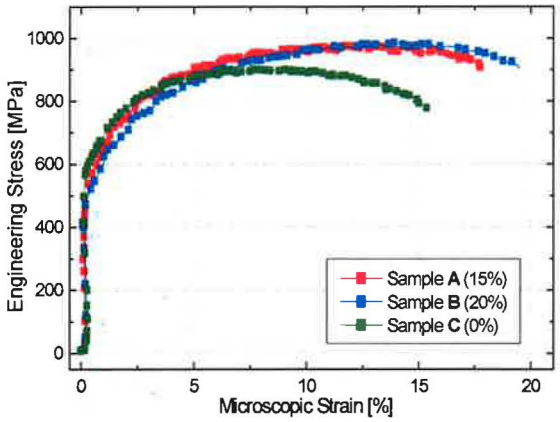

Figure 7.6: Stress-strain curves of the three examined steel specimens (**A, B, C**) containing various volume fraction of the retained austenite in tensile tests at room temperature.

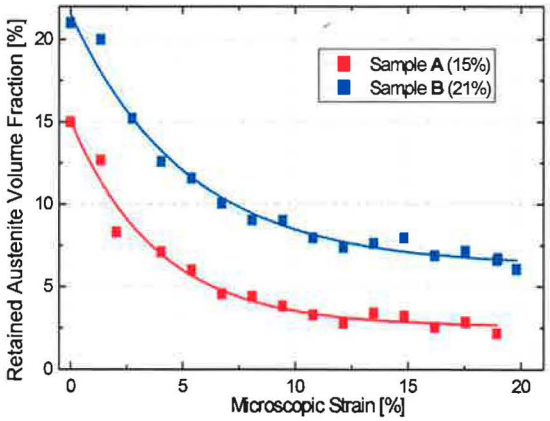

Figure 7.7: Evolution of the austenite volume fraction with ma macroscopic strain during the tensile test estimated from the integral intensity of $\{111\}_\gamma$ austenite reflection.

The strain-induced martensitic transformation of the retained austenite was mainly evaluated from the variation of the integrated intensities of the $\{111\}_\gamma$ austenite reflection during the deformation test (Fig.7.4, Fig.7.5). As it is evident from obtained data (Fig.7.7) taken in radial arrangement, the transformation proceeds massively in early stages of the deformation process at strains $\varepsilon < 0.03$ (sample **B**) and $\varepsilon < 0.1$ (sample **A**). Nevertheless, the transformation behaviour of both specimens shows a rather similar character, the specimen with higher volume fraction of the retained austenite has also higher fraction of the residual non-transformed austenite in the final microstructure after tensile test.

7.1.2.2 Effect of steel microstructure on the retained austenite transformation kinetics

It is obvious from the stress-strain curves (Fig.7.8) that the samples **D, E, F** have different mechanical properties, despite rather similar content of present phase constituents (particularly the retained austenite volume fraction). The sample **D** exhibits the highest yield

stress and elongation whereas the sample **F** has the smallest yield stress but, on the other hand, the highest tensile strength.

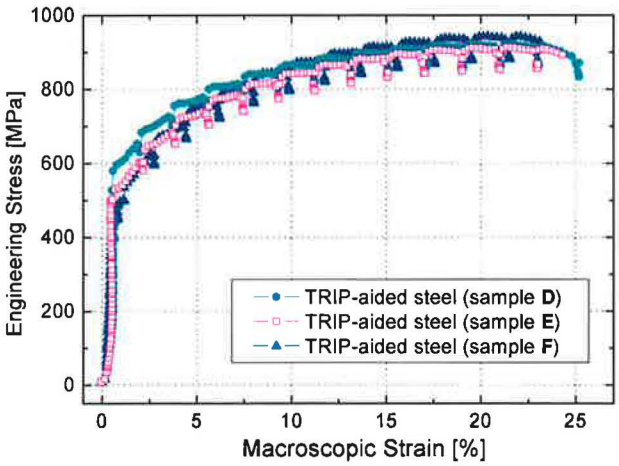

Figure 7.8: Stress-strain curves of the three TRIP steel specimens containing similar volume fraction of the present constituents.

It is well-known that mechanical properties of TRIP-aided multiphase steels strongly depend on the microstructural composition, but in general, it was assumed that the amount of retained austenite has the highest influence on deformation strengthening and uniform plasticity. In our case, however, the retained austenite volume fraction in the structure is roughly similar there are some differences in mechanical properties mainly in yield stress and elongation, as it is seen in Fig.7.8. Therefore, other microstructural influences which can significantly affect the behaviour of TRIP-aided steel during the deformation process have to be considered. Microstructural parameters such as a morphology, grain size, carbon enrichment of retained austenite and composition of α-matrix play important role in deformation process and influence thus achieved mechanical properties of this type of multiphase steels (Fig.7.8) [110,111].

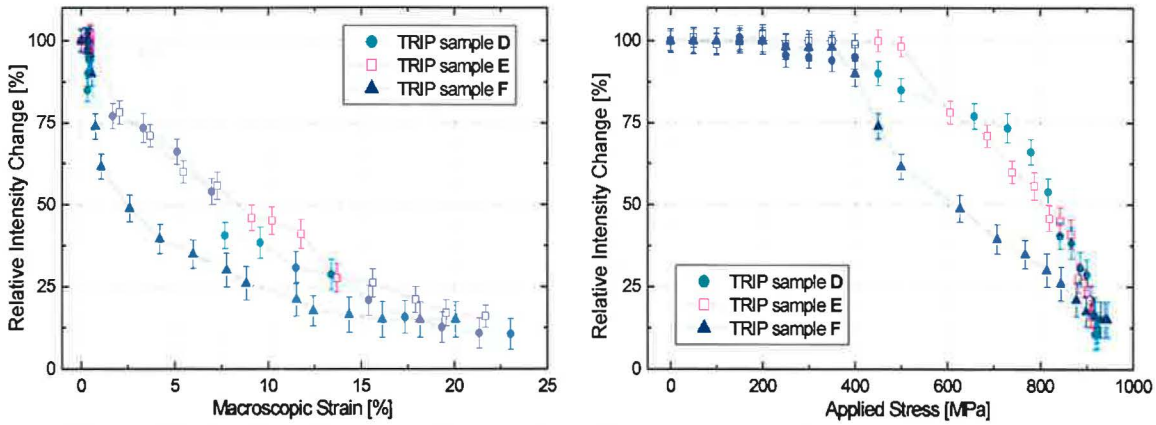

Figure 7.9a,b: Transformation kinetics of retained austenite estimated from austenite $\{111\}_\gamma$ reflection (**a**) as a function of macroscopic stain and (**b**) as a function of the applied stress.

A decrease in the integrated intensity of the austenite $\{111\}_\gamma$ reflections measured individually in the course of tensile testing of TRIP-aided steel specimens (**D**, **E**, **F**) is shown in Fig.7.9. Since the changes in the integrated intensity of the austenite $\{111\}_\gamma$ reflection during the tensile test reflect the changes in the retained austenite volume fraction this method can be used as the first approximation to characterize the kinetics of the austenite transformation during the straining [111,112]. As evidenced from obtained data (Fig.7.9) taken in the axial arrangement, the transformation proceeds most massively in the sample **F** at strains $\varepsilon \geq 0.005$–0.01 (~ 400 MPa). At strain $\varepsilon \geq 0.12$ (~ 890 MPa), almost all present retained austenite in this steel sample is already transformed to the strain-induced martensite. The martensitic transformation in other two samples **D**, **E** starts at higher levels of strain/stress that is related to higher level of yield strengths of the present phase constituents in these samples. In the sample **D** which exhibits the highest elongation, austenite transforms even at the highest strains of $\varepsilon \geq 0.18$. In fact, some untransformed stabilized austenite remains in the microstructure in all TRIP-aided steel specimens even at the end of the tensile test (sample failure). It is assumed that the untransformed retained austenite is present in the microstructure in the form of laths inside the bainite islands [113]. Because of that, it is highly saturated by carbon, which has by far the biggest influence on the retained austenite stability.

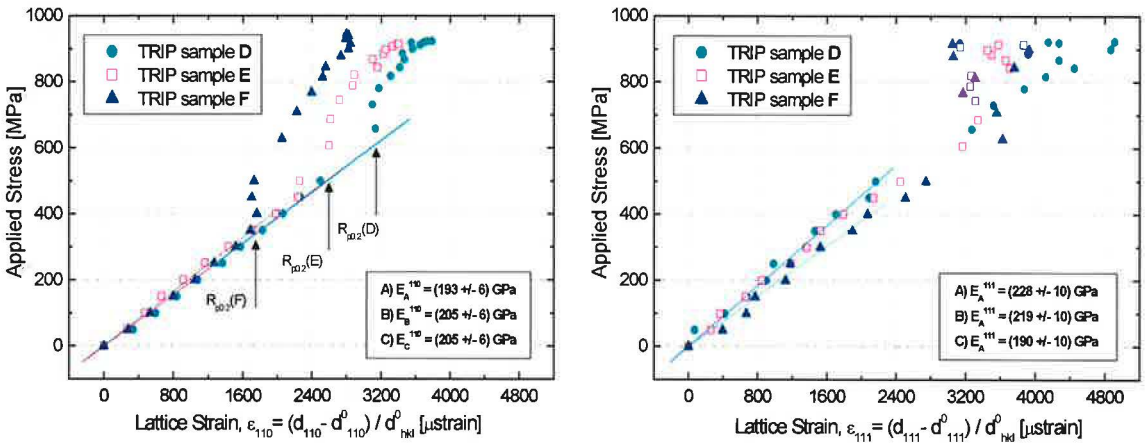

Figure 7.10a,b: Change in lattice plane strain with tensile straining (**a**) of ferrite and (**b**) of austenite, the statistical fit uncertainties are of about 15 microstrain for ferrite and 100 to 200 microstrain for retained austenite.

Figure Fig.7.10a documents the macroscopic (applied) stress vs. lattice strain curves for the $\{110\}_\alpha$ plane in all three samples. At the beginning, all curves show a linear evolution of the lattice strains with increasing of the macroscopic stress. Slightly different slopes (diffraction moduli of ferrite $\{110\}_\alpha$ reflection) in the elastic region of each sample can correspond to the difference in mechanical properties, texture and stress partition between present phases in the microstructure of samples treated by various thermo-mechanical (TM)

processing. The non-linearities occur at the strains/stresses at which the yield point of the $\{110\}_\alpha$ ferrite family grains is reached [114]. As the ferrite-bainite α-matrix constitutes a major part of the microstructure of TRIP-aided steels, it allows us to estimate its yield strength on the basis of the measurement of applied stress vs. lattice strain at plane $\{110\}_\alpha$ just from the axial lattice response. The yield stresses for α-matrix in the TRIP-aided steel samples **D, E, F** received by various thermo-mechanical treatments were determined as: $\mathbf{R_{p0.2}}$ **(A)** ~ 604 MPa, $\mathbf{R_{p0.2}}$ **(B)** ~ 532 MPa, $\mathbf{R_{p0.2}}$ **(C)** ~ 361 MPa. These obtained α-matrix yield strengths coincide very well with macroscopic yield strengths determined from stress-strain curves (see Fig.7.8). It is assumed that the hardness of the α-matrix increases with the volume fraction of bainite, which is known as harder phase than ferrite.

The figure Fig.7.10b documents the austenite $\langle 111\rangle_\gamma$ oriented grain family elastic strain with respect to the applied stress (lattice strain vs. applied load). From the comparison of the lattice strain response of ferrite $\langle 110\rangle_\alpha$ and austenite $\langle 111\rangle_\gamma$ oriented grains it is clearly seen that in all tested samples (**D, E, F**) the ferrite $\{110\}_\alpha$ family grains yields earlier than austenite $\{111\}_\gamma$ family grains. Furthermore, it is obvious that at yielding point of ferrite-bainite α-matrix load is transferred towards the austenite $\langle 111\rangle_\gamma$ grains and accelerates thus the martensitic transformation of such oriented austenitic grains. Obtained results imply that retained austenite is stiffer phase than ferrite-bainite α-matrix in TRIP-aided multiphase steel which is in contrast to the usual concept of austenite as a more compliant phase. This assumption has been confirmed also in the following experiment on ENGIN-X at ISIS.

7.1.3 Brief Summary

In the first experiment, a significant improvement in strength and elongation was achieved in the case of the TRIP-aided multiphase steel specimens (**A, B**) in comparison to the retained austenite-free steel (Fig.7.6). On the other hand, no essential difference in the tensile behaviour was found between the TRIP-aided steel specimens **A, B** containing different volume fraction of the retained austenite (15%; 21%). This effect is probably caused by different types of the retained austenite present in differently treated TRIP-aided steel specimens as well as by slightly different composition of the ferrite-bainite α-matrix. This assumption is supported by different retained austenite transformation kinetics in both steels (Fig.7.7). Furthermore, a significant amount of the retained austenite has been retained in microstructure even after failure in both tested steel samples (**A, B**) containing retained austenite.

Results obtained in the second experiment show that the elasto-plastic properties of the individual phases present in TRIP-aided multiphase steels (ferrite, bainite, retained austenite and/or martensite) are markedly affected by the choice of TCMP parameters (deformations, transformation temperatures, etc.). Not only volume fraction of the retained austenite but also its microstructural state (size, distribution, carbon saturation, morphology) and the state of surrounding ferrite-bainite α-matrix can influence the mechanical properties of the TRIP-aided steel. That gives us an opportunity to prepare TRIP steels with tailored mechanical properties for various engineering applications.

7.2 NEUTRON DIFFRACTION STUDIES OF TRIP STEELS ON ENGIN-X, ISIS

In order to obtain complex information on strain-induced martensitic transformation and load partitioning in the TRIP-aided multiphase steels full diffraction patterns were observed during uniaxial loading tests on ENGIN-X at ISIS spallation neutron source. These *in situ* experiments brought a lot of important information on the transformation kinetics of the retained austenite and evolution of the interphase and intergranular strains during the tensile straining.

7.2.1 TMCP of Experimental Material and Microstructure Characterisation

The low-alloyed Si-Mn steel samples (Tab.7.1) in the form of bars of 25 mm in diameter were subjected to two slightly different thermo-mechanical controlled processes (TMCP) [114] (Fig.7.1) resulting in two TRIP-aided steel samples **G, H** with different microstructures. The TMCP parameters (transformation temperatures, deformation, etc.) of the relevant thermo-mechanical processes for prepared steel samples (**G, H**) are as follows:

- TMCP for Sample **G**: **1)** heating to 850 °C / 30 min. → **2)** compression deformation ε_1 = 50% → **3)** air cooling to 750 °C → **4)** isothermal holding at 750 °C / 600 sec. → **5)** water cooling in 4 sec. → **6)** bainitic critical tempering at 420 °C / 600 sec. → **7)** air cooling.
- TMCP for Sample **H**: **1)** heating to 1000 °C / 30 min. → **2)** compression deformation ε_1 = 50% → **3)** air cooling to ~ 820 °C followed by second compressive deformation ε_2 of 60% → **4)** air cooling to 750 °C followed by isothermal holding for 300 sec. → **5)** water cooling in 4 sec. → **6)** bainitic critical tempering at 420 °C / 300 sec. → **7)** air cooling.

Microstructural Characterisation

Microstructural SEM analysis of both tested samples revealed that resultant multiphase TRIP-aided steel structure consists of polygonal ferrite, bainite (α-matrix) and retained austenite. The SEM micrographs corresponding to samples **G** and **H** are shown in Fig.7.11

and Fig.7.12 respectively. Apparently the main difference between the structures is the size and ferrite volume fraction on one side and bainite morphology on the other side. The retained austenite volume fraction, measured using X-ray and neutron diffraction, was detected to be higher in sample **G** (8%±3%) and lower in sample **H** (4%±3%). Due to a higher solutioning temperature (1000°C) for sample **H,** the ferrite and bainite are coarser, and as it is seen in Fig.7.12 a large amount of bainite with lath morphology is observed. In the case that the TMCP is started at lower solutioning temperature (800°C, sample **G**) the obtained structure is significantly finer and consists of equiaxed ferrite and granular bainite (Fig.7.11). The retained austenite in sample **G** is very fine-grained (1-2 μm) and precipitated either on ferrite boundaries or in the area of granular bainite. The size of retained austenite precipitated in sample **H** on ferrite grain boundaries (blue arrows in Fig.7.12) is of similar size to that in sample **G**. However, in the case of specimen **H**, some retained austenite is also found as laths within bainite islands (red arrows in Fig.7.12).

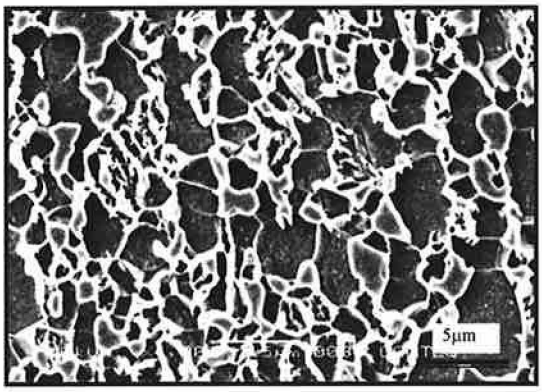

Figure 7.11: Microstructure of the prepared TRIP-aided multiphase steel, sample **G** with retained austenite volume fraction of 0.08.

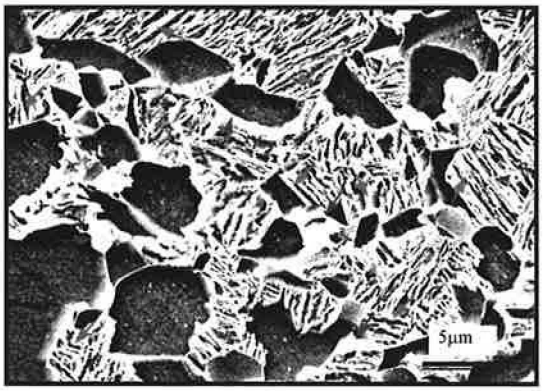

Figure 7.12: Microstructure of the prepared TRIP-aided multiphase steel, sample **H** with retained austenite volume fraction of 0.04.

7.2.2 Uniaxial Loading Test on ENGIN-X

In situ diffraction experiments during uniaxial tensile deformation were carried out at room temperature using ENGIN-X diffractometer (Fig.7.13). The diffraction experiment is conducted in time-of-flight (TOF) mode using neutron pulses with a range of energies travelling a distance towards the sample and detectors, so that their time-of-flight is proportional to the wavelength and elastic scattering in the sample [115,116]. The instrument is equipped by Instron testing machine (Fig.7.14) mounted on the diffractometer, with its loading axis 45° turned to the incident beam. There are two detector banks (Fig.7.13) which measure time-resolved diffraction patterns at fixed horizontal scattering angles of ± 90° [116]. Each *hkl* reflection in the diffraction pattern (Fig.7.18) is generated by distinct family of

polycrystal grains equally oriented with respect to the load axis. The two detector banks thus measure diffraction patterns from grains oriented in axial and radial geometry with respect to the applied tensile stress.

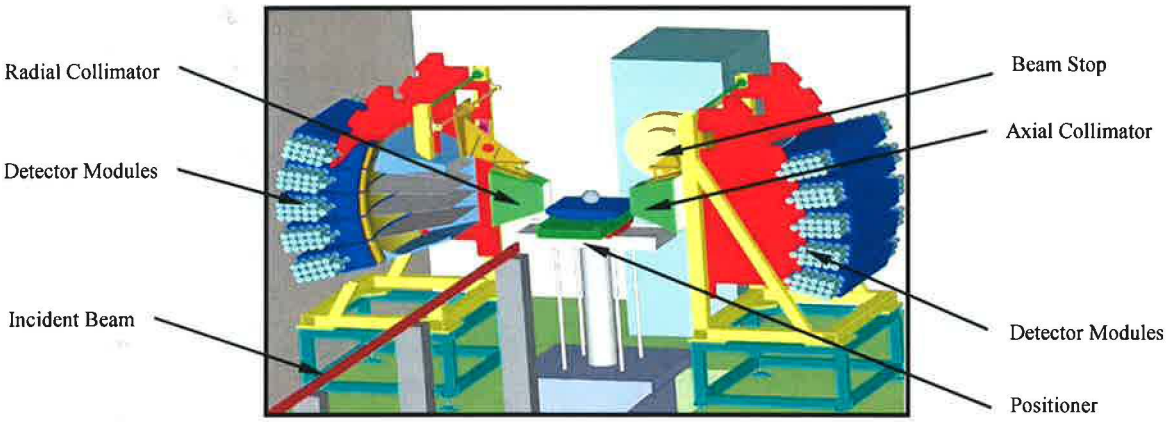

Figure 7.13: A CAD (Computer-Aided Design) image of the ENGIN-X instrument at ISIS, showing the two detector banks at 90° scattering angle, the radial collimators and the x-y-x-Q sample positioner [72].

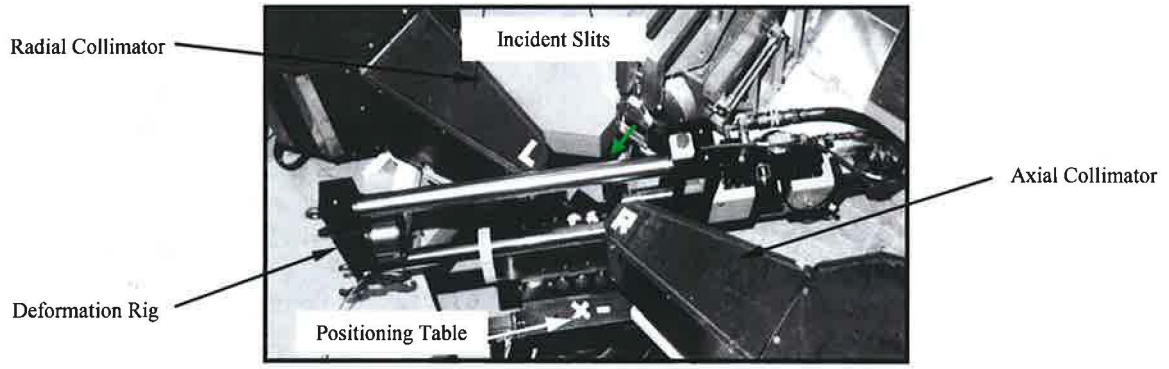

Figure 7.14: Photograph of the stress rig in the place on the stress/strain diffractometer ENGIN-X at ISIS spallation source.

The *in situ* diffraction experiments during tensile tests were conducted using combined stress and strain control, with count times of 10 minutes approximately (measured on neutron counts). The stress control was used during diffraction data acquisition at low strains ($\varepsilon \leq$ 2%), while strain control mode was used in later stages. Macroscopic strain was monitored by means of a clip gauge extensometer fitted directly on the sample surface.

7.2.3 Macroscopic Response

The macroscopic stress-strain curves measured in tensile tests on samples **G**, **H** are shown in Figs.7.15,16 (Fig.7.16 is an enlarged part of the curves near the yield point, as run in the stress controlled regime). The short plateaus of the step-wise curves in Fig.7.16 ($\varepsilon \leq$ 2%) correspond to the creep deformation during temporary dwells in the stress controlled part of

the tests, during which the diffraction data were collected. On the other hand, stress relaxations of about 100 MPa (see inset in Fig.7.15) take place during the temporary dwells in the strain controlled part of the tensile test ($\varepsilon > 2\%$). The mechanical properties of Young's modulus (**E**), yield stress ($\mathbf{R_{p0.2}}$), tensile strength ($\mathbf{R_m}$) and elongation (**A**) determined from the tests are summarized in Tab.7.2. Sample **H** clearly exhibits a higher yield stress ($\mathbf{R_{p0.2}}$ = 600MPa) than sample **G** ($\mathbf{R_{p0.2}}$ = 500MPa) but substantially lower elongation, whereas tensile strengths of both samples are comparable. The higher yield stress of sample **H** can be most likely attributed to the higher bainite volume fraction in the α-matrix (Fig.7.12) within its microstructure.

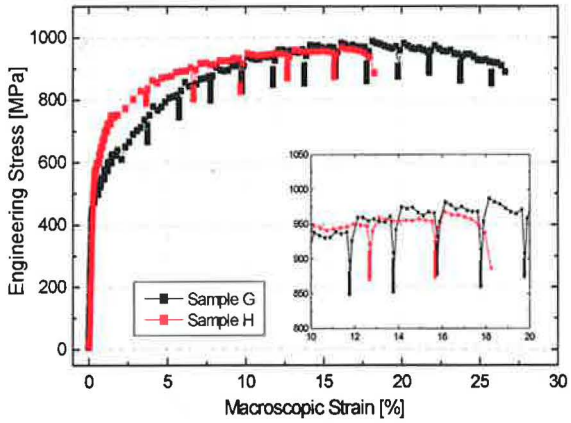

Figure 7.15: The macroscopic tensile stress-strain curves of two different TRIP-aided steels (samples **G,H**) at room temperature. The inset shows stress relaxations during temporary stops (strain control mode $\varepsilon > 2\%$) required for the collection of neutron diffraction data.

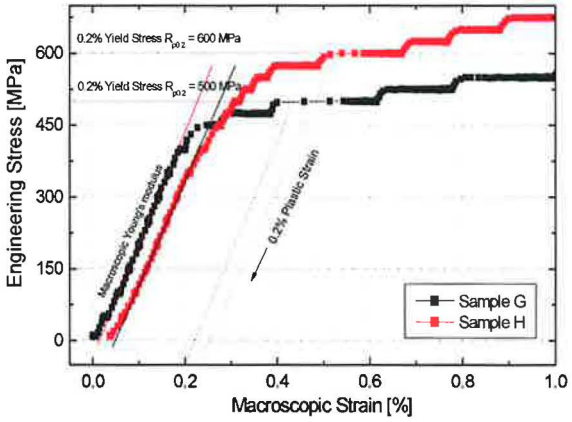

Figure 7.16: Early stage of the tests (stress control mode $\varepsilon \leq 2\%$), with graphical representation of the Young's modulus, 0.2% yield stress and 0.2% plastic strain.

Table 7.2: Mechanical properties of both tested TRIP-aided steel samples (**G**, **H**)

	E [GPa]	$\mathbf{R_{p0.2}}$ [MPa]	$\mathbf{R_m}$ [MPa]	**A** [%]
Sample **G**	230	500	992	26.6
Sample **H**	200	600	983	18.2

7.2.4 Full Diffraction Pattern Analysis

Dummy Histogram (GSAS – prediction)

The GSAS (General Structure Analysis System) package was used to simulate the diffraction pattern of modelled TRIP-aided steel consisting of single ferritic matrix (80%) and retained austenite (20%). Time-of-flight (TOF) neutron diffraction pattern of this simulated un-textured TRIP-aided steel prior the tensile test is in Fig.7.17a. The used lattice parameters

of ferrite (*b.c.c.*) and austenite (*f.c.c.*) lattices were obtained from already reported data [72] as 0.2846 nm and 0.3589 nm for ferrite and austenite, respectively.

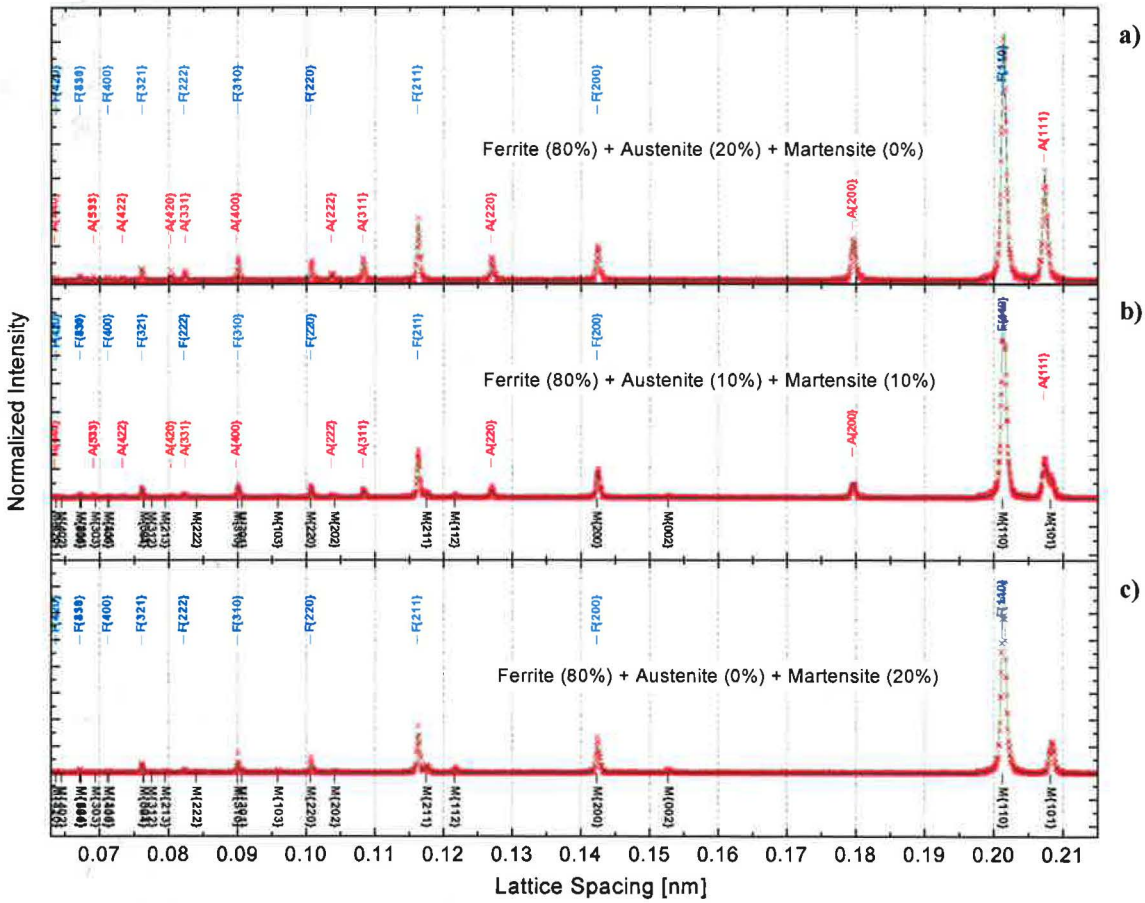

Figure 7.17: GSAS predictions of full diffraction pattern of TRIP-aided multiphase steels consist of (**a**) 80% ferrite + 20 % austenite, (**b**) 80% ferrite + 10% austenite + 10% martensite, (**c**) 80% ferrite + 20% martensite.

During the straining the external strain reaches critical value for starting the strain-induced transformation of the retained austenite (*f.c.c.*) into the martensite (*b.c.t.*). Therefore, the microstructure of the TRIP steel will consist of the ferrite matrix, retained austenite and strain-induced martensite. For example, the full diffraction pattern of TRIP-aided steel in the course of the straining with 10% of newly formed martensite phase is shown in Fig.7.17b. In this example, the body-centered tetragonal (*b.c.t.*) martensite containing 0.14% C with the lattice constant ratio c/a = 1.07 (a = 0.2846 nm, c = 0.3053 nm) was introduced into the structure model (Fig.7.17b,c). However, martensite forming in the deformation process as a result of the strain-induced martensitic transformation of the face-centred cubic retained austenite does not have to be strictly body-centred tetragonal. Nevertheless this simulation can give us a scheme how the full diffraction pattern of TRIP steel will be affected by the presence of martensitic reflections. Unfortunately, it can be seen from modelled histograms (Fig.7.17b,c) that most of the martensite reflections are overlapped by ferrite and austenite

peaks, however, there are still some single martensitic peaks as $\{202\}_{\alpha'}$, $\{112\}_{\alpha'}$, $\{103\}_{\alpha'}$ and $\{222\}_{\alpha'}$. But positions of these single martensite peaks depend on the martensite tetragonality, the lattice constants ratio c/a. If one compares the simulated diffraction pattern (Fig.7.17) with partial diffraction pattern obtained at high-resolution diffractometer at NPI (Fig.7.4) and full diffraction pattern from ENGIN-X (Fig.7.18), the martensite lattice parameters can be roughly deduced. It can be observed that in GSAS modelled patterns, the martensitic reflections $\{110\}_{\alpha'}$, $\{101\}_{\alpha'}$ and $\{112\}_{\alpha'}$, $\{211\}_{\alpha'}$ are clearly separated, whereas in obtained diffraction patterns are overlapped (Fig.7.18). This is due to the fact that lattice constant ratio c/a is actually much smaller than it was assumed in the modelled body-centred tetragonal martensitic lattice (Fig.7.17b,c). Therefore, we observe martensitic peaks just as the overlapping shoulders (wings) at some ferritic reflections as for example at $\{110\}_{\alpha}$, $\{211\}_{\alpha}$ and $\{220\}_{\alpha}$ (arrows, Fig.7.18).

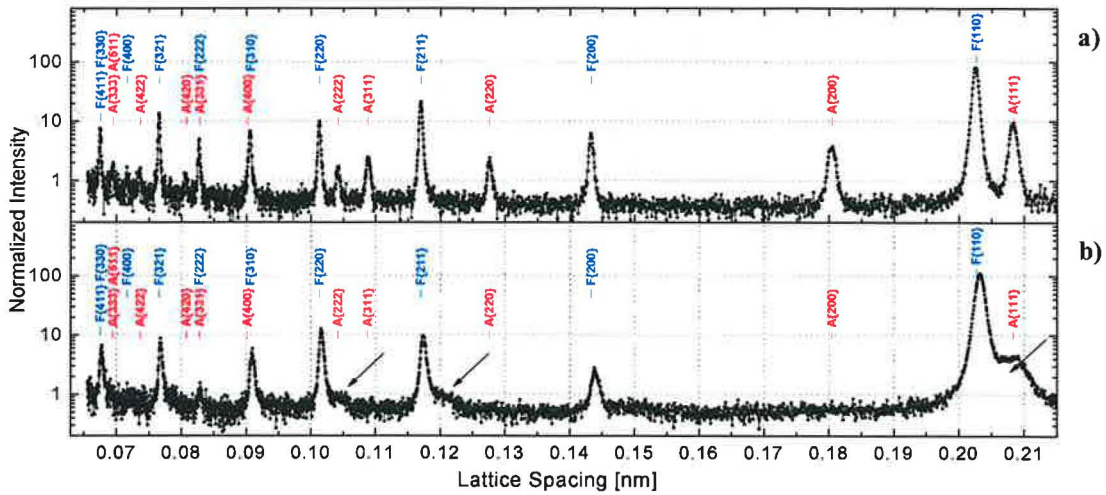

Figure 7.18: Axial full diffraction pattern of TRIP-aided multiphase steel (**a**) before and (**b**) "after" tensile test (Sample **G**).

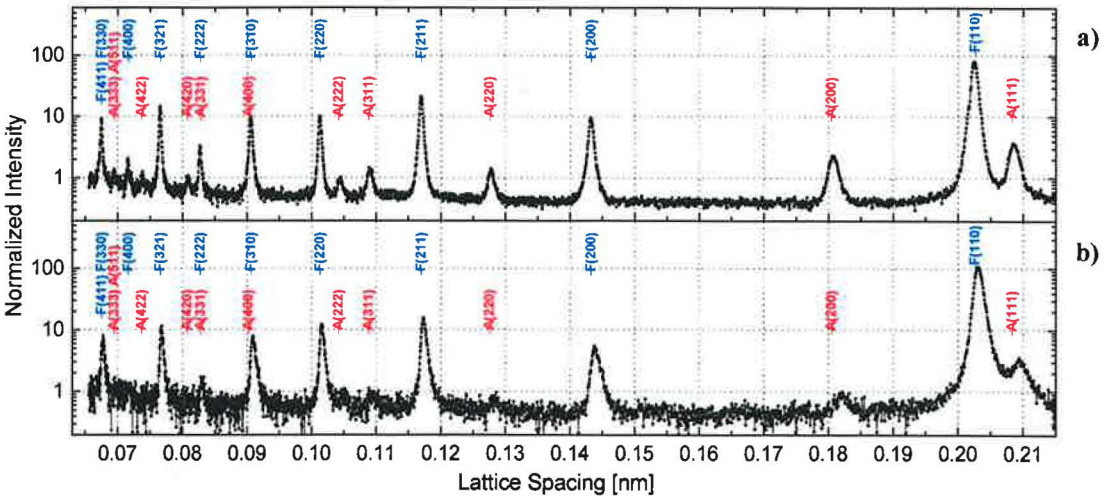

Figure 7.19: Axial full diffraction pattern of TRIP-aided multiphase steel (**a**) before and (**b**) "after" tensile test (Sample **H**).

Analysis of Measured Diffraction Patterns

Axial diffraction spectra before and "after" (last diffraction pattern before the sample failure) tensile testing are shown in Fig.7.18 for sample **G** and in Fig.7.19 for sample **H**. Ferrite-bainite (α-matrix) and austenite diffraction reflections are labelled as F{hkl} and A{hkl}, respectively. Austenite diffraction peaks weaken and become more diffuse as the plastic strain is increased (see error bars in Fig.7.25) and, finally, it is nearly impossible to determine their position. Stress-induced martensite reflections are completely overlapped in most cases with those from ferrite-bainite α-matrix. Individual martensitic peaks are not distinguished, however, GSAS-prediction with ideal martensite as body-centred tetragonal shows some individual martensitic peaks (Fig.7.17b,c). But some martensitic reflections were observed as the overlapped shoulders of some ferrite-bainite reflections (e.g. $\{200\}_{\alpha}$, $\{211\}_{\alpha}$ and $\{110\}_{\alpha}$) in sample **G** (see arrows in Fig.7.18). Observed shoulders at $\{220\}_{\alpha}$ and $\{110\}_{\alpha}$ ferrite-bainite peaks are probably mixed reflections of the non-transformed austenite and the newly formed martensite in the deformation process. Therefore, the strongest austenitic reflection $\{111\}_{\gamma}$ had to be excluded from data analysis, after becoming overlapped by ferrite $\{110\}_{\alpha}$ and martensite $\{101\}_{\alpha'}$, $\{110\}_{\alpha'}$ reflections (Fig.7.18).

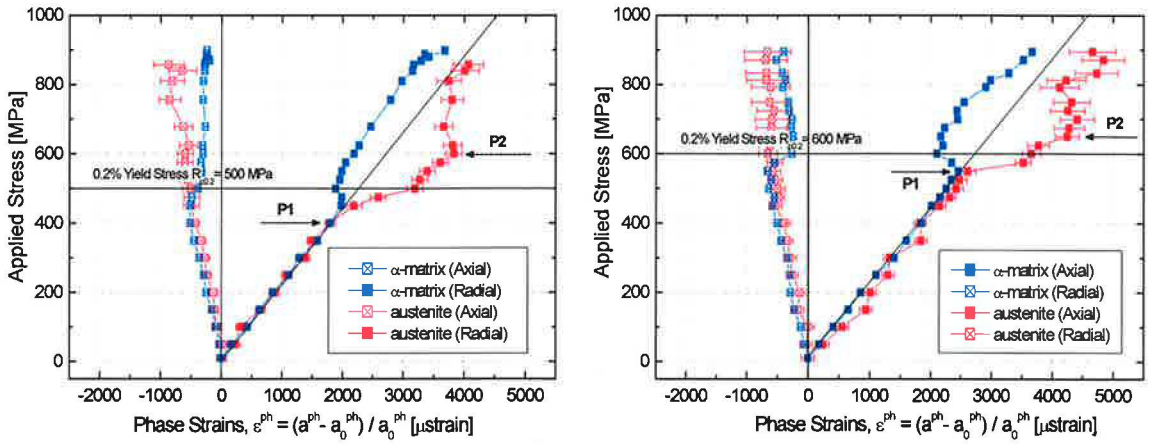

Figure 7.20a,b: Evolution of the volume-averaged phase strains ε^{ph} (in both axial and radial geometries) in the α-matrix and retained austenite with the applied stress during tensile deformation of two TRIP-aided steels sample **G (a)** and sample **H (b)** measured by the neutron diffraction. The uncertainties in the determination of phase strains in the retained austenite are from 50 to 250 microstrain, depending on the peak intensity and count times, while the uncertainties on the α-matrix strains are from 15 to 25 microstrain.

7.2.5 Load Partitioning between Retained Austenite and Ferrite-Bainite Matrix

The evolutions of the volume-averaged phase strains, ε^{ph}, of the ferrite-bainite α-matrix and retained austenite during tensile tests on both of the investigated TRIP-aided multiphase steels (samples **G**, **H**) are plotted in Figs.20a,b as functions of the applied stress. The stress

free lattice parameters, a_0^{ph}, were taken as those measured in the α-matrix and retained austenite prior to the uniaxial loading test, so that any potential initial residual strains/stresses were neglected. When studying tensile deformation of common single phase materials by *in situ* diffraction, the evolution of the volume-averaged phase strain ε^{ph} remains approximately linear with the applied stress even after the onset of plastic flow (Fig.5.1). This is due to the fact that the role of elastic and plastic anisotropies in the deformation process between reflecting grains in the single phase material is eliminated by volume-averaging [117]. In contrast, the onset of plastic deformation of a multiphase material with different elasto-plastic properties of individual phases is accompanied by significant redistribution of stresses between the phases. The interphase stresses are evidenced by significant deviations of the lattice strain-stress dependencies from linearity [72,117].

As seen in Figs.20a,b the volume-averaged phase strains ε^{ph} determined in the α-matrix and retained austenite at applied stresses below the elastic limit (labelled as **P1**) are similar and are proportional to the macroscopic applied stress. This suggests that the elastic properties of the α-matrix and retained austenite are comparable. Above the elastic limit, however, the phase strains of α-matrix and retained austenite deviate from linearity in opposite directions. This is due to the redistribution of stress from the α-matrix (which starts to yield plastically at lower stress) towards the retained austenite. This implies that the stress needed to transform the retained austenite into martensite is higher than that needed to trigger plastic deformation in the α-matrix. The tensile stress in the austenite increases with increasing applied stress up to the point where it starts to deform plastically and/or transform to the martensite phase. Macroscopic yielding of the sample may only start after the load has been redistributed and stress in the retained austenite has reached the transformation limit. In what follows, inelastic deformation processes proceed in both α-matrix and retained austenite in a hardening manner which leads to further increase of the stresses (phase strains) in both microstructure components. The retained austenite thus provides the potential for high ductility of the TRIP-aided steel but at the same time acts as a "*reinforcement phase*" during the plastic deformation of its complex multiphase microstructure. Beyond the macroscopic yielding point, when austenite volume fraction quickly decreases as a result of the strain-induced transformation, the data analysis becomes complicated by the fact that the reflections of the newly formed martensitic phase overlap with the ferrite-bainite reflections (Fig.7.17). In the last stages of the test, when significant martensite volume fraction is present, the stress is probably

redistributed again from the austenite towards the new much harder martensite phase, which we refer to as "*austenite load shedding*" (point **P2**, Fig.20a,b). The interpretation is however, not easy since the hardening behaviour is not known, and the retained austenite in the alloy microstructure may exist in various morphological forms and have different carbon contents. Similar qualitative conclusions on austenite phase being the harder phase in TRIP steel microstructure were drawn by Furnémont [118] and Tomota [109].

In the following an estimation of the load partitioning between retained austenite and α-matrix is calculated. Neglecting any initial residual phase stresses, the volume-averaged phase stresses σ_{11}^{ph} in the α-matrix and retained austenite can be estimated by Hooke's law as follows:

$$\sigma_{11}^{ph} = \frac{E^{ph}}{(1+\nu^{ph})(1-2\nu^{ph})}\left[(1-\nu^{ph})\varepsilon_{11}^{ph} + \nu^{ph}(\varepsilon_{22}^{ph} + \varepsilon_{33}^{ph})\right] \qquad (7.1)$$

In order to determine quantitatively the stress redistribution between phases, the average phase stresses in the α-matrix and retained austenite were calculated at macroscopic yielding point of both tested steels using material parameters in Tab.7.2 and phase-specific elastic constants estimated from the diffraction results in Fig.20a,b (slopes of the ε^{ph}- stress dependencies - we note that strictly the constraint imposed by one phase on another modifies these estimates from true constraint-free elastic constants, but in practice the similarity in elastic properties between phases makes this additional constraint very small). As regards sample **G**, the Young modulus of the α-matrix (E^{α}) and retained austenite (E^{γ}) were obtained almost identical as 218 GPa and 217 GPa, respectively. These values are close to the results reported in the literature for single ferritic steel (220 GPa), whereas the Young modulus of single phase austenitic steel is reported to be about 200 GPa [72,109]. This difference is probably caused by the already mentioned constraint imposed by one phase on another or/and by the high carbon concentration in retained austenite, which considerably affects its elastic properties. Poisson's ratios, ν^{γ} (retained austenite) and ν^{α} (α-matrix) were determined as $\nu^{\gamma} = 0.26$ and $\nu^{\alpha} = 0.29$, respectively. These values are similar to the reported data for single phase austenitic and single phase ferritic steels [72,109].

The phase strains at macroscopic yielding point were determined as: $\varepsilon_{11}^{\gamma}$ = 3200 μstrain, $\varepsilon_{22}^{\gamma} = \varepsilon_{33}^{\gamma}$ = -520 μstrain for retained austenite and $\varepsilon_{11}^{\alpha}$ = 1890 μstrain and $\varepsilon_{22}^{\alpha} = \varepsilon_{33}^{\alpha}$ = -380 μstrain for α-matrix (Fig.20a, Fig.7.21a). Inputting these observed values into Eq.7.1, the volume-averaged phase stresses for retained austenite and α-matrix at $\mathbf{R_{p0.2}}$ of 500MPa were

calculated as 756 MPa and 447 MPa, respectively. The average phase stresses should satisfy the equilibrium condition by assuming the rule of mixture [72,109,117]:

$$f^{\gamma}\sigma_{11}^{\gamma} + (1 - f^{\gamma})\sigma_{11}^{\alpha} = \sigma_{appl} \tag{7.2}$$

where f^{γ} is the retained austenite volume fraction, σ_{appl} is the applied stress and $\sigma^{\gamma}, \sigma^{\alpha}$ are the volume-averaged phase stresses in the retained austenite and α-matrix, respectively. Taking into account the retained austenite volume fraction at 500MPa of f^{γ} = 6.5% (Fig.7.23b), the stress balance is then calculated as:

$$0.065 \times 756MPa + (1 - 0.065) \times 447MPa = 467MPa\,.$$

The same procedure was used to calculate the average phase stresses in sample **H** (Fig.7.20, 7.21). Since retained austenite in this sample does not transform even at the macroscopic yield point the initial volume fraction of 4% was taken into account at $\mathbf{R_{p0.2}}$ = 600MPa (Fig.7.24b). The volume-averaged phase stresses in the α-matrix and critical transformation stress for the austenite-to-martensite phase transformation were obtained as 875MPa and 546MPa, respectively, leading to stress balance for sample **H** as follows:

$$0.04 \times 875MPa + (1 - 0.04) \times 546MPa = 560MPa\,.$$

The obtained discrepancy in stress balance in both cases is probably caused by experimental errors and possible influence of initial residual stresses in the α-matrix and retained austenite. Nevertheless, the critical stress values for yielding in both microstructural phase constituents are clearly larger in sample **H**. This is due to the higher yield stress of the α-matrix in sample **H** stemming from the higher bainite volume fraction in its microstructure. At the same time, the higher carbon content in the retained austenite and/or its different morphological form leads probably to the higher critical stress for the austenite-to-martensite transformation.

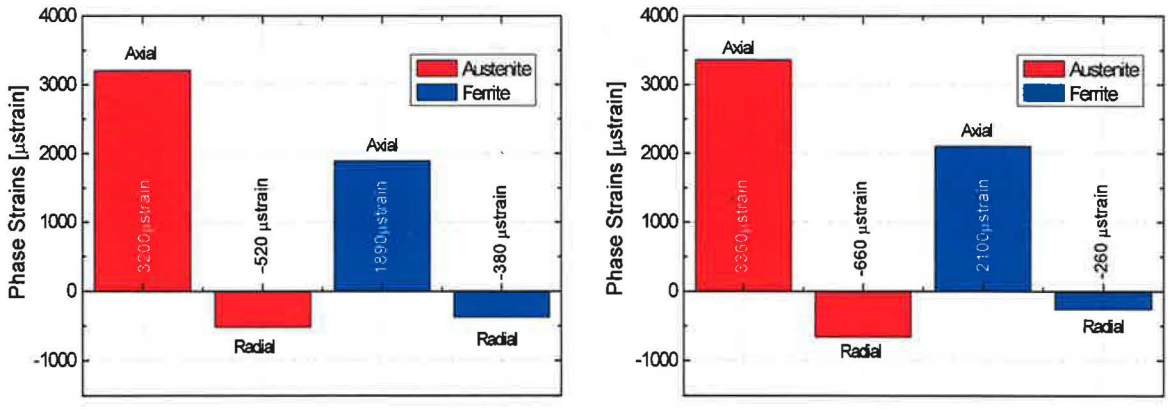

(a) **(b)**

Figure 7.21a,b: Austenite and α-matrix phase stresses determined at macroscopic yielding points of both tested TRIP steels, **(a)** for sample **G** at $R_{p0.2}$ = 500 MPa, **(b)** for sample **H** at $R_{p0.2}$ = 600 MPa.

7.2.6 Intergranular Strain Evolution during Tensile Straining

The dependence on the applied stress of lattice strains of individual reflections of the ferrite-bainite matrix and retained austenite are hereafter referred to as lattice plane responses. This allows us to follow the load partitioning not only between different phases but also between sets of similarly oriented grains. Fig.7.22a,b shows the evolution of lattice strains of α-matrix grain families $\{200\}_\alpha$, $\{310\}_\alpha$, $\{110\}_\alpha$ and retained austenite grain families $\{200\}_\gamma$, $\{310\}_\gamma$, $\{220\}_\gamma$ during the tensile test on sample **G**. The difference in slopes of the *hkl*-responses of both phases below the elastic limit (indicated by horizontal dotted lines in Fig.22a,b) are due to the load partitioning between grains controlled by the cubic elastic anisotropy factor (Eq.5.7). For cubic steel phases, the higher A_{hkl} implies higher stiffness (diffraction elastic constant, E_{hkl}) of <*hkl*> grain families aligned axially to the loading direction [117,119]. Therefore, the axial stiffness of the selected grain families of the α-matrix is increasing in following order $\{200\}_\alpha$, $\{310\}_\alpha$, $\{110\}_\alpha$ since $A_{200}<A_{310}<A_{110}$. Similarly, the stiffness of retained austenite grain families $\{200\}_\gamma$, $\{310\}_\gamma$, $\{220\}_\gamma$ increases in the same order since $A_{200}<A_{310}<A_{220}$. This trend can be clearly seen in the ferrite-bainite α-matrix response (Fig.7.22a) as well as in the retained austenite response (Fig.7.22b) to the applied load below the elastic limit.

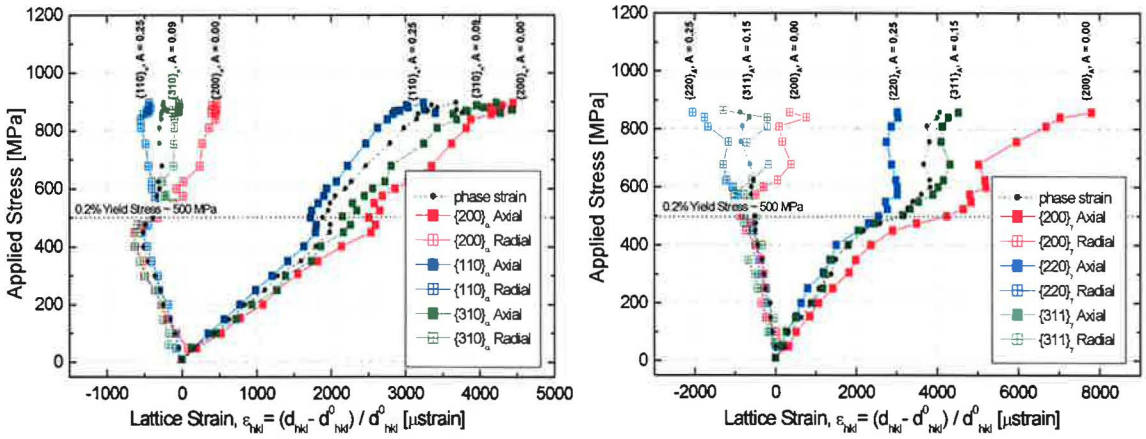

Figure 7.22a,b: Lattice plane responses (applied stress vs. lattice strain) of selected ferrite reflections **(a)** and retained austenite reflections **(b)** during tensile deformation of the sample **A**. The dashed lines indicate the yield point of 500 MPa. Statistical fit uncertainties for the retained austenite peaks range from 50 to 250 microstrains, depending on the peak intensity, the statistical error of ferrite peaks are from 15 to 25 microstrains.

Beyond the elastic limit, the lattice plane responses show deviations from linearity in qualitative agreement with the phase stresses discussed earlier. In order to interpret properly the individual lattice plane responses in Fig.22a,b, dedicated micromechanics modelling of the TRIP deformation capable of simulating the lattice plane responses (e.g. similar to the

models developed for phase transforming SMAs [120], and single phase elasto-plastic deformation [121]) has to be developed.

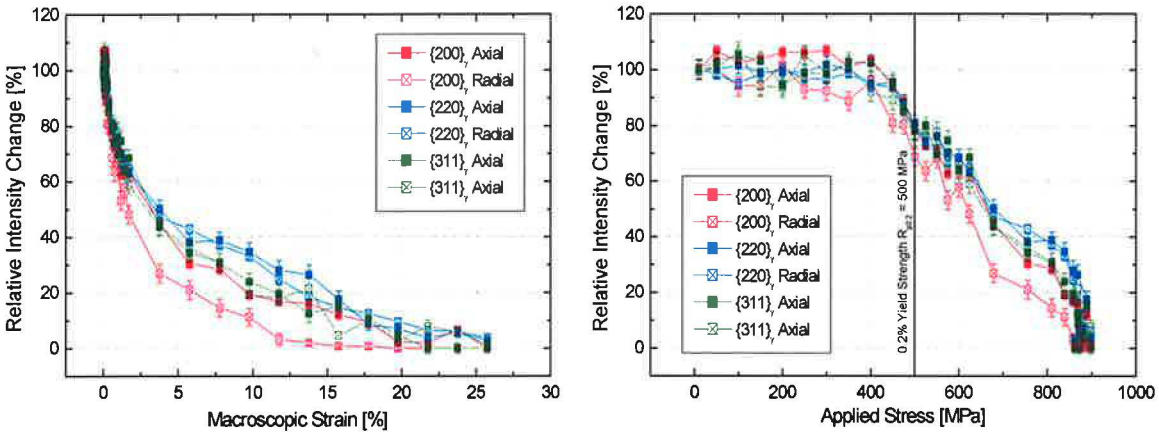

Figure 7.23a,b: Lattice plane responses (relative integrated intensity vs. applied stress **(a)** and macroscopic strain **(b)** during tensile deformation of the sample **G**.

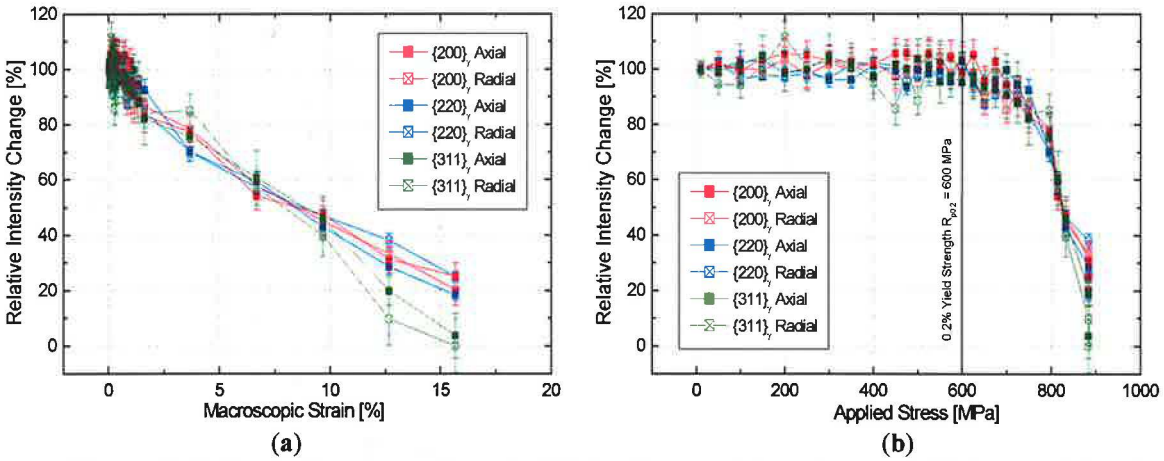

Figure 7.24a,b: Lattice plane responses (relative integrated intensity vs. applied stress **(a)** and macroscopic strain **(b)** during tensile deformation of the sample **H**.

7.2.7 Transformation Kinetics of Retained Austenite during Tensile Straining

Finally, the evolution of integrated intensities of few selected reflections of the retained austenite: $\{200\}_\gamma$, $\{310\}_\gamma$, $\{220\}_\gamma$) during the tensile tests are presented in Fig.7.23a,b (sample **G**) and Fig.7.24a,b (sample **H**). Relative intensity changes were evaluated by normalizing the integrated intensities to those measured prior to the tensile test. Since the intensities of all studied austenite reflections of sample **G** do not change significantly in the elastic range (Fig.7.23b), and decrease strongly beyond the yield point (Fig.7.23a), it is obvious that the austenite-to-martensite transformation plays a significant role in the TRIP deformation mechanism of sample **G**, particularly in the strain range 0-10%. The rate of decrease of the relative intensity with macroscopic strain is largest for the $\{200\}_\gamma$ austenite reflection suggesting the austenite-to-martensite transformation proceeds fastest in the austenite grains

oriented with <200> crystal direction parallel to the load axis. This clearly demonstrates the importance of the fact that the load redistribution takes place not just between distinct phases but also between differently oriented grain families of individual constituent phase. This might be quite important: a qualitative explanation for the observed behaviour has been given by Oliver, et al. [122] although, the above mentioned micromechanics modelling would again be necessary for a full quantitative interpretation of the differences between lattice plane responses of individual grain families. It is interesting to note that the integrated intensity responses measured on sample **H** are quite different (Fig.7.24a,b). The intensities of all austenite reflections start to decrease at 700MPa which is far beyond the 0.2% yield stress level (Fig.7.24b) and decrease rather slowly with macroscopic strain leaving still retained austenite remaining at the failure point at 15% strain. One possibility to rationalize this would be plastic deformation in the retained austenite preceding the austenite-to-martensite transformation, but other explanations might exist as well. In any case, sample **G** with higher volume fraction of austenite and less strong α-matrix seems to be a better TRIP steel (it has the same strength and higher elongation compared to sample **H**, Fig.7.15).

7.2.8 Brief Summary

Results of *in situ* neutron diffraction experiments on two TRIP-aided steels with the same chemical composition but different microstructures have shown that the applied tensile load (originally equally shared by austenite and α-matrix in the elastic range) is redistributed at the yielding point in such a way that the harder retained austenite bears significantly larger load than the softer α-matrix. Only after this load partitioning is finished, macroscopic yielding of the TRIP steel takes place through simultaneous activity of the martensitic transformation (in the austenite phase) and plastic deformation (in the α-matrix) processes. The transforming retained austenite thus provides the potential for high ductility of the TRIP steel but at the same time acts as a "*reinforcement phase*" during the plastic deformation of its complex multiphase microstructure. The alloy with higher volume fraction of austenite and less strong α-matrix (sample **G**) seems to be a better TRIP steel. Despite its lower α-matrix yield stress, it has the same strength but higher ductility than the second alloy (sample **H**) and the strain-induced austenite-to-martensite phase transformation is more effective in the TRIP deformation mechanism.

8.

TENSILE BEHAVIOUR OF SINGLE AND MULTIPHASE STEELS

Investigation of the *hkl*-reflections response on the applied stress in deformed crystalline materials can give us very important information on the interphase, intergranular and residual strains generation during straining. Macroscopic properties are closely related to the particular grain family deformation behaviour which can be measured by the *in situ* neutron/synchrotron diffraction technique. Thanks to the unique feature of the neutron/synchrotron diffraction lattice strain measurement of a well-defined subset of grains each diffraction peak provides insight on the *Type I, II* and *III* (see chapter 4) elastic strains within the strained gauge volume. In order to study the tensile behaviour of selected single and multiphase steels the *hkl*-reflections ($\{110\}_\alpha$ and $\{111\}_\gamma$) responses on the applied stress were studied by neutron diffraction during uniaxial loading tests at room temperature.

8.1 IN SITU DEFORMATION INVESTIGATION OF SINGLE FERRITIC STEEL

8.1.1 Material and Experimental Procedure

The commercial steel WELDOX 700 was used as an experimental material. This is a general steel with the minimum yield strength of 700 MPa intended for applications where its high strength permits weight savings to be made. The steel is fine grained and microalloyed to a total of at least 0.040 % with Al, V, NB, Ti, whereas its complete chemical composition is shown in Tab.8.1.

Table 8.1: Chemical composition of used high strength steel (wt. %)

C	Si	Mn	P	S	Nb	Cr	V	Cu	Ti	Al	Mo	Ni	N
0.20	0.60	1.60	0.02	0.01	0.04	0.70	0.09	0.30	0.04	0.02	0.70	2.00	0.02

In situ neutron diffraction experiments were performed on dedicated high resolution stress/strain diffractometer (TKSN-400) at NPI (for detail see 6.1.2). The width of slits was 2 mm yielding thus the specimen gauge volume of about 12 mm^3. Tensile stress was applied in a step-by-step manner and neutron diffraction profiles were recorded during temporary stops of the crosshead. Several unloads were performed during experiment in order to measure the evolution of intergranular residual strain as a function of accumulated plastic strain. An exposure time of 1 hour was necessary to obtain sufficiently good statistics to perform a

reliable analysis of diffraction profiles. Ferrite lattice strain, $\varepsilon^{\alpha}_{110}$, was determined from the shift of the diffraction angle, θ_{110}, of ferrite $\{110\}_{\alpha}$ diffraction profile (see Eq.5.2). With a view of obtaining the ferrite lattice plane strains in both directions (axial $\Rightarrow \varepsilon^{\alpha}_{11}$, radial $\Rightarrow \varepsilon^{\alpha}_{22}=\varepsilon^{\alpha}_{33}$) two samples were examined with the different experimental arrangement, respectively.

8.1.2 Macroscopic Stress-Strain Behaviour

The macroscopic stress-strain curve recorded during neutron data acquisition is shown in Fig.8.1. The macroscopic Young's modulus (**E**), the conventional yield strength ($\mathbf{R_{p0.2}}$) and the tensile strength ($\mathbf{R_m}$) have been determined as 210 GPa, 725 MPa and 820 MPa, respectively. These values coincide well with those given by steel producer (**E** = 210 GPa, $\mathbf{R_{p0.2}}$ = 700 – 720 MPa, $\mathbf{R_m}$ = 780 - 930 MPa). As it can be clearly seen in Fig.8.1 the stress-strain curve after the yielding point ($\mathbf{R_{p0.2}}$ = 725 MPa) is composed of a series of steps, which correspond to the creep deformation during the period when the load was held constant.

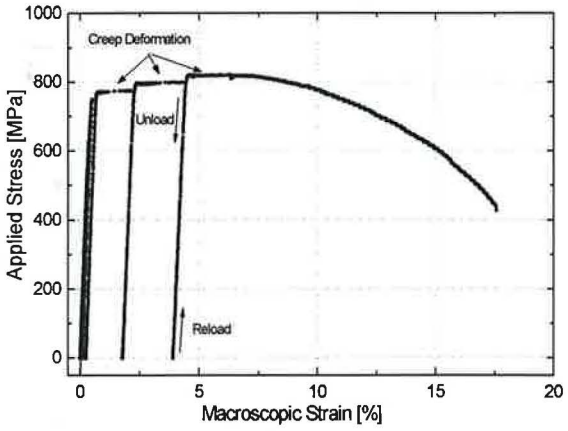

Figure 8.1 Stress-strain curve acquired during the *in situ* neutron diffraction experiment.

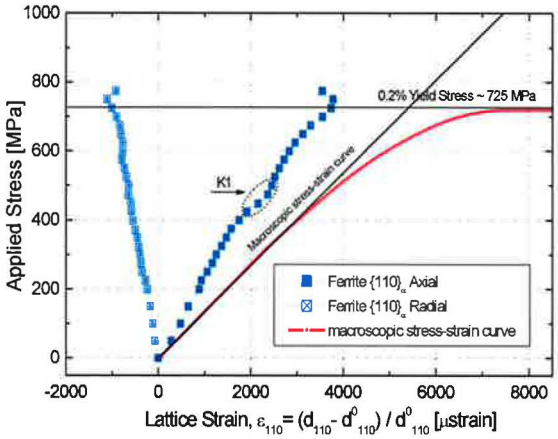

Figure 8.2 Change in lattice strain with tensile straining for ferrite $\{110\}_{\alpha}$ reflection.

8.1.3 Ferrite $\{110\}_{\alpha}$ Lattice Plane Strain Response

Fig.8.2 shows changes of ferrite $\mathbf{\{110\}_{\alpha}}$ lattice strains ($\varepsilon^{\alpha}_{11}$ and $\varepsilon^{\alpha}_{22}=\varepsilon^{\alpha}_{33}$) measured independently in the axial and radial direction, as a function of the applied stress. The lattice strain was calculated by using the lattice spacing before loading as the reference value neglecting thus any initial residual strains. The ferrite lattice strain is increasing in both directions with applied stress, almost linearly up to the yielding point, suggesting thus elastic deformation. However, the conventional yield strength was determined only at 725 MPa (Fig.8.1), there it is obvious kink in lattice strain response on the applied load already at around 475 MPa (point **K1**, Fig.8.2). The reason is speculated either it can correspond to the

yielding in different grain families or it is caused by partial release of dislocations in some of the **<110>$_\alpha$** oriented grain family, which brings about microplastic deformation.

8.1.4 Changes in FWHM and Dislocation Density during Tensile Test

Stress/strain fields that vary over a scale much smaller than the gauge volume (i.e. *Type II* and *Type III microstresses*, see chapter 4) give rise to the peak broadening effect. As it can be seen in Fig.8.3a, the Full Width at Half Maximum (FWHM) of the ferrite **{110}$_\alpha$** diffraction peak increases with loading and falls back after unloading completely in the elastic region and partially in the plastic region. The reversible changes in the peak width correspond to the heterogeneous elastic strain distribution between particular grains families within the strained sample gauge volume. Whereas in the elastic region the change in the peak width is completely reversible due to already mentioned heterogeneous elastic strain caused by anisotropy of elastic properties at the grain size scale (*Type II*), the FWHM changes in the plastic region, are not completely reversible upon unloading. Irreversible increase in diffraction peak width during plastic deformation can be due to a combination of *Type II* and *Type III* microstresses variation within the diffracted grains [72]. Peak broadening caused by microstress (*Type II* + *Type III*) variation within grains is often categorized by the root mean square strain (RMSS), $\langle \varepsilon^2 \rangle^{1/2}$ (Fig.8.3b,c) [72,123,124].

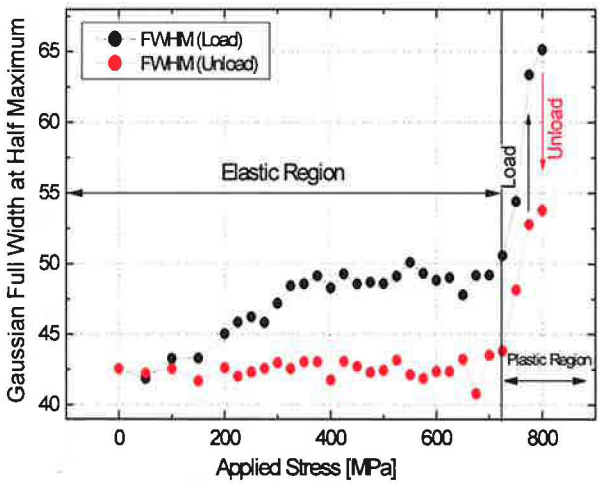

Figure 8.3a Change in the Gaussian FWHM (Full Width at Half Maximum) upon tensile load (black) and unload (red).

In what follows, we will treat the observed peak broadening effects in a rather rough approximation based on simple integral breath method [123,124]. Both instrumental resolution function and experimentally observed broadened profiles are approximated by Gauss fitted profiles of and the simple deconvolution method can be then performed according to the following formulas:

$$FWHM^2_{exp} = FWHM^2_{spec} + FWHM^2_{spec} \tag{8.1}$$

$$FWHM_{spec} = \sqrt{FWHM^2_{exp} - FWHM^2_{inst}}\,, \tag{8.2}$$

where $FWHM_{spec}$ is the width of the specimen broadened profile, $FWHM_{inst}$ is the width of the instrumental resolution function and $FWHM_{exp}$ is the width of experimentally observed diffraction profile. Afterwards, the root mean square strain (RMSS) can be determined according to Ref. [123,124] as:

$$\left\langle \varepsilon^2 \right\rangle^{1/2} = \frac{\cot\theta}{4\sqrt{-2\ln 1/2}} \sqrt{FWHM^2_{exp} - FWHM^2_{inst}} \tag{8.3}$$

The result of this procedure is displayed in following figures (Fig.8.3b,c).

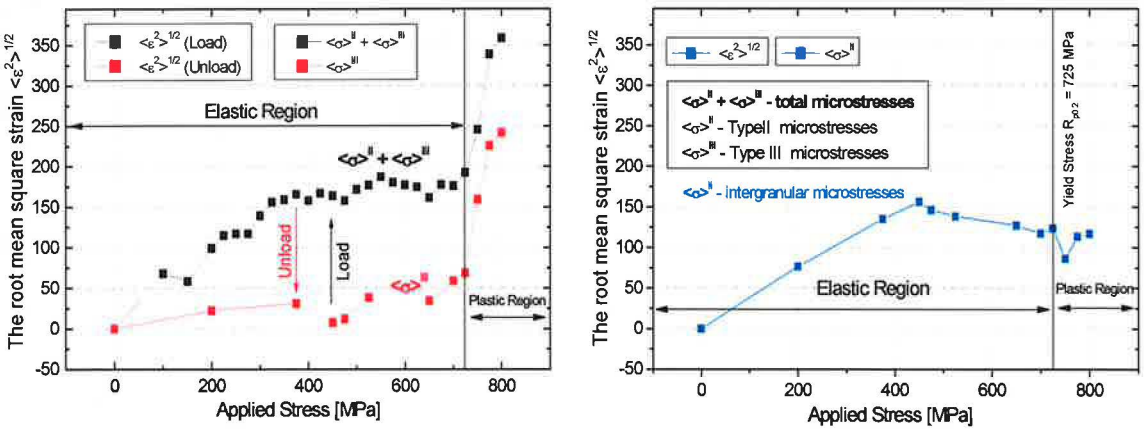

Figure 8.3b,c Change in the RMSS (Root Mean Square Strain) estimated from Gaussian FWHM upon tensile load (black) and unload (red). It has been assumed that RMSS estimated for FWHM measured upon loading corresponds to total microstress (*Type II* + *Type III*) while RMSS estimated from FWHM measured upon unloading corresponds only to *Type III* microstress. **(c)** An evolution of the *Type II* microstress estimated as a difference from measured total and *Type III* microstresses.

The experimental result shown in Fig.8.3b indicate a unique possibility to distinguish between two different types of microstresses (*Type II* + *Type III*) contributing to the observed changes in FWHM of diffraction peak (Fig.8.3a). Since neutron diffraction spectra have been alternately collected upon loading and unloading (Fig.8.1), it can help us roughly assume that FWHM of ferritic diffraction profile measured upon loading corresponds to the presence of total microstresses ($\langle\sigma\rangle^{II} + \langle\sigma\rangle^{III}$, Fig.8.3b, black points) whereas FWHM measured upon unloading corresponds only to *Type III* ($\langle\sigma\rangle^{III}$) microstress (Fig.8.3b, red point). The evolution of intergranular microstress (*Type II*, $\langle\sigma\rangle^{II}$) estimated as a difference of the measured total and *Type III* microstresses (Fig.8.3b) is plotted in Fig.8.3c. *In situ* neutron diffraction method thus provides unique information on macrostresses (*Type I*) and microstress (*Type II* + *Type III*)

present in material and thus help us to predict their possible influence on mechanical properties.

Since *Type III* microstress is in this case mostly due to presence of dislocations causing very severe short-range elastic strains, it is possible to use the microstructural parameter RMSS for rough estimate of the increase of the dislocation density ρ [72]. It can be done, for example, according to a very simple dislocation density model of Williamson and Smallman [125]:

$$\rho = \frac{K\langle \varepsilon^2 \rangle}{Fb^2} \tag{8.4}$$

where ***b***, ***F*** and ***k*** represent the magnitude of Burger's vector, the factor describing interaction between dislocations, and a constant, respectively. In the present case, we assume ***F*** = 1, ***k*** =14.4 for *b.c.c.* lattice with a Burger's vector along <111> direction according to Ref. [125]. However, this rough model is not valid if the dislocations are clustered into cells or boundaries [72].

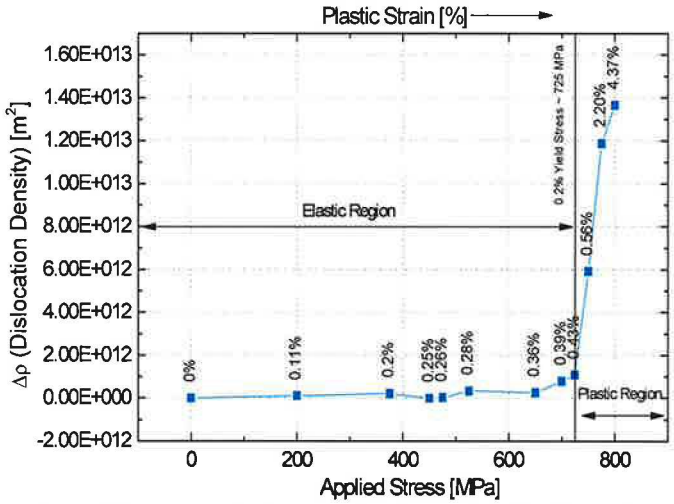

Figure 8.4 An increase in dislocation density estimated from the FWHM (unload, Fig.8.3) during the tensile test as a function of the applied stress.

The change in the dislocation density during tensile straining of examined ferritic steel is plotted as a function of the applied stress in Fig.8.4. As it is seen, at the beginning of deformation, dislocation density hardly varies with increasing applied stress. This means that the deformation is only elastic probably accompanying by little generation of lattice defects. The onset stress of an increase in dislocation density coincides with yield stress of 725 MPa, after this point dislocation density is dramatically increasing up to the sample failure.

8.1.5 Evolution of Intergranular Residual Strain (Stress) during Tensile Test

Intergranular residual strains/stresses generation as a function of accumulated plastic strain during tensile test can be clearly seen in Fig.8.5 and Fig.8.6. The magnitude of the residual strain (see Fig.8.5) generated in axial direction is of about three times larger than in the radial direction corresponding thus to the diffraction Poison's ratio (ν^{α}_{110}= 0.28). At the beginning of the plastic deformation the intergranular residual strain generation rate is high, but above the plastic strain **ε** > 0.1% residual strains increase slowly. Nevertheless, a small increase in the intergranular residual strain magnitudes can be observed even at applied plastic strain of 0.4 % (Fig.8.5).

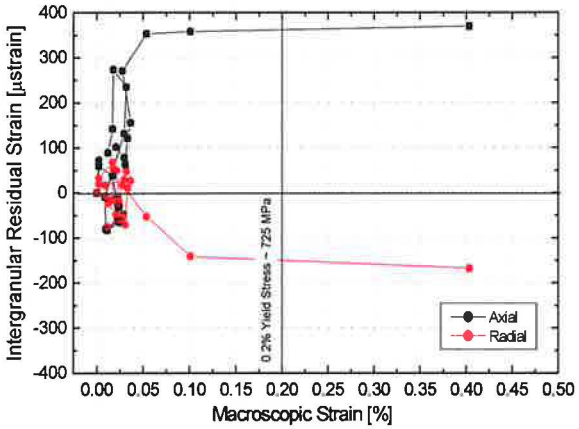

Figure 8.5 The evolution of residual strain as a function of accumulated plastic strain.

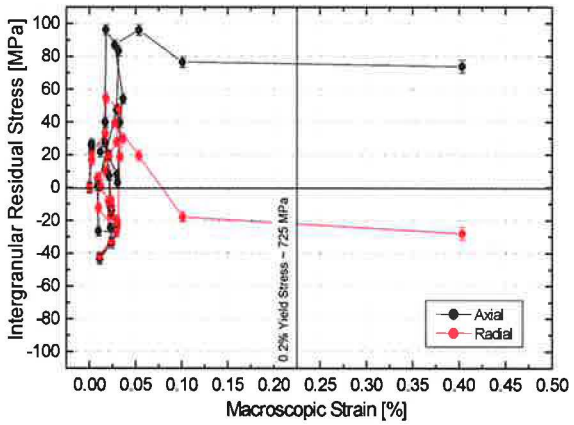

Figure 8.6 The evolution of residual stress as a function of accumulated plastic strain.

Measured intergranular residual strains in the axial ($\varepsilon^{\alpha}_{11}$) and radial ($\varepsilon^{\alpha}_{22}=\varepsilon^{\alpha}_{33}$) direction were recalculated to the intergranular residual stresses by means of Hooke's Law (Fig.8.6). For axial direction (σ^{α}_{11}) and radial direction (σ^{α}_{22} = σ^{α}_{33}) Hooke's Law is written as:

$$\sigma^{\alpha}_{11} = \frac{E^{\alpha}_{110}}{(1+\nu^{\alpha}_{110})(1-2\nu^{\alpha}_{110})}\left[(1-\nu^{\alpha}_{110})\varepsilon^{\alpha}_{11} + 2\nu^{\alpha}_{110}\varepsilon^{\alpha}_{22})\right], \text{ and} \tag{8.5}$$

$$\sigma^{\alpha}_{22} = \sigma^{\alpha}_{33} = \frac{E^{\alpha}_{110}}{(1+\nu^{\alpha}_{110})(1-2\nu^{\alpha}_{110})}\left[\nu^{\alpha}_{110}\varepsilon^{\alpha}_{11} + (1-\nu^{\alpha}_{110})\varepsilon^{\alpha}_{22} + \nu^{\alpha}_{110}\varepsilon^{\alpha}_{22})\right]. \tag{8.6}$$

Generation of the intergranular residual stresses as a function of the accumulated plastic strains during tensile straining is clearly seen from Fig.8.6. The intergranular residual stress in axial direction was determined of about 80 MPa and in the radial direction of about -20 MPa. If we consider the yield strength of 725 MPa these intergranular stresses are too small to cause any macroscopic cracks, but they can be important in the case of the following deformation process (i.e. cyclic deformation).

8.1.6 Brief Summary

Single ferritic steel with high yield strength (WELDOX 700) was studied during uniaxial loading by means of the *in situ* neutron diffraction technique. The evolution of the lattice strain in the ferrite $<110>_{\alpha}$ oriented grain family and the intergranular residual strains/stresses generation as a function of the accumulated plastic strain was analyzing in axial and radial directions, respectively. The main obtained results are the following:

- lattice plane strain is proportional to the applied stress in the elastic regime, however a small deviation from linearity is observed even in the elastic region, which is probably corresponding to the partial movement of dislocations in some of ferritic $<110>_{\alpha}$ oriented grains or plastic already occurs in others ferrite grain families
- the FHWM changes in the elastic regime are related to the heterogeneous elastic strain distribution between individual grains within the strained sample gauge volume
- the FHMW changes in the plastic region are corresponding to the evolution of microstrain (represented by RMSS) which is mainly related to the dislocation density changes
- the generation of the intergranular residual strains/stresses as a function of the accumulated plastic strain shown that $\{110\}_{\alpha}$ grain family in axial direction retains in tension, whereas the same ferrite grain family in radial direction retains in compression.

8.2 IN SITU DEFORMATION INVESTIGATION OF DUPLEX STAINLESS STEEL

8.2.1 Investigated Material and Experimental Arrangement

The commercial duplex stainless steel (SAF 2507) has been chosen as an experimental material for *in situ* tensile testing. This multiphase steel has an excellent combination of mechanical and corrosion-resistant properties which are exploited in the various applications. Tested material with chemical composition given in Tab.8.2 was provided by Sandvik AB (Sandviken, Sweden) in the form of cold-worked rods with diameter of 30 mm. In order to prepare the austenite-ferrite microstructure (Fig.8.7) which is free from carbides and intermetallic phases at grain boundaries the steel was subjected to the heat treatment, consisting of annealing at the 1050 °C for 1 hour, followed by water cooling (quenching). The phase composition of such treated steel was determined by the image analysis and the austenite volume fraction of 34%±3% has been found [126]. The tensile specimens for *in situ*

KNIHOVNA MAT.-FYZ. FAKULTY
Knihovna Fr. Živnský (fyz. odd.)
Ke Karlovu 3
121 16 Praha 2

neutron diffraction experiment were machined with gauge diameter of 5 mm and the gauge length of 14 mm.

Table 8.2: Chemical composition of used steel (wt. %)

C	Cr	Mo	Ni	N
0.02	2.50	3.80	7.00	0.27

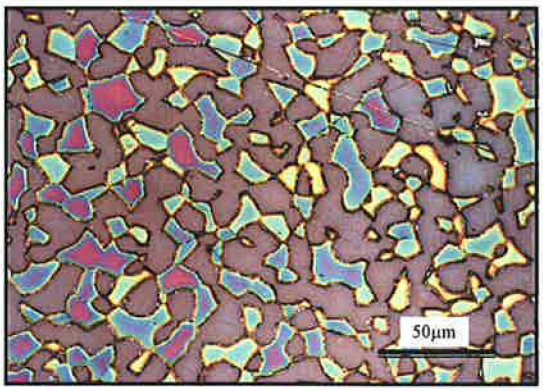

Figure 8.7 Micrograph of the SAF2507 steel consists of ferrite and austenite phase.

The *in situ* neutron diffraction experiment was performed on the high-resolution diffractometer TKSN-400 at NPI (see section 6.1.2 for details). The specimens were deformed in tension in a step-by-step manner up to the sample fracture similar to previous experiment (see section 8.1). As it is usual for the *in situ* neutron diffraction experiments the diffraction profiles were recorded during temporary stops (1 hour). The detector window was set to cover ferrite $\{110\}_{\alpha}$ and austenite $\{111\}_{\gamma}$ reflections, simultaneously.

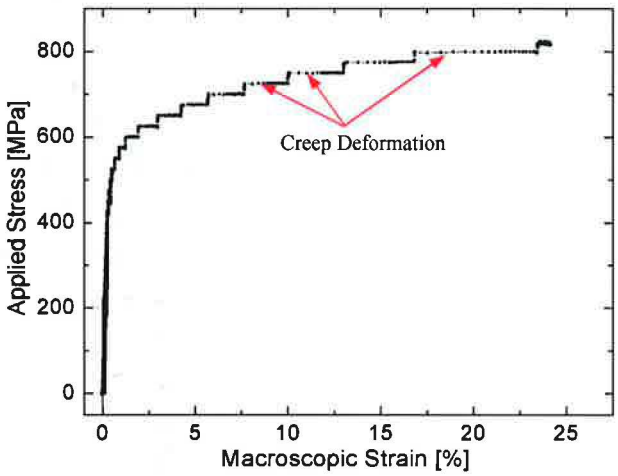

Figure 8.8 A macroscopic stress-strain curve of the duplex stainless steel obtained by a step-wise tensile test.

8.2.2 Macroscopic Stress-Strain Behaviour

Fig.8.8 shows the experimental stress-strain curve obtained during *in situ* tensile test. The macroscopically determined mechanical properties are as follows: Young's modulus, **E** = 200 GPa, yielding strength, $\mathbf{R_{p0.2}}$ = 525 MPa, and tensile strength, $\mathbf{R_m}$ = 820 MPa. As it is obvious from Fig.8.8 beyond the yielding point, the creep deformation in each of measuring step

occurs. Achieved mechanical properties are in the range of values provided by producer ($\mathbf{R_{p0.2}}$ = min. 500MPa, $\mathbf{R_m}$ = 760-930, **E** = 200 GPa and **A** = min.20%).

8.2.3 Ferrite and Austenite Lattice Strain Response

In the first approximation, the initial (thermal, ε_{hkl}^{ther}) lattice strains in both present phase constituents originate form the previous heat treatment, were neglecting Fig.8.9 thus that as the stress-free lattice spacing were taken those measured in the ferrite and austenite prior to the uniaxial loading test. Then we can write:

$$\varepsilon_{hkl}^{tot} = \varepsilon_{hkl}^{def} + \varepsilon_{hkl}^{ther}, \quad \varepsilon_{hkl}^{def} = \varepsilon_{hkl}^{tot} - \varepsilon_{hkl}^{ther}, \tag{8.3}$$

where ε_{hkl}^{def} is the lattice strain caused by tensile deformation, ε_{hkl}^{tot} is the total measured lattice strain, and ε_{hkl}^{ther} is the thermal residual lattice strain (initial in our case), respectively [127]. In Fig.8.9 can be clearly seen that in the relationships between ε_{hkl}^{def} and applied stress during uniaxial straining the three stages (I, II, III) could be identified. At the stage I, both phases are elastically deformed, so that linear relations are found (E_{110}^{α} = 193 GPa, E_{111}^{γ} = 265 GPa). The difference in slopes is caused by different diffraction elastic moduli of the phase constituents.

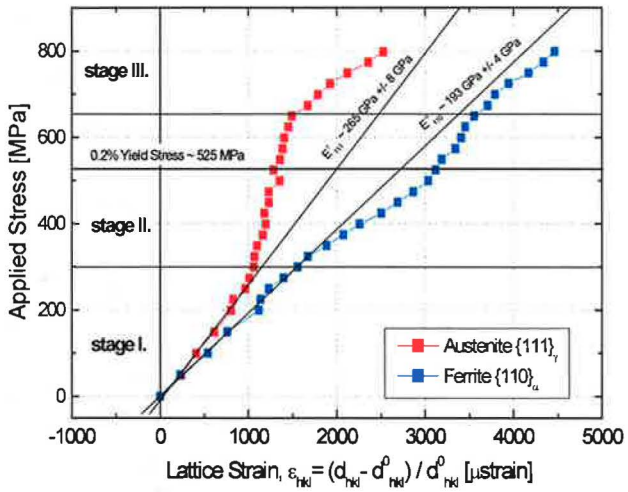

Figure 8.9 Lattice strain evolution in duplex steel during the uniaxial loading test without the initial (thermal) lattice plane strain.

Furthermore, from Fig.8.9 is obvious that the diffraction elastic modulus of **<110>**$_\alpha$ oriented ferritic grains is lower than that of austenitic **<111>**$_\gamma$ oriented grains. At the stage II, the soft austenite is plastically deformed, while the hard ferrite is still deformed elastically. During this stage, the applied load is transferred away from plastically deformed austenite **<111>**$_\gamma$ oriented grains towards plastically stiffer ferritic **<110>**$_\alpha$ oriented grains. As a result, the austenite lattice strain ($\varepsilon_{111}^{\gamma}$) increases more slowly with increasing applied stress, while

the ferrite lattice strain ($\varepsilon^{\alpha}_{110}$) increases more rapidly. At the stage III, both phases are deformed plastically, resulting in the $\varepsilon^{\gamma}_{111}$ of austenite phase increasing rapidly again with increasing applied load (Fig.8.9b).

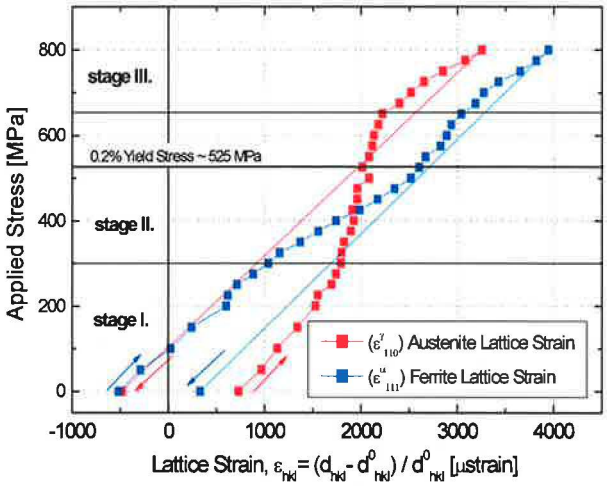

Figure 8.10 Lattice strain evolution in both present phase constituents in duplex steel during the uniaxial loading test with the initial (thermal) lattice plane strains.

Since the initial (thermal, ε^{ther}_{hkl}) strains have been already determined on the same material by Jenčuš et al. [126] as follows: tensile ($\varepsilon^{\gamma}_{111}$ = 730±20 μstrain) for austenite **{111}$_{\gamma}$** and compressive ($\varepsilon^{\alpha}_{110}$ = -520±20 μstrain) for ferrite **{110}$_{\alpha}$** grain families, we will consider their influence on deformation process. It is assumed that these interphase residual strains were generated during quenching from 1050 °C to 25 °C due to the difference in thermal expansion coefficients of ferrite and austenite [128], therefore, we term them as thermal. The presence of any initial strains/stresses has great influence on the deformation behaviour of the particular phase constituents as well as on the deformation behaviour of the alloy. In our case it has been expected that austenite which has been in tension prior to the tensile test will flow plastically earlier than ferrite which is at the beginning of the test in compression (although austenite has probably lower yield stress as well). As it is seen from Fig.8.9 and Fig.8.10 this assumption has been confirmed and austenite reached tensile yielding point at lower stresses (earlier) than ferrite. Furthermore, in Fig.8.10 can be clearly seen not just an evolution of the austenite and ferrite lattice strains during ($\varepsilon^{\gamma}_{111}, \varepsilon^{\alpha}_{110}$) the tensile straining but also their impact on the final (residual) interphase strains after unloading. It has been found that ferrite **<110>$_{\alpha}$** oriented grain family retains in tension and austenite **<111>$_{\gamma}$** oriented grain family retains in compression. It is assumed that high compressive residual strain in austenite after tensile

deformation can accelerate plastic flow when a specimen is subsequently deformed in compression, resulting in a large Bauschinger effect occurring in dual-phase alloys [128,129].

8.2.4 Brief Summary

Macroscopic stress-strain curves and changes in the lattice strain (ε_{hkl}) in the multiphase steel (SAF 2507) during tensile deformation were successfully measured simultaneously by *in situ* neutron diffraction. The changes in the lattice strains in the austenite ($\varepsilon^{\gamma}_{111}$) and ferrite ($\varepsilon^{\alpha}_{110}$) phase, respectively, during tensile deformation are divided into three stages, showing elastic a plastic inhomogeneity. The main results obtained by *in situ* neutron diffraction are the following:

- it was clearly shown that austenite in this steel is plastically softer phase than ferrite in contrast to the TRIP-aided multiphase steel where austenite is plastically harder phase than ferrite-bainite α-matrix (see chapter 7)
- load redistribution during the yielding is described, while it is obvious that applied load is transferred from plastically softer austenite grains towards plastically harder ferrite grains
- it is assumed that the high compressive residual strain found in austenite phase after tensile straining can accelerate plastic flow when a specimen is subsequently deformed in compression, resulting in a large Bauschinger effect.

CONCLUSIONS

This thesis deals with the experimental results obtained by the application of neutron diffraction methods to studies of the problem of the deformation and transformation processes taking place in structural steels during thermo-mechanical controlled processing at high temperatures and during the tensile straining at room temperature. Commonly, our understanding of deformation/transformation processes occurring in steels during low/high temperature treatment comes form *ex post* microstructure studies and modelling. The *in situ* neutron diffraction results provide unique phase and structure specific information on the microstructures under stress or/and temperature conditions at which the deformation or/and transformation processes take place.

Neutron diffraction experiments were carried out on two neutron diffractometers dedicated to stress/strain measurements - high-resolution stress/strain diffractometer TKSN-400 at NPI in Řež near Prague, Czech Republic and ENGIN-X at ISIS neutron spallation source in RAL Chilton, United Kingdom.

In the first part of the project (Chapter 6), the *in situ* neutron diffraction technique, using the dedicated diffractometer TKSN-400, has been employed to study deformation and transformation processes in low-alloyed (Nb-free, Nb-added) steels and low-alloyed (Si-Mn) TRIP-aided multiphase steel during the various TMCPs in a wide temperature range ($20^{\circ}C<T<900^{\circ}C$). The analysis of the neutron diffraction profiles of Nb-free and Nb-added low-alloyed steels has revealed that austenite pre-deformation and a small amount of the Nb addition enhanced the starting temperature of the austenite-to-ferrite phase transformation. Furthermore, the lattice changes both in the single austenite (or ferrite) region and in the dual phase region were also evaluated from the neutron diffraction profiles, suggesting thermal contraction of crystalline lattice of both phases.

As regards the low-alloyed (Si-Mn) TRIP-aided multiphase steel, the neutron diffraction has been employed in the optimization process of the TMCP for this type of structural steel. In fact, the transformation temperature and isothermal holding time criteria of the austenite-to-ferrite phase transformation has been defined just on the basis of results obtained by the *in situ* neutron diffraction experiments. Information received from this studies were utilized to propose more advanced TMCPs of bulky TRIP-aided steels, particularly the deformation, thermal and holding time criteria.

In the second part of the project (Chapter 7), the deformation/transformation behaviour of TRIP-aided multiphase steels during the tensile straining at room temperature was investigated by *in situ* neutron diffraction methods using both TKSN-400 and ENGIN-X diffractometers. Tensile deformation of differently treated Si-Mn TRIP-aided steels was studied with the aim to achieve a better understanding of the TRIP deformation mechanisms which combines transformation and plastic deformations processes. It was found that applied tensile load is significantly redistributed at the yielding point. The harder retained austenite bears significantly larger load than the softer ferrite-bainite α-matrix. Only when load partitioning between present phase constituents is finished, macroscopic yielding of the TRIP steel takes place through simultaneous activity of the martensitic transformation (in the retained austenite) and plastic deformation (in the α-matrix) processes. The strain-induced martensitic transformation of retained austenite thus yields the potential for high ductility of the TRIP steel but at the same time acts as a "*reinforcement phase*" during yielding. Moreover, the neutron diffraction in combination with microstructural observation has shown that the retained austenite transformation kinetics in TRIP steels and thus overall mechanical properties of the alloy strongly depends on microstructural characteristics of the present phase constituents (volume fraction, morphology, grain size, carbon content, etc.).

In the last part of the project (Chapter 8), the tensile deformation behaviour of single (ferritic) and multiphase (duplex stainless) steels at room temperature was studied by *in situ* neutron diffraction. It has been found that similarly to the TRIP steel, the load redistribution taking place upon yielding also in duplex stainless steels, but in contrast to the TRIP steel it is shown that austenite in duplex steels is plastically more compliant phase than ferrite. This load redistribution between austenite and ferrite phase constituents leads to the generation of high interphase residual strains, while austenite remains in compression and ferrite in tension after plastic deformation.

As regards the single ferritic steel, the evolution of the internal strains/stresses upon loading and unloading during tensile test was evaluated from the data obtained by the *in situ* neutron diffraction. Furthermore, the neutron diffraction was employed in the *in situ* studies for an estimate of dislocation density evolution during tensile straining.

The large variety of problems treated and resolved in the present doctoral thesis confirms usefulness and uniqueness of the *in situ* neutron diffraction method in the characterisation of processes occurring in thermally or/and mechanically treated crystalline materials.

DISSERTANT'S ROLE IN OBTAINED RESULTS

Author's contribution to the results represented in the thesis is following:

- deformation rig modifications at diffractometer TKSN-400 at NPI for performing *in situ* thermo-mechanically controlled processes
- preparation and carrying out *in situ* neutron diffraction experiments on the dedicated high-resolution stress/strain diffractometers TKSN-400 at NPI in Řež and NGIN-X at ISIS Facility
- performing the fitting and analysing of the obtained data by means of the fitting programs PeakFit and GSAS (General Structure Analysis System)
- performing some of microstructural observation by means of light and scanning electron microscopy
- active participating in physical interpretation of the all results obtained by *in situ* neutron diffraction

Furthermore, during my three-year stay at the Nuclear Physics Institute, as a post-gradual student I was the member of the scientific team of the Neutron Physics Department carrying out the neutron scattering experiments. Therefore, I have been participating in almost all diffraction measurements performed on TKSN-400, however my doctoral thesis is based only on a part of these results that thematically cover the tensile behaviour of the modern steel-based samples.

During my stay at Nuclear Physics Institute, I have became author and co-author of more than 17 scientific papers published in international journals and in proceedings of the international conferences. The PhD thesis is based mainly on the following eight contributions:

1. O. Muránsky, J. Zrník, P. Jenčuš, P. Lukáš, Neutron diffraction analysis of austenite transformation kinetics in Mn-Si TRIP steel, Acta Metalurgica Slovaca, 10, (2004), 228.
2. O. Muránsky, P. Lukáš, P. Šittner, J. Zrník, P. Jenčuš and Z. Nový, In situ neutron diffraction studies of phase transformations in Si-Mn TRIP steel, Materials Science Forum, vol. 490-491 (2005) pp: 275-280.
3. O. Muránsky, P. Lukáš, J. Zrník, P. Šittner, Neutron Diffraction Analysis of Retained Austenite Stability in Mn-Si TRIP Steel During Plastic Deformation, In Proc. of the ICNS 2005, Sydney, Nov. 27 - Dec. 2, 2005, Physica B, accepted.

4. O. Muránsky, P. Lukáš, P. Šittner, J. Zrník, E.C. Oliver, In situ neutron diffraction studies of tensile behaviour of TRIP-aided multiphase steel, The 3rd International Conference on Advanced Structural Steels, August 2006, submitted.
5. J. Zrník, O. Muránsky, P. Lukáš, P. Šittner, Z. Nový, In-situ neutron diffraction analysis of phase transformation kinetics in TRIP steel, Materials Science Forum, Vol. 502, December 2005, p. 339-344.
6. J. Zrník, O. Muránsky, P. Lukáš, Z. Nový, P. Sittner, P. Horňak, Retained austenite stability investigation in TRIP steel using neutron diffraction, J. of Materials Science & Eng., (September TMS2005), in print.
7. P. Jenčuš, P. Lukáš, O. Muránsky, J. Zrník, Z. Nový, Neutron diffraction studies of Si-Mn TRIP Steel upon thermo-mechanical processing, J. of Neutron Research, Vol. 12, 1-3, 2004, 243.
8. P. G. Xu, Y. Tomota, O. Muránsky, P. Lukáš and Y. Adachi, In situ neutron diffraction during thermo-mechanically controlled processing of C-Mn(-Nb) steels, Proc. of 150th ISIJ Meeting 2005, September 29-30, Hiroshima, Japan, CAMP-ISIJ, Vol. 18 (2005) 1300-1303.
9. P. G. Xu, Y. Tomota, O. Muránsky, P. Lukáš, and Y. Adachi, Austenite-to-Ferrite Transformation and Phase Strain Evolution in Low Alloy Steels during Thermo-mechanically Controlled Process Studied by In Situ Neutron Diffraction, Materials Science and Engineering A, accepted for publication (2006).

Besides of these publications which have been used in the present doctoral thesis I have also became co-author of following scientific contributions:

10. P. Jenčuš, J. Polák, P. Lukáš and O. Muránsky, In situ neutron diffraction study of the low cycle fatigue of the α-γ duplex stainless steel, In Proc. of the ICNS 2005, Sydney, Nov. 27 - Dec. 2, 2005, Physica B, accepted.
11. J. Zrník, O. Muránsky, P. Lukáš, Z. Nový, P. Sittner, P. Horňak, Retained austenite stability investigation in TRIP steel using neutron diffraction, J. of Materials Science & Eng., (September TMS2005), in print.
12. J. Zrnik, Z. Novy, P. Lukaš, O. Muránsky, P. Jenčuš and P. Wangyao, Study on transformation behavior of bulk Si-Mn TRIP steel, Journal of Metals, Materials and Minerals, Vol. 14, No.1 pp. 1-9, 2004.
13. P. Lukáš, O. Muránsky, P. Jencuš, J. Polák, In-situ neutron diffraction study of the low cycle fatigue of the α-γ duplex, in proc. of the 9th European Powder Diffraction Conference, September 2-5, 2004, Prague, Czech Republic, Zeitschrift fur Kristallographie (2005), in print.
14. P. Jenčuš, J. Polák, P. Lukáš and O. Muránsky, Periodic loading of dual phase steel studied by neutron diffraction, Proc. of CETS 2005, Budapest, in Materials Structure in Chemistry, Biology, Physics and Technology, Czech and Slovak Crystallographic Association, 2005, in print.
15. P. Lukáš, P. Jenčuš, O. Muránsky, J. Polák and J. Zrník, In-situ Neutron Diffraction Studies of Deformation and Transformation Characteristics of Metals, Proc. of 150th ISIJ Meeting 2005, September 29-30, Hiroshima, Japan, CAMP-ISIJ, Vol. 18 (2005), 1408-1411.

16. M. S. Koo, P. G. Xu, Y. Tomota, O. Muránsky, P. Lukáš and Y. Adachi, In situ neutron diffraction during thermo-mechanically controlled process in low alloy steels, Proc. of the 3rd Asian Conf. on Heat Treatment of Materials, Gyeongiu, Korea, November 2005, pp.15-17.

17. J. Zrník, Z. Nový, P. Lukáš, O. Muránsky, P. Jenčuš, J. Fiala, Development of thermomechanical processing in bulk Si-Mn TRIP Steel, in proc. of XIII. Verformungskundliches Kolloquim, March 2004, Leoben-Planneralm, Austria, p. 291.

REFERENCES

[1] W.D. Callister, Materials Science and Engineering, An Introduction, Sixth Editon, ISBN: 0471744778, Jun, 2005.

[2] P. G. Xu, Y. Tomota, O. Muránsky, P. Lukáš and Y. Adachi, In situ neutron diffraction during thermo-mechanically controlled processing of C-Mn(-Nb) steels, Proc. of 150th ISIJ Meeting 2005, September 29-30, Hiroshima, Japan, CAMP-ISIJ, Vol. 18 (2005) 1300-1303.

[3] P. Lukáš, D. Neov, P. Strunz, P. Mikula, M. Vrána, Y. Tomota, S. Harjo, P. Bittner, V. Novák, J. Phys. Cos. Jpn, vol. A 70 920010, pp. 548-550.

[4] P. Bittner, P. Lukáš, D. Neov, M.R. Daymond, V. Novák, G. Swallowe, Material Science and Engineering, A378/1-2 (2004), pp. 97-104.

[5] M.T. Hutchings and A.D. Krawitz (eds.), Measurement of Residual and Applied Stress Using Neutorn Diffraction, NATO ASI Series, Applied Sciences 26, Kluwer Acad. Publ. , 1992.

[6] P. Lukáš, Y. Tomota, S. Harjo, D. Neov, P. Strunz, P. Mikula, J. Neutr. Res., vol. 9 92001, pp. 415-421.

[7] S. Godet, Thermo-mechanical processing of TRIP-assisted multiphase steels, Doctoral Thesis, Université Catholique de Louvain, Louvain-la-Neuve, May 2003.

[8] E.O.Hall, Proc. Phys. Soc. 64B (1951) 747.

[9] N.J.Petch, J. Iron Steel Inst. 174 (1953) 25.

[10] F.B.Pickering: Physical Metallurgy and the Design of the Steels, London, Applied Science Publishers Ltd., pp.1978-275.

[11] V. Karel, Fyzika Kovov II, Editačné středisko VŠT, Košice, 1978.

[12] C.M. Parish, Fundamental study of phase transformations in Si-Al TRIP steels, Doctoral Thesis, University of Pittsburgh, Pittsburgh, Jun 2003.

[13] W.A. Smith, Structure and Properties of Engineering Alloys, 2nd ed., McGraw-Hill, 1993, P114-118.

[14] http://www.azom.com/details.asp?ArticleID=2537#_Carbon_steels

[15] A.J. DeArdo, C.I. Garcia and E.J. Palmiere, "Thermomechanical Processing of Steels," ASM Handbook, Vol 4: Heat Treating, ASM Intl., Materials Park, 1991, P237-255.

[16] E.J. Palmiere, C.I. Garcia, A.J. DeArdo, "The Influence of Niobium Supersaturation in Austenite on the Static Recrystallisation Behavior of Low Carbon Microalloyed Steels," Met. Trans. A, V27A, 1996, P951-960.

[17] O. Matsumura, Y. Sakuma and H. Takechi, Trans. ISIJ, 1987, 27, 570-579.

[18] H.K.D.H. Bhadeshia, Bainite in steels, 2nd edn, 2001, London, The Institute of Materials.

[19] Material World, 2002, 10, 22-23.

[20] Y. Tomota, K. Kuroki, T. Mori and I. Tamura, Material Science and Engineering, 1976, 24, 85-94.

[21] M.Y. Sherif, C.G. Mateo, T. Sourmail, H.K.D.H. Bhadeshia, Stability of retained austenite in TRIP-assisted steels, MST/5936, IoM Communications Ltd., published by Maney for the Institute of Materials, Minerals and Mining, 2003.

[22] http://www.krakatausteel.com/product/ifsteel/index.asp

[23] O.Z. Chen, B.J. Duggan, On cells and microbands formed in an interstitial-free steel during cold rolling at low to medium reductions, Metallurgical and materials transactions A, Volume 35A, November 2004, 3423.

[24] B. Engl, U. Heidmann, and W. Müschenborn, "Cold Formability and Light Weight Construction – Driving forces for recent steel development," in Modern LC and ULC Sheet Steels for Cold Forming: Processing and Properties, ed. W Bleck, Verlag Mainz, Aachen, 1998, P39-50.

[25] Section 4 – Glosarry, Advanced high strength steel application guidelines, www.wordaoutosteel.org, March, 2005.

[26] W.A. Smith, Structure and Properties of Engineering Alloys, 2nd ed., McGraw-Hill, 1993, P119-123.

[27] H.K.D.H. Bhadeshia, Lecture 11, Metallic Alloys, Materials Science & Metallurgy, 2nd year course, Metals and Alloys, 2005.

[28] Practical guidelines for the fabrication of duplex stainless steels, Reviesed Edition, International Molybdenum Association, Inc. of Pittsburgh, Pennsylvania, USA, 2001.

[29] T. Ros-Yanez, et al., Materials Characterization, vol. 47 (2001), pp. 93-104.

[30] E. Wirthl, et al., Int. Conf. on TRIP-aided high strength ferrous alloys, pp. 61.

[31] L. Zhao, et al., TRIP-aided ferrous alloys, Int. Conf. on TRIP-aided high strength ferrous alloys, pp. 141.

[32] H.K.D.H. Bhadeshia, ISIJ International, vol. 42 (2002), No. 9, pp. 1059-1060.

[33] M.Y. Sherif et al., Materials Science and Technology, vol. 20 (2004), pp. 319-322.

[34] Y. Tomota, et al., Material Science and Engineering, vol. 24 (1976), pp. 85-94.

[35] P. Jacques, et al., ISIJ int., vol. 41 (2001), pp. 1061-1067.

[36] http://epubl.luth.se/index-en.shtml

[37] http://ussautomotive.com/auto/tech/grades/TRIP600.htm

[38] V.F. Zackay, E.R. Parker, D. Fahr and R. Busch, "The Enhancement of Ductility in High-Strength Steel," Transactions of the ASM, V60, 1967, P252-259.

[39] P.J. Jacques, A. Petein, P. Harlet, Improvemen of mechanical properties hrough concurrent deformation and transformation: new steels for the 21st cenrury, Int. Cont. on TRIP-aided High Strength Ferrours Alloys, 2002

[40] AHSS Microstructure, Mechanical Behaviour, and Alloy Design, IISI-AutoCo, AHSS Gidelines, March 2004.

[41] ULSAB-AVC Technical Transfer Dispatch #6 (ULSAB-AVC, 2001).

[42] M.P. Puls and J.S. Kirkaldy, Metallurgical and materials transactions A, Volume 35A, 1972, 2777.

[43] O. Kawano, M. Takahashi, J. Wakita, K. Esaka and H. Abe, Proc. International Conf. on Physical Metallurgy of Thermomechanical Processing of Steel and Other Metals (Thermec – 88), Tokyo, Japan, 1988, 692.

[44] E. Bain and H.w. Paxton, "Alloying Elements", 2nd ed., ASM, Metals Park, Ohia, 1966, 104.

[45] G.R. Purdy, D.H. Neichert and J.S. Kirkaldy, Trnas. TMS/AIME, 1964, 1025.

[46] J.B. Gilmour, G.R. Purdy and J.S. Kirkaldy, Trans. TMS/AIME, 1972, 1455.

[47] J. Immamura and T. Furukawa, Nippon Steel Technical Report Overseas, 10, 1977, 103.

[48] T. Kato, K. Hashigushi, I. Takahashi, T. Irie, and N. Ohashi, „Fundamentals of Dual-Phase Steels", ed. R.A. Kot and B.L. Bramfitt, TMS/AIME, Warrendale, Pa., 1981, 199.

[49] S. Koyama, T. Ishii and K. Narita, J. Japna Inst. Metals 35, 1971, 161.

[50] S.K. Liu and G.Y. Zhang, Metallurgical and materials transactions A, 21A, 1990, 1509.

[51] H. Baumgrat, H.F. de Boer and F. Heisterkamp, „Proceedings of the International Symposium on Niobium", AIME, Warrendale, Pa, 1981, 883.

[52] L. Meyer, F. Heisterkemp and W. Mueschenborn, „Microalloying 75", Union Carbide Corporation, New York, 1975, 153.

[53] A.J. DeArdo, "Accelerated Cooling of Steel", The Metallurgical Society Inc., Warrendale, Pa, 1986, 97.

[54] C.A. Dube, Ph.D. Thesis, Carnegie Inst. Of Technology, 1948, as cited by A.K. Sinha in „Ferrous Physical Metallurgy", Butterworths, Boston, 1989.

[55] A.D. Chiro, Processing and properties of C-Si-Mn TRIP steels, Doctoral Thesis, McGill University, Montreal, Canada, August, 1997.

[56] J.W. Christian, "Theory of Transforamtions in Metals and Alloys", 2nd edn. Pt.1, Pergamon Press, Oxford, 1975.

[57] H.K.D.H. Bhadeshia, Bainite in Steels, The Institute of Materials, London, 1992, 124.

[58] H.K.D.H. Bhadeshia, Bainite in Steels, The Institute of Materials, London, 1992, 62.

[59] http://www.mete.metu.edu.tr/Facilities/Research/SMA/smatext/MART.htm

[60] H.K.D.H. Bhadeshia, Martensite in steels, https://www.msm.cam.ac.uk/phase-trans/2002/martensite.html

[61] C.L. Magee and H.W. Paxton, Trnas. Metall. Soc. AIME, 1968, 242, 1741 – 1749.

[62] D.C. Ludwigson and J.A. Berger, Journ. of The Iron and Steel Institute, 1969, 63.

[63] Y. Sakuma, D.K. Matlock and G. Krauss, J. Heat Treatment, 8, 109, 1990.

[64] J.M. Rigsbee, ICOMAT 1979, Martensitc Transformations, Cambridge, Mass., 1979, 381.

[65] A. Itami, M. Takahashi and K. Ushioda, 1994 High Strength Steels for Automotive Symposium Proceedings, 36th Mechanical Working and Steel Processing Conference, ISS/AIME, 1994, 245.

[66] Q.Y. Long, D. Tseng and K. Tangri, Metallography 20, 1987, 61.

[67] F.J. Humphreys nad M. Haterly, Recrystallisation nad related annealing phenomena, Oxford, Pergamon Press, 1996.

[68] R.F. Mehl, ASM Metals Handbook, 1948, ASM, Metals Park, Ohio, 259.

[69] J.E. Burke and D. Turnbull, Prog. Metal Physic, 3, 1952, 220.

[70] J.J. Jonas, C.M. Sellars and W.J. McG Tegart, Metallurgical Reviews, Review 130, 1969, 1-24.

[71] H.J. McQueen and N.D. Ryan, Material Science and Engineering, 2000, 290, 95-107.

[72] M.T. Hutchings, P.J. Withers, T.M. Holden, and T. Lorentzen, Introduction to the characterization of residual stress by neutron diffraction, ISBN: 0-415-31000-8, 2005.

[73] P.J. Withers, Residual stresses: measurement by diffraction, in Encyclopedia of Materials: Science & Technology, IV: Structural Phenomena, K.H.J. Buschow et al., Eds., Elsevier, Oxford, 2001, 8158-8170.

[74] P.J. Withers, Residual stress: definition, in Encyclopedia of Materials: Science nad Technology, IV: Structural Phenomena, K.H.J. Buschow et al., Eds., Elsevier, Oxford, 2001, 8110-8113.

[75] H.H. Lester and R.H. Aborn, Behaviour under stress of iron crystal in steel, Army Ordnance, 6, 120-127, 200-207, 283-287, 364-369, 1925.

[76] A.E. van Arkel, Über die verformung des kristallgitters von metallen durch mechanische bearbeitung, Physica B, 5, 208-212, 1925.

[77] European Synchronition Radiation Facility, Grenoble, France, Highlights 95-96, 2000.

[78] http://www.embl-heidelberg.de/ExternalInfo/public_relations/Synchrotron.html

[79] www.esrf.fr

[80] A.J. Allen, M. Bourke, W.I.F. David, S. Dawes, M.T. Hutchings, A.D> Krawitz and C.G. Windsor, Effect of elastic anisotropy on the lattice strain in polycrystalline metals and composites measured by neutron diffraction, in Proceedings of 2nd International Conference on Residual Stress, C. Beck, S. Denis, and A. Simon, Eds., Elsevier Applied Science, London, 1989, 78-83.

[81] M.T. Jensen, P. Brondsted, B.S. Johansen, T. Lorentzen, and O.B. Pedersen, Phase coupling and low cycle fatigue in a duplex stainless steel, in ICSMA-10, Fundamental Physical Aspects of the Strength of Crystalline Materials, H. Oikawa et al., Eds., Japan Institute of Metals, Sendai, 1994, 489-492.

[82] D.C. Dunand, D. Mari, M.A.M. Bourke, and J.A. Roberts, NiTi and NiTi-TiC composites, 4 and Neutron diffraction study of twinning and shape memory recovery, Met. Mater. Trans. A, 27, 1996, 2820-2836.

[83] W.D. Armstrong, T. Lorentzen, P. Brondsted, and P.H. Larsen, An experimental and modeling investigation of the external strain, internal stress and fiber phase transformation behaviour of a NiTi actuated aluminum metal matrix composite, Acta Metall., 46, 1998, 3455-3466.

[84] G.A. Webster, Ed., Polycrystalline Materials – Determination of residual stresses by neutron diffraction, ISO/TTA3 Technology Trends Assessment, Geneva, 2001.

[85] P.J. Withers, Depth capabilities of neutron and synchrotron diffraction strain measurement instruments, Part I – The maximum feasible path length, J.Appl. Crystallogr., 37, 596-606, 2004.

[86] P.J. Withers, Depth capabilities of neutron and synchrotron diffraction strain measurement instruments, Part II – Practical implicatins, J.Appl. Crystallogr., 37, 2004, 607-612.

[87] P.J. Webster, X.D. Wang, and G. Mills, Strain scanning using neutrons and synchrotron radiation, in Proceedings European Conference on Residual Stress IV, 4, 1966, 127-134.

[88] G.A. Webster, Neutron diffraction measurements of residual stress in ring and plug, Versailles Project on Advanced Materials and Structures (VAMAS) TWA20, Tech Report No. 38, 2000.

[89] M.R. Daymond, M.A.M. Bourke, R.B. Von Dreele, B. Clausen, and T. Lorentzen, Use of Rietveld refinement for elastic macrostrain determination and for the evaluation of plastic strain history from different spectra, J. Appl. Phys., 82, 1997, 1554-1562.

[90] T.M. Holden, A.P. Clarke, and R.A. Holt, Neutorn diffraction measurements of intergranular strain in Monel 400, Metall. Mater. Trans, 28A, 1997, 2565-2576.

[91] B.Clausen, T. Lorenzen, M.A.M. bourke, and M.R. Daymond, Lattice strain evolution during tensile loading of stainless steel, Material Science and Engineering, A259, 1999, 17-24.

[92] P.G. Th. van der Varst, Effective elastic properties, Details of selected topics from the lecture series Thermomechanics of solid materials (6M030), November, 2000.

[93] M.E. Tuttle, Review of the concepts of stress, strain, and Hooke's Law, Dept. Mechanical Engineering, University of Washington, Seattle.

[94] Lecture 7 – Elasticity, Kittel Chapter 3.

[95] R.W. Herzberg, Deforamtion and fracture mechanics of engineering materials, Wiley, New York, 1976.

[96] G. Simmons and H. Wnag, Single crystal elastic constants and calculated aggregate properties, a Handbook, M.I.T. Press, Boston, 1971.

[97] E. Kröner, Berechnung der elastischen konstants des vielkristalls aus den konstanten des einkristalls, Z. Physik, 151, 1958, 404-418.

[98] E. Kröner, Zur plastichen verformung des vielkristalles, Acta Metall., 9, 1961, 155-161.

[99] P. G. Xu, Y. Tomota, O. Muránsky, P. Lukáš, and Y. Adachi, Austenite-to-Ferrite Transformation and Phase Strain Evolution in Low Alloy Steels during Thermo-mechanically Controlled Process Studied by In Situ Neutron Diffraction, Materials Sience and Enginnering A, accepted for publication (2006).

[100] G.E. Bacon, Neutorn Diffraction, Clarendon Press, Oxford 1975, chap. 2.6, p.55.

[101] S.C.Hong, S.H. Lim, H.S. Hong, K.J.Lee, D.H. Shin, K.S. Lee., Material Science and Engineering A, 335 (2003), pp. 241-248.

[102] D.N. Hanlon, J. Sietsma, S. van der Zwaag, ISIJ INt. 41 (2001), pp. 1028-10396.

[103] X.J. Sun, H. Dong. Q.Y. Liu, Y.Qo. Weng, Iron and Steel 40 (2005), Suppl. 264-269.

[104] J. Sietsma, S. van der Zwaag, Acta Materialia 52 (2004) pp. 4143-4152.

[105] P.G. Xu, Y. Tomota, O. Muránsky, P. Lukáš, Y. Adachi, Iron and Steel 40 920050, Suppl. 234-238.

[106] J. Zrník, Z. Nový, P. Lukáš, O. Muránsky, P. Jenčuš, J. Fiala, Development of thermomechanical processing in bulk Si-Mn TRIP Steel, Leoben-Planneralm, Austria, p. 291

[107] W.Soboyejo, Mechanical Properties of Engineered Materials, Princeton University, Princeton, New Jersey, ISBN: 0-8247-8900-8.

[108] P.Lukáš, P.Jenčuš, J.Zrník, Z.Nový, Optimization of thermal processing of Si-Mn TRIP steel by using in situ neutron diffraction, ICM9, Geneva, 2003

[109] Y. Tomota et al., Acta Materialia, vol. 52 (2004), pp. 5737-5745.

[110] O. Muránsky, J. Zrník, P. Lukáš, P. Jenčuš, Z. Nový, Acta Metalurgica Slovaca, 10 (2004) 228.

[111] O. Muránsky, P. Lukáš, P. Šittner, J. Zrník, P. Jenčuš and Z. Nový, In situ neutron diffraction studies of phase transformations in Si-Mn TRIP steel, Materials Science Forum, vol. 490-491 (2005) pp: 275-280.

[112] K. P. Kwang et al., Material Science Forum, Vols. 408-412 (2002) pp. 571-576.

[113] Q. Furnémont et al., Fundamental Materials Science of the TRIP Phenomenon, Int. Conf. On TRIP-Aided High Strength Ferrous Alloys, Ghent, Belgium, 2002, p. 39.

[114] J. Zrník, Z. Nový, P. Lukáš, O. Muránsky, P. Jenčuš, J. Fiala, in proc. of XIII. Verformungskundliches Kolloquim, March 2004, Austria, p. 291.

[115] E.C. Oliver, M.R. Daymond, P.J. Withers, T. Mori, Materials Science Forum, vol. 404-407 (2002), pp. 489-494.

[116] M.R. Daymond and H.G. Priesmeyer, Acta Materialia, vol. 50 (2002), pp. 1613-1626.

[117] E.C. Oliver, M.R. Daymond, P.J. Withers, Acta Materialia, vol. 52 (2004), pp. 1937-1951.

[118] Q. Furnémont et al., International Conference on TRIP-aided high strength ferrous alloys, ISBN 90-76019-17-7, 2002, pp. 39-44.

[119] J. Hutchinson, Proc. Roy. Soc., vol. A319 (1970) pp. 247-72.

[120] V. Novák and P. Šittner, Material Science and Engineering, A 378/1-2, 2004, pp. 490-498.

[121] P.A. Turner, C.N. Tomé, Acta Metallurgica, vol. 42 (1994), 4043.

[122] E.C. Oliver, M.R. Daymond, P.J. Withers, T. Mori, Mater. Sci. Forum, vols. 404-7, pp. 489-494.

[123] P.Lukáš, S. Harjo, K. Macek, M. Ono, Y. Tomota, P. Strunz, J. Zrník, M. Vrána, Microstrain characterizatin of metals using high-resolution neutron diffraction, Materials Structure, vol. 4, no.3, (1997).

[124] Th. H. De Keijser, J.I. Langford, E.J. Mittemeijer, A.B. P. Vogels, Use of the Voigt Function in a single-line method for the analysis of X-ray diffraction line broadening, J. Appl. Cryst. (1982), (15), pp. 308-314

[125] G.K. Williamson, R.E. Smallman, Phil. Mag., 1955, 1, pp.34.

[126] P. Jenčuš, In-situ neutron diffraction studies of fatigue mechanisms in steels, Doctoral Thesis, Czech Technical University in Prague, 2006.

[127] S. Harjo, Y. Tomota, P. Lukáš, D. Neov, M. Vrána, P. Mikula, M. Ono, In-situ neutron diffraction study of α-γ Fe-Cr-Ni alloys under tensile deformation, Acta Mater. 49 (2001), pp. 2471-2479.

[128] S. Harjo, Y. Tomota, M. Ono, Acta Mater., 47, (1999), pp. 353.

[129] S. Harjo, Y. Tomota, P. Lukáš, M. Vrána, D. Neov, P. Mikula, Mater. Sci. Forum, 328, (2000), pp. 347-349.